UC Irvine

UC Irvine Electronic Theses and Dissertations

Title

Single-Molecule Measurements of Proteins using Carbon Nanotube Field-Effect Transistors

Permalink

https://escholarship.org/uc/item/3m7532zj

Author

Sims, Patrick

Publication Date

2015

Copyright Information

This work is made available under the terms of a Creative Commons Attribution-NoDerivatives License, availalbe at https://creativecommons.org/licenses/by-nd/4.0/

Peer reviewed|Thesis/dissertation

eScholarship.org Powered by the California Digital Library
University of California

UNIVERSITY OF CALIFORNIA,
IRVINE

Single-Molecule Measurements of Proteins using Carbon Nanotube Field-Effect Transistors

DISSERTATION

submitted in partial satisfaction of the requirements
for the degree of

DOCTOR OF PHILOSOPHY

in Physics

by

Patrick Craig Sims

Dissertation Committee:
Professor Philip G. Collins, Chair
Professor Gregory A. Weiss
Professor Zuzanna S. Siwy

2015

Portions of Chapter 2, 4, & 5 © 2013-2014 American Chemical Society
Portions of Chapter 2 © 2012 American Association for the Advancement of Science
All other materials © 2015 Patrick Craig Sims

DEDICATION

To Lili

TABLE OF CONTENTS

Page

LIST OF FIGURES v

LIST OF TABLES vii

ACKNOWLEDGMENTS viii

CURRICULUM VITAE ix

ABSTRACT OF THE DISSERTATION xii

1 Introduction 1
- 1.1 Conformational Variability 2
  - 1.1.1 Static Disorder 2
  - 1.1.2 Dynamic Disorder 2
  - 1.1.3 Conformational Motion and Catalysis 4
- 1.2 Single Molecule Techniques 5
  - 1.2.1 Single Molecule Fluorescence 5
  - 1.2.2 Förster Resonance Energy Transfer (FRET) 6
  - 1.2.3 Electronic Measurements of Single Molecules 6
- 1.3 Single-Walled Carbon Nanotube FET Sensors 7
  - 1.3.1 Electronic Measurements of T4 Lysozyme 8

2 Experimental Design and Fabrication 9
- 2.1 Fabrication of Carbon Nanotube Field-Effect Transistors 9
- 2.2 Synthesis of cAMP-Dependent Protein Kinase (PKA) 10
  - 2.2.1 PKA Mutagenesis 10
  - 2.2.2 PKA Expression and Purification 10
  - 2.2.3 PKA Activity Assay 13
- 2.3 Protein Conjugation 14
  - 2.3.1 Confirming Protein Conjugation 15
- 2.4 T4 Lysozyme Variants 17
- 2.5 Electrical Measurements 18
- 2.6 Three-Level Switching Data Analysis 18

3 Protein Conjugation to SWCNTs 24
- 3.1 The Standard Conjugation Protocol 24
- 3.2 Effects of High Protein Concentration on Conjugation 26
- 3.3 Effects of Contamination and Defects on the Conjugation Process 29
- 3.4 Effects of Tween-20 on the Conjugation Process 34
- 3.5 Effects of Long Duration and Low Protein Concentration 41

3.6 Effects of Solution-dependent Variation on Conjugation....44
3.7 Summary....46

4 Single-Molecule Signal Transduction in SWCNT FETs....48
4.1 Debye Screening in Single-Molecule SWNT FETs....48
4.2 Electrostatic Effects of Specific Amino Acids....55
4.3 Electrostatic Mechanism....63
4.4 Summary....67

5 Single-Molecule Measurements of cAMP-Dependent Protein Kinase (PKA)....70
5.1 cAMP-dependent Protein Kinase (PKA)....71
5.2 Control Measurements....74
5.3 Electronic Measurements of PKA Binary Complexes....75
5.4 Dynamic Disorder of PKA Binary Complex....80
5.5 Electronic Measurements of PKA Ternary Complex....86
5.6 Transition Probabilities of PKA....88
5.7 The Efficiency of Phosphorylation by PKA....90
5.8 Fluctuation and Noise Measurements....93
5.9 Electrically-Driven Deposition of Peptides....95
5.10 Summary....101

BIBLIOGRAPHY....103

LIST OF FIGURES

Page

Figure 2.1 Expression and Purification of T32C PKA Variant....12

Figure 2.2 PKA Activity Assay 13

Figure 2.3 Examples of T4 Lysozyme Devices 16

Figure 2.4 Duration Versus Event Number for Three-Level System....19

Figure 2.5 Matrices for Extracting General Transitional Behavior....20

Figure 2.6 Statistical Parameters for Three States 21

Figure 2.7 Statistical Parameters for Succeeding State....21

Figure 2.8 Statistical Parameters for Preceding State 21

Figure 2.9 Histograms to Determine Steps and Duration between certain Transitions 22

Figure 2.10 Binned-Average of State Duration versus Time....23

Figure 3.1 Effect of Time and Concentration on Standard Conjugation Process 28

Figure 3.2 Effect of Thermal Treatment in Air on Conjugation of Lysozyme 30

Figure 3.3 Effect of using as-grown Carbon Nanotubes on Lysozyme Conjugation....32

Figure 3.4 Effect of using as-grown Carbon Nanotubes on PKA Conjugation 33

Figure 3.5 Effect of UV/Ozone on Conjugation 34

Figure 3.6 Effect of Thermal Treatment in Air without a Tween-20 Rinse....36

Figure 3.7 Scaling of Non-specific Adsorption with Time and Concentration 37

Figure 3.8 Mitigating Non-specific Adsorption of PKA using Tween-20 39

Figure 3.9 Effect of Tween-20 in the Lysozyme Conjugation Step....40

Figure 3.10 Time-Dependent Adsorption of Lysozyme at Low Concentrations....42

Figure 3.11 Conjugation of DNA Polymerase at Low Concentrations....43
Figure 3.12 Variability of Long Duration Conjugation of Lysozyme....45
Figure 3.13 Time-Dependent Variability of Protein Solutions....46
Figure 4.1 Debye Screening of Signal Transduction....49
Figure 4.2 Measurements of S36C T4 Lysozyme Variant....52
Figure 4.3 Detailed View of the Lysozyme-SWNT Interface....54
Figure 4.4 Dynamic I_{sd}(t) Signals for R119A and K83A/R119E Variants....56
Figure 4.5 Compilation of Switching Amplitudes for T4 Lysozyme Variants....61
Figure 4.6 Average Transduction by T4 Lysozyme Variants....62
Figure 5.1 PKA-Labeled, SWNT-based Nanocircuit....73
Figure 5.2 Control Measurements of a Pyrene-Maleimide Coated SWNT Device....75
Figure 5.3 Representative ΔI_{sd} (t) Signals for a PKA-Conjugated SWNT Device....77
Figure 5.4 Dynamic Disorder of PKA with ATP or Kemptide....81
Figure 5.5 Scatter Plot of $<t_{bound}>$ and $<t_{waiting}>$ for ATP or Kemptide....83
Figure 5.6 Conductance Fluctuations due to Kemptide Binding and Release....85
Figure 5.7 Distributions of the Duration spent in three PKA Conformations....88
Figure 5.8 Probability of PKA Re-opening....91
Figure 5.9 A Kinetic Scheme for the Phosphorylation of Kemptide....92
Figure 5.10 Time-Dependence of the Effective Gating of a single PKA Device....95
Figure 5.11 Electrically-Driven Deposition of PKI....98
Figure 5.12 Control Measurements for Electrically-Driven Deposition....99

LIST OF TABLES

Page

Table 4.1 Electric Field Magnitudes Generated by Point Charges of Interest.....65

Table 5.1 PKA Binding Rates.....78

Table 5.2 Matrix of Transition Probabilities and Mean Durations.....89

ACKNOWLEDGMENTS

As this part of my journey reaches its ultimate conclusion, I would like to pause and offer a sincere thanks to all those who have supported, encouraged, and guided me. None of this would have been possible without the unyielding support from so many.

Professor Collins is an invaluable mentor, guide, and advisor. His continual and constant guidance served as a north star during this voyage whether I was idling in the doldrums, cruising with the trade winds, or bracing against rough seas. I will always be grateful for everything he has done for me.

Professor Weiss is the second half of the dynamic advisory duo. His friendly demeanor coupled with his ravenous appetite for those under his wing to improve will leave a lasting impression. He helped me become a better scientist, and his insights gave me a new perspective.

The now Professor Yongki Choi imparted me with the technical and scientific knowledge required to make this possible. He was an invaluable asset to me and cannot thank him enough.

Max Akhterov and Elliot Fuller are true friends and compatriots. I want to thank them for always being there to offer their valued opinions or to engage with me in the occasional boisterous banter.

Without Mariam Iftikhar I would have been lost. She persistently went above and beyond to help me in every way. I truly am grateful for the opportunity I had to work with her.

I would also like to thank all the Collins and Weiss Lab members I was lucky enough to interact with: Brad Corso, Danny Wan, Steve Denning, Steve Hunt, Tatyana Sheps, Deng Pan, Israel Perez, Tolga Gul, Arith Rajapakse, Tetyana Ignatova, Jill Pestana, Tivoli Olsen, Issa Moody, and Kaitlin Pugliese.

I would like to especially thank my family for giving me unconditional love and always being a pedestal to lean on. Thank you, Mom, Dad, Weston, Nicole, Devin, Michelle, Troy, Jill, and Luke.

I would also like to acknowledge my family away from home: Sohaila, Khosrow, and Nick. Your love and care eased my burden tremendously.

Finally, Lili. Her patience knows no bounds. Without her, I would have floundered. Her love was a beacon of light guiding me through the dark nights and was a warm blanket to weather wintry gusts. I want to thank her for holding my hand and walking beside me on this long and twisting path.

CURRICULUM VITAE

Patrick Craig Sims

2009	B.S. in Physics with minor in Mathematical Sciences, University of Nevada, Las Vegas
2009-12	Teaching Assistant, Department of Physics and Astronomy, University of California, Irvine
2011-12	NSF-IGERT Fellow, LifeChips, University of California, Irvine
2014	M.S. in Physics with emphasis in Chemical and Material Physics, University of California, Irvine
2014	Multidisciplinary Design Program Fellow, University of California, Irvine
2012-15	NSF-GAAN Fellow, Department of Physics and Astronomy, University of California, Irvine
2010-15	Research Assistant, Department of Physics and Astronomy, University of California, Irvine
2015	Ph.D. in Physics with emphasis in Chemical and Material Physics, University of California, Irvine

FIELD OF STUDY

Single-Molecule Biophysics, Carbon Nanotube Electronics

PUBLICATIONS

1. K.M. Pugliese, O.T Gül, Y. Choi, T.J. Olsen, P.C. Sims, P.G. Collins, & G.A. Weiss. "Processive Incorporation of Deoxynucleoside Triphosphate Analogs by Single-Molecule DNA Polymerase I (Klenow Fragment) Nanocircuits." *Journal of the American Chemical Society* 137 (30), 9587-9594 (2015).

2. M.V. Akhterov, Y. Choi, T.J. Olsen, P.C. Sims, M. Iftikhar, O.T. Gül, B.L. Corso, G.A. Weiss, & P.G. Collins. "Observing Lysozyme Closing and Opening Motions by High-Resolution Single Molecule Enzymology." *ACS Chemical Biology* 10 (6), 1495-1501 (2015).

3. B.L. Corso, I. Perez, T. Sheps**,** P.C. Sims, O.T. Gül, & P.G. Collins. "Electrochemical Charge-Transfer Resistance in Carbon Nanotube Composites." *Nano Letters* 14 (3), 1329-1336 (2014).

4. *Y. Choi, P.C. Sims, T.J. Olsen, M. Iftikhar, B.L. Corso, O.T. Gül, G.A. Weiss, & P.G. Collins "Single Molecule Sensing with Carbon Nanotube Devices." *Proc. SPIE*. 8814, 8814Q, (2013).

5. *Y. Choi, P.C. Sims, T.J. Olsen, O.T. Gül, B.L. Corso, M. Iftikhar, G.A. Weiss, & P.G. Collins "Single Molecule Enzymology Using Carbon Nanotube Circuits." *IEEE Transducers.* 17, 633-636 (2013).

6. P.C. Sims, I.S. Moody, Y. Choi, C. Dong, M. Iftikhar, B.L. Corso, O.T. Gül, G.A. Weiss, & P.G. Collins. "Electronic Measurements of Single-Molecule Catalysis by cAMP-Dependent Protein Kinase A." *Journal of the American Chemical Society* 135 (21), 7861-7868 (2013).

7. Y. Choi, T.J. Olsen, O.T. Gül, P.C. Sims, B.L. Corso, C. Dong, W.A. Brown, P.G. Collins, & G.A. Weiss. "Electronic Measurements of Single-Molecule Processing by DNA Polymerase I (Klenow fragment)." *Journal of the American Chemical Society* 135 (21), 7855-7860 (2013).

8. *I.S. Moody, Y. Choi, T.J. Olsen, P.C. Sims, P.G. Collins, & G.A. Weiss. "Dissecting Lysozyme by Single-Molecule Techniques." *Lysozymes, Sources, Functions, and Role in Disease* Nova Publishers, 193-214, (2013).

9. Y. Choi, T.J. Olsen, P.C. Sims, I.S. Moody, B.L. Corso, M.N. Dang, G.A. Weiss, & P.G. Collins "Dissecting Single-Molecule Signal Transduction in Carbon Nanotube Circuits with Protein Engineering." *Nano Letters* 13 (2), 625-631 (2013).

10. Y. Choi, I.S. Moody, P.C. Sims, S.R. Hunt, B.L. Corso, D.E. Seitz, L.C. Blaszczak, P.G. Collins, & G.A. Weiss. "Single-molecule Dynamics of Lysozyme Processing Distinguishes Linear and Cross-linked Peptidoglycan Substrates." *Journal of the American Chemical Society* 134 (4), 2032–2035 (2012).

11. Y. Choi, I.S. Moody**,** P.C. Sims, S.R. Hunt, B.L. Corso, I. Perez, G.A. Weiss, & P.G. Collins. "Single-molecule Lysozyme Dynamics Monitored by an Electronic Circuit." *Science* 335, 319–324 (2012).

*Non Peer-reviewed.

ORAL PRESENTATIONS

1. P.C. Sims & P.G. Collins "Monitoring Single Biomolecule Dynamics Using a Carbon Nanotube FET" Presented at the CMOS Emerging Technologies Research Symposium, Grenoble, France (2014).

2. P. C. Sims, et al. "Single Molecule Kinetics of cAMP-Dependent Protein Kinase Monitored Continuously by a Carbon Nanotube Transistor." Presented at the American Physical Society March Meeting, Baltimore, MD. (2013).

3. P.C. Sims, et al. "Single Molecule Kinetics of cAMP-Dependent Protein Kinase Monitored Continuously by a Carbon Nanotube Transistor." Presented at the Biophysical Society Annual Meeting, Philadelphia, PA. (2013).

4. P.C. Sims, et al. "The Transduction Mechanism of Carbon Nanotube Transistors Monitoring Single Molecule Protein Dynamics." Presented at the American Physical Society March Meeting, Boston, MA. (2012).

5. P. C. Sims, et al. "Single Molecule Lysozyme Dynamics Monitored by an Electronic Circuit" Presented at the American Association for the Advancement of Science: Pacific Division, San Diego, CA (2011).

SELECTED HONORS AND AWARDS

• NSF-GAANN Fellowship Recipient (2012 – 2015);

• UC Irvine Multidisciplinary Design Program Fellow (2014);

• NSF-IGERT Video and Poster Competition Judges' Choice Award (2013);

• NSF-IGERT LifeChips Fellowship Recipient (2011 – 2012);

• UC Irvine Regents' Fellowship Recipient (2009);

• Nevada NASA Space Grant Consortium Undergraduate Scholarship (2006 – 2008); and

• UNLV Provost's Scholarship (2005).

PROFESSIONAL WORKSHOPS

• NSF-IGERT LifeChips Bootcamp at the University of California, Irvine (2011)

• BioNanotechnology Summer Institute at the University of Illinois, Urbana-Champaign (2011)

• X-Ray Crystallography Workshop at Los Alamos, NM (2007)

ABSTRACT OF THE DISSERTATION

Single-Molecule Measurements of Proteins using Carbon Nanotube Field-Effect Transistors

By

Patrick Craig Sims

Doctor of Philosophy in Physics

University of California, Irvine, 2015

Professor Philip G. Collins, Chair

Single-walled carbon nanotube (SWCNT) field-effect transistors (FETs) provide a promising platform for investigating proteins at the single-molecule level. Recently, we have demonstrated that SWCNT FETs have sufficient sensitivity and bandwidth to monitor the conformational motions and processivity of an individual T4 lysozyme molecule. This is accomplished by functionalizing a SWCNT FET device with a single protein and measuring the conductance versus time through the device as it is submerged in an electrolyte solution. To generalize this approach for the study of a wide variety of proteins at the single-molecule level, this dissertation investigates the conjugation process to determine and isolate the key parameters involved in functionalizing a SWCNT with a single protein, the physical basis for transducing conformational motion of a protein into an electrical signal, and finally, the general application of the technique to monitor the binary and ternary complex formation of cAMP-dependent protein kinase (PKA).

A systematic investigation of the conjugation process examined the effects of numerous parameters on the device yield. These parameters included the protein concentration, incubation

duration, presence or absence of surfactant, resist contamination, defects, thermal treatments, and protein time-dependent variability. The results suggested that the dominant factors driving the yield may be the solubility of pyrene maleimide in ethanol or the efficiency of maleimide-thiol reaction.

The next study focused on understanding the transduction mechanism underlying the device's sensitivity to enzymatic conformational motion. It was first established that the transduction was due to an electrostatic interaction near the sidewall of the SWCNT. This was accomplished by measuring the signal amplitude of devices in solutions with varying Debye screening lengths. Knowing that the effect was electrostatic in nature, lysozyme variants were measured that were comprised of differing charged residues near the attachment site to the deivce. This confirmed that the transduction mechanism was the local gating of the device due to the motion of charged amino acids near the SWCNT.

Finally to show the generality of the technique, measurements were conducted with a PKA molecule tethered to the SWCNT device. The apo, binary, and ternary complex conformational states were clearly resolved. Observations of the formation of the binary complex of PKA in the presence of ATP or its peptide substrate revealed the single-molecule kinetic rates of binding and unbinding. Monitoring PKA in the presence of both ATP and the peptide substrate showed cooperative binding and the full catalytic cycle of the enzyme as it phosphorylated the peptide substrate. From this data, the complete transition probability matrix as well as the conversion rates between the conformations was determined. Finally, the vicissitudes of PKA between the intermediate and the closed conformations as it attempts to phosphorylate its peptide substrate

suggest that PKA is a highly dynamic enzyme that has evolved to efficiently act as a molecular switch as opposed to optimizing its catalytic efficiency.

Chapter 1

Introduction

Observing and deciphering the intricate interactions and motions of proteins that are inherent in all life's processes is a keystone in building an archway to understanding the physical underpinnings of life at the molecular level. Life itself is a testament that proteins effectively perform necessary functions, but what is not well understood are the physical and chemical mechanisms that occur at the molecular level that drive their function. The ability to resolve in real-time the dynamical and kinetic behavior of proteins at relevant timescales provides an opportunity to understand the intricate and complex behavior of proteins as they perform their processes, and when done at the single molecule level provides rich insight into hidden steps and time-varying behaviors that are otherwise obscured at the ensemble level. Being able to monitor the behavior of the molecule as opposed to an average behavior gives further understanding of protein variability (static disorder), time-dependent variability (dynamic disorder), and innate mechanistic behavior of a protein during individual binding, unbinding, or catalytic events.

1.1 Conformational Variability

1.1.1 Static Disorder

Static disorder describes the conformational heterogeneity within an ensemble of proteins. In essence static disorder arises from a protein in a conformational state with a large energy barrier where the interconversion between conformational states is slow with respect to the reaction rate.[1,2] At the ensemble level this leads to nonexponential kinetics due to the diversity of the reaction rates.[1-3] Ignoring the effects of dynamic disorder which will be described later, at the single molecule level this static disorder leads to reaction rates that vary between molecules but not within the same molecule. The effect of static disorder therefore should be discernible by comparing how the reaction rates vary between molecules. Furthermore at long enough timescales, single molecule measurements could be able to discern the slow interconversion rate between these large energy barrier conformational states. The ability to measure the reaction rates of single proteins allows for the characterization of the heterogeneity between proteins to understand folding pathways that lead to different conformational states or to ascertain the effects of co- or post-translational modifications on protein activity.

1.1.2 Dynamic Disorder

If the energy barrier between conformational states is small enough such that the interconversion rate between states is faster than the reaction rates, then dynamic disorder occurs.[1] Absent

static disorder, dynamic disorder leads to exponential rate kinetics at the ensemble level since its effect can be replaced with a time average.[1] At the single molecule level, dynamic disorder leads to stretched exponential distributions of waiting times due to the fluctuations in the rate constants within an individual protein. This heterogeneity of rate constants within a single molecule provides information on the accessible conformations. Furthermore, statistical calculations of the waiting times such as the randomness parameter can provide semi-quantitative insight in the effect of dynamic disorder. For reactions comprised of rate-limiting poisson processes, $r = 1/N$ [4,5], but in the presence of increasing dynamic disorder r can become much greater than unity.[6] This muddles the capability of determining the exact number of rate-limiting steps in a process in systems with dynamic disorder. The presence of high levels of dynamic disorder—high enough to mask the rate-limiting processes—is not a general phenomenon in many biological systems.[6-10] Minimal dynamic disorder is apparent in some biological processes due to the ability to extract the number of rate-limiting processes. This may be because some biological processes require precise control in order to repeatedly and effectively perform a function on a specific substrate. For example, single molecule measurements of T4 lysozyme revealed the presence of multiple rate-limiting steps in presence of its substrate peptidoglycan.[11] Other enzymes such as PKA may need to undergo rapid conformational changes, leading to higher dynamic disorder, to effectively bind and phosphorylate a diverse number of target substrates.[12] Single molecule studies over a range of biological systems offer the opportunity to examine the number of rate-limiting steps in a process in the absence of dynamic disorder and to begin to understand why some biological systems have evolved to have dynamic disorder while others have not.

1.1.3 Conformational Motion and Catalysis

The effect of conformational motion of enzymes on catalysis remains a controversial topic in enzymology.[13] There are two predominant lines of thought. The first is that non-equilibrium effects due to conformational motion increase the transmission coefficient, i.e., provide directionality along the reaction coordinate to minimize any barrier recrossings from product to reactants.[14] The other suggests that non-equilibrium dynamics due to conformational motions have minimal effect on the enhancement in the reaction rate caused by enzymes, but the enhancement is instead due to the enzyme providing an electrostatically preorganized environment that lowers the barrier to the transition state.[13,15] Other lines of thought on enzyme catalysis are steric strain, near-attack conformations, entropic effects, desolvation, and low-barrier hydrogen bonds.[13] Catalysis may indeed be driven by one or more of these effects. These views on catalysis describe the transition from the substrate-bound state, ES, through the transition state to the product bound state, EP. Single molecule studies with sufficient spatial and temporal resolution may at some point finally settle this question.

Also controversial in the field of enzymology is the recognition step for ligand binding leading from the unbound state of the enzyme, E + S, to the substrate-bound state, ES.[16] The two predominant mechanisms in which enzymes recognize their cognate ligands are by conformational selection[17,18] or by induced fit[19]. The conformational selection model describes a highly flexible enzyme that continual samples its conformational space for a suitable conformation for binding the ligand, i.e., large-scale conformational changes occur before ligand

binding. The induced fit model differs in that the large-scale conformational changes proceed after ligand binding. Enzymes may use these mechanisms or a combination of these mechanisms to bind their cognate ligands.[20-22] Single molecule offers the ability to view conformational changes at the single molecule level providing an opportunity to determine the specific mechanism enzymes or classes of enzymes bind to specific targets.

1.2 Single Molecule Techniques

Optical and electronic approaches have been developed to observe these phenomena. In general, the optical approaches rely on fluorescence to observe phenomena related to enzymatic conformational motion, binding, and turnover events, while the electronic approaches depend on measuring a change in electrical conductance.

1.2.1 Single Molecule Fluorescence

In order to elucidate binding or turnover events, it is necessary to label the substrate with a quenched fluorophore that fluoresces upon binding or turnover.[23,24] This labeling may also have unintended consequences as the measured binding and catalytic rates of the labeled-substrate may differ from that of the native substrate. While this approach can be used to observe single molecule kinetics, a different fluorescence approach must be used to reveal conformational dynamics.

1.2.2 Förster Resonance Energy Transfer (FRET)

Förster Resonance Energy Transfer (FRET) enables temporal monitoring of spatial changes related to binding or conformational dynamics.[25] To accomplish this, two fluorophores which act as a donor-acceptor pair are labeled in close proximity to each other or are labeled in such a way that at some point will be in close-proximity as would be the case for substrate binding.[25-27] As the donor and acceptor fluorophores move closer or farther apart, the energy transfer between them scales with the distance between the fluorophores.[25-27] This enables the measurement of the respective motion between the two sites and thereby allowing the observation of the conformational dynamics of the biomolecule. While single molecule fluorescence techniques provide valuable insight into the behavior of single molecules, they suffer from the inability to monitor single molecules with high temporal resolution for long durations due to the tradeoff between photon flux and photobleaching.[28]

1.2.3 Electronic Measurements of Single Molecules

The advent of one-dimensional electronic systems based on carbon nanotubes[29,30] and silicon nanowires[31] laid the foundation for the development of nanoelectronic (bio)chemical sensors that overcome the intrinsic limitations of fluorescence-based measurements. By harnessing the low-dimensional electronic properties of these systems, the initial sensors based on these materials achieved label-free detection of specific analytes with high sensitivity.[32-34] Building on these initial efforts, researchers have pursued the development of sensors using new materials such as graphene[35,36] and have focused their attention on understanding the physics

underlying the sensitivity.[37-40] Recently, electronic techniques based on single-walled carbon nanotube (SWCNT) field-effect transistors (FETs) [11,41,42] and nanopores [43] have been developed with single-molecule sensitivity that are label-free and allow for measurements with microsecond resolution for durations that can span hours, thus enabling the continuous monitoring of a single molecule over a range of timescales inaccessible to fluorescence techniques. Of particular interest are single molecule sensors based on SWCNT FETs as their sensitivity, bandwidth, and device architecture provides an opportunity to generalize the technique to a range of chemical and biological systems.

1.3 Single-Walled Carbon Nanotube FET Sensors

The sensing mechanism behind single-walled carbon nanotube (SWCNT) arises through a Schottky barrier effect, i.e., modulation of the work function at the metal contacting the SWCNT, or an electrostatic gating effect.[37] When the contact is passivated to prevent any adsorption onto it, the dominant mechanism is the electrostatic gating effect which is due to a change in the electrostatic environment surrounding the SWCNT upon adsorption or binding. This effect has been used to achieve single molecule sensitivity by introducing a defect into SWCNT which localizes the gate dependence of the device.[44] Using this approach, researchers have observed individual molecular reactions[41] and DNA binding events[42,45].

While the introduction and modification of defects in SWCNTs allows for high sensitivity, it suffers from irreproducibility as the introduction of a defect can lead to the SWCNT becoming irreversibly insulating. Also this approach is serial as each device needs to be monitored such

that the oxidative damage to the SWCNT is minimized. To usurp this, we developed a technique that relies on non-covalent modifications of the SWCNT to attain single molecule sensitivity as presented in previous reports.[11,46]

1.3.1 Electronic Measurements of T4 Lysozyme

This approach relies on using pyrene maleimide to non-covalently adsorb onto the SWCNT, and then covalently tether a protein through a maleimide-thiol reaction. It was first used to monitor the single molecule behavior of T4 Lysozyme as it interacted with a cell wall component of bacteria called peptidoglycan.[11] From these measurements, the SWCNT sensor could easily distinguish between the open and closed conformation of T4 Lysozyme's hinge. Furthermore, we extracted rate constants pertaining to the productive and unproductive hinge motion of the enzyme and showed that the duration the enzyme spends doing this unproductive motion is directly related to the amount of crosslinking in the peptidoglycan substrate.[46] Because we were able to monitor T4 Lysozyme for long durations and with high resolution, we established the T4 Lysozyme as a processive enzyme, quantified the effects of pH on its various rate constants, and determined the number of rate-limiting steps traverse in the enzymes open and closed conformations.[11]

While the previous reports demonstrated the rich capability of this technique in observing conformational motions of enzymes, this dissertation will demonstrate how this technique can be generalized and applied to other enzymes.

Chapter 2

Experimental Design and Fabrication

2.1 Fabrication of Carbon Nanotube Field-Effect Transistors

The methodology for fabricating SWCNT FETs has been expounded in previous reports. In short, SWCNT are formed on 4 inch degenerately doped (p++) silicon wafers with a 250 nm thermally formed insulating oxide layer from Keggin $Fe_{30}Mo_{84}$ catalyst nanoparticles [47,48] using chemical vapor deposition [49]. After the growth step, the wafers are transferred to a clean room where source and drain electrodes are lithographically defined using photolithography and formed using electron-beam evaporation. The wafers also have a titanium backing which serves as the gate electrode for the SWCNT devices. After fabrication, the devices are first characterized electronically to determine their resistance, transconductance, and type. Devices that appear suitable for electronic measurements are then characterized using atomic force microscopy to ensure that the device is comprised of an individual single-walled carbon nanotube free from any interfering particulates on its surface. Following this characterization,

the SWCNT-metal contacts and the majority of the oxide layer are passivated using an electron-beam resist (A3 PMMA, MicroChem) to limit Schottky barrier effects as well as to minimize leakage current.

2.2 Synthesis of cAMP-dependent Protein Kinase (PKA)

2.2.1. PKA Mutagenesis

A mutation introduced into the gene encoding protein kinase A (PKA) placed a free thiol on the protein surface for bioconjugation to the SWCNT. This mutation, T32C, was synthesized using the DNA sequence for the core catalytic domain of wild-type PKA as a template for splice overlap extension PCR using the primers PKA-T32C-F (5'-GAAAAAATGGGAGCTTCTCAGAATAC-3') and PKA-T32C-R (5'-GTATTCTGAGAAGCTCCCATTTTTTC-3'). A second round of PCR was carried out using the primers Wild-Type PKA-F (5'-CATGCCATGGCAGCAACGCCGCCGCC-3') and Wild-Type PKA-R (5'-CCGCTCGAGCGGCACTCCTTGCCACA-3'). The subsequent DNA sequence encoding T32C PKA variant was then subcloned into the pET28 vector for protein overexpression.

2.2.2. PKA Expression and Purification

The T32C PKA variant was overexpressed in *E. coli* using the following representative protocol adapted from previous reports.[50,51] After transformation of the pET28-T32C PKA plasmid

into BL21 DE3 *E. coli* cells, agar plates supplemented with kanamycin (40 μg/mL) were incubated overnight at 37 °C. The following day, a single transformed colony was inoculated into LB media (5 mL) supplemented with kanamycin (40 μg/mL) and shaken at 37 °C overnight. The starter culture (5 mL) was used to inoculate LB media (1L) before incubation at 37 °C, and the culture was grown to an OD_{600} of 0.8 before induction with 500 μM IPTG. Next, the culture was grown overnight at 23 °C with shaking. The culture was then centrifuged at 6 krpm (4032 g) for 25 min at 4 °C, and the supernatant was decanted. The cell pellet was resuspended in 15 mL low salt lysis buffer (20 mM Tris, 10 mM NaCl, pH 7.2) before cell lysis by sonication. The resultant cell culture was centrifuged at 16 krpm (17203 g) for 45 min at 4 °C. Subsequently, the supernatant was decanted and filtered through a 0.45 μm pore size filter. The cell lysate was applied to a cation exchange column on a BioLogic DuoFlow FPLC. The purified T32C PKA fractions were concentrated by ultrafiltration with a 10 kDa cutoff microconcentrator and applied to a Superdex size-exclusion column. The T32C variant of PKA was eluted in PBS buffer (138 mM NaCl, 2.7 mM KCl, 8.1 mM Na_2HPO_4, 1.5 mM KH_2PO_4, pH 7.2). Another protocol adapted from conversations with Dr. Michael Deal (in Professor Susan S. Taylor's laboratory at the University of California, San Diego) applied weak and then strong cation exchange chromatography for purification.[50,51] As shown by the 15% SDS-PAGE (Figure 2.1), the resultant protein was < 99% homogenous.

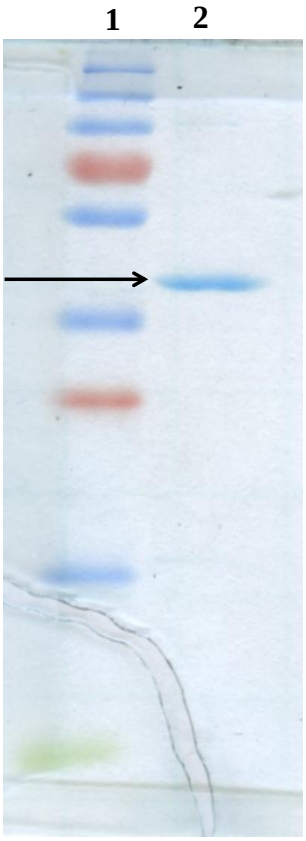


Figure 2.1: Expression and purification of T32C PKA variant. This 15% SDS-PAGE provides an illustrative example of the purity of the expressed PKA variant. The arrow indicates the expected MW for the migration of T32C PKA (41.8 kDa). Lane 1 is the PageRuler Plus Prestained Protein Ladder (Fermentas). Reproduced from [12] .

2.2.3 PKA Activity Assay

In order to confirm that the modification minimal effected catalysis, a PKA activity assay was conducted. The PKA activity assay applied a previously reported protocol.[52] From the results, it can be concluded that wild-type PKA activity is demonstrated by a decrease in absorbance as compared to the absorbance of the reaction with no PKA present. Wild-type PKA activity is similar to T32C PKA activity, as shown in Figure 2.2. This suggests that the modification had minimal effect within error on the enzyme's ability to perform catalysis.

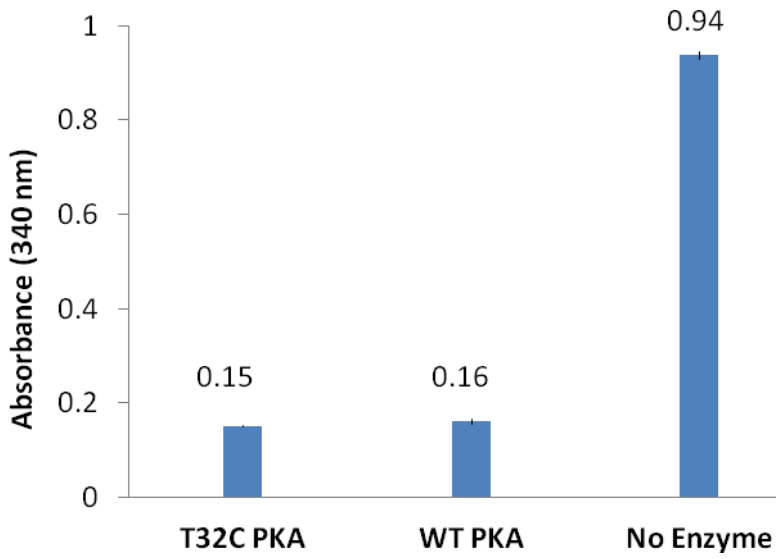


Figure 2.2: A PKA activity assay with the T32C and wild-type PKA variants. A negative control condition with no enzyme present under identical condition showed essentially no activity. Error bars represent standard deviation (n = 3). Reproduced from [12].

2.3 Protein Conjugation

The following will focus predominantly on the protein conjugation procedure for PKA as the conjugation procedure for T4 Lysozyme has been described in detail previously.[11,46,53]

A bi-functional linker molecule, pyrene maleimide, was used to functionalize the SWNT of the device. The pyrene functionality, through pi-pi stacking, adheres strongly to sidewall of SWNT while the maleimide group allows for the formation of a stable thioether bond with the free thiol of a cysteine sidechain in the protein.[54,55] The device was submerged in a saturated solution N-(1-pyrenyl)maleimide (Sigma-Aldrich) in ethanol for 45 minutes without agitation. Following this, the device was rinsed with 0.1% Tween-20 (Acros Organics) in ethanol to remove excess N-(1-pyrenyl)maleimide and then rinsed with de-ionized water.

Protein Kinase A was then conjugated to the SWNT. A solution of Protein Kinase A (52μM) in phosphate buffer (137 mM NaCl, 2.7 mM KCl, 10 mM Na_2HPO_4, 2 mM KH_2PO_4, 2 mM $MgCl_2$, 2 mM ATP, 100 μM TCEP, pH 7.4) was prepared. The $MgCl_2$ and ATP are used to sterically block bonding to cysteines (C199, C343) located near the active site of the protein.[56] The device was soaked in the protein kinase solution for 60 min without agitiation at room temperature. The device was then rinsed with phosphate buffer and soaked in another solution (100 mM NaCl, 20 mM Na_2HPO_4, pH 2.5) for 1 min with gentle shaking to remove non-specifically adsorbed protein from the surface of device. Following this, the device was rinsed and stored in a buffered aqueous solution (100mM MOPs, 9 mM $MgCl_2$, 100 μM TCEP, pH 7.2).

2.3.1 Confirming Protein Conjugation

The outcome of the conjugation procedure was confirmed either before or after electrical measurements. For instances where the conjugation was confirmed before electrical measurements, an atomic force microscope (NT-MDT) was used to image the devices in a protein compatible buffer solution. After measurements, the devices were rinsed thoroughly for 1 – 2 min in deionized water to remove excess salts from the surface, dried using nitrogen, and imaged (AFM, Pacific Nanotechnology Nano-R and NT-MDT). Figure 2.3 (A) shows a representative device before the electron beam resist passivation, with a dashed line outlining where the electron-beam resist will be exposed and developed. Figure 2.3 (B) shows the device after the passivation process and after the protein conjugation step. In this image, two lysozyme attachments can be resolved on the SWNT. Another representative device is shown in Figure 2.3 (C) where there is only a single protein attachment. Line cuts are provided in Figure 2.3 (D) for six devices with protein attachments. The line cuts demonstrate the pyrene-coated SWNTs appear to be 1.5 – 2.0 nm in height, while the protein attachments range from 5 – 10 nm in height. In comparison to the 0.2 to 0.4 nm roughness along the SWNT, the protein attachments are easily distinguishable by AFM.

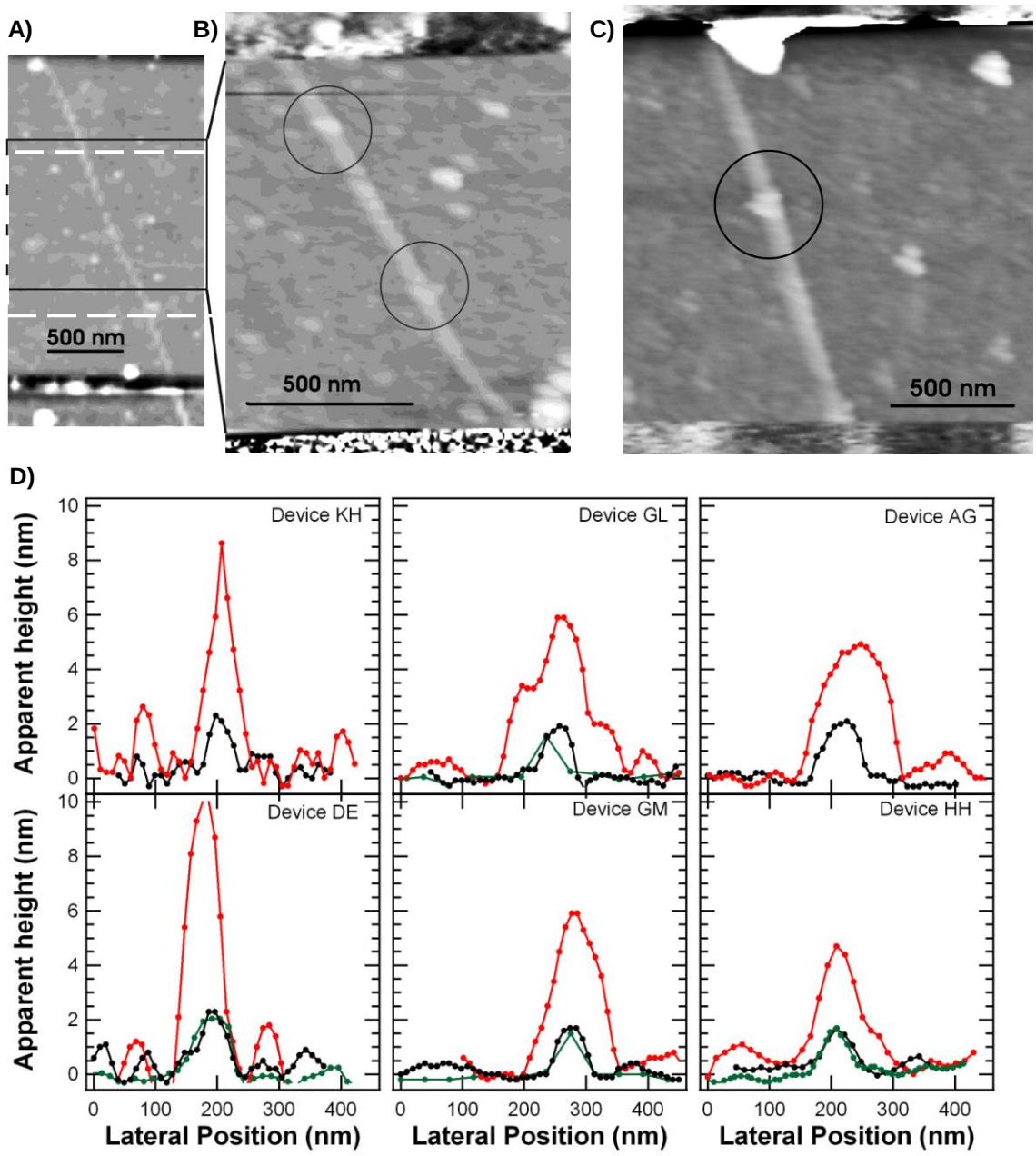


Figure 2.3: Examples of lysozyme device fabrication. (A) AFM image of a bare SWNT device with the target position of the PMMA window indicated (dashed box). (B) A higher magnification image of the same device after bioconjugation, which resulted in two lysozyme attachments (gray circles). Note the larger scale bar, and that the top and bottom edges of the image now correspond to the protective PMMA rather than to metal electrodes. (C) A device with a single lysozyme attachment. (D) AFM line profiles for 6 different devices. Three lines in each image correspond to height profiles taken across the lysozyme attachment (red), pyrene-coated SWNT (black), and pristine SWNT (green). Reproduced from [11].

2.4 T4 Lysozyme Variants

In order to investigate the nature of the transduction mechanism, T4 lysozyme variants with differing charge residues near the attachment site were prepared in the laboratory of Professor Gregory Weiss by Drs. Issa S. Moody and Tivoli J. Olsen. The methods can found in previous reports[11,46,53]. The following is an exhaustive list of each of the T4 lysozyme variants measured:

1. **S90C:** an active variant of pseudo-wild-type T4 Lysozyme where cysteine replaces a serine at the 90-site and the naturally-occurring cysteines have been replaced with a threonine at the 54-site and an alanine at the 97-site.
2. **S36C:** an active variant of pseudo-wild-type T4 Lysozyme where cysteine replaces a serine at the 36-site and the naturally-occurring cysteines have been replaced with a threonine at the 54-site and an alanine at the 97-site.
3. **R119A:** an active variant of S90C where an arginine near the 90-site is replaced with an alanine.
4. **K83A:** an active variant of S90C where a lysine near the 90-site is replaced with an alanine.
5. **K83A/R119A:** an active variant of S90C where a lysine and arginine near the 90-site are both replaced with alanines.
6. **K83E/R119A:** an active variant of S90C where a lysine and arginine near the 90-site are replaced by glutamic acid and alanine, respectively.

7. **K83A/R119E:** an active variant of S90C where a lysine and arginine near the 90-site are replaced by alanine and glutamic acid, respectively.
8. **K83E/R119E:** an active variant of S90C where a lysine and arginine near the 90-site are both replaced by glutamic acids, respectively.
9. **T26E:** an inactive variant of S90C where a threosine at the 26-site is replaced by a glutamic acid. This variant produces a covalent adduct with the peptidoglycan substrate and thus provides a constitutively substrate-bound version of the lysozyme[57].
10. **E11H:** an inactive variant of S90C where a glutamic acid is replaced by a histidine[57].

2.5 Electrical Measurements

All electrical measurements were performed with the active portion of the device submerged in a buffered aqueous solution. The potential of the electrolyte was controlled using Pt counter and reference electrodes, and held at -0.3 V to 0.3 V vs. Pt using a Keithley 2400 sourcemeter. The source-drain bias was held at 100 mV. A Keithley 428 preamplifer operating at 10^7 or 10^8 V/A gain and with a 15 or 40 μs rise time was used to measure the source-drain current of the device, respectively. Data was collected for at least 300 s for each measurement condition.

2.6 Three-level Switching Data Analysis

The addition of another switching level added complexity to the data and thus necessitated improvements in the data processing tools in order to adequately analyze the data sets with more

than two levels. Figure 2.4 shows the graphical user interface of a LabView VI where the duration of all three-level events could be captured and exported to Igor for further data processing.

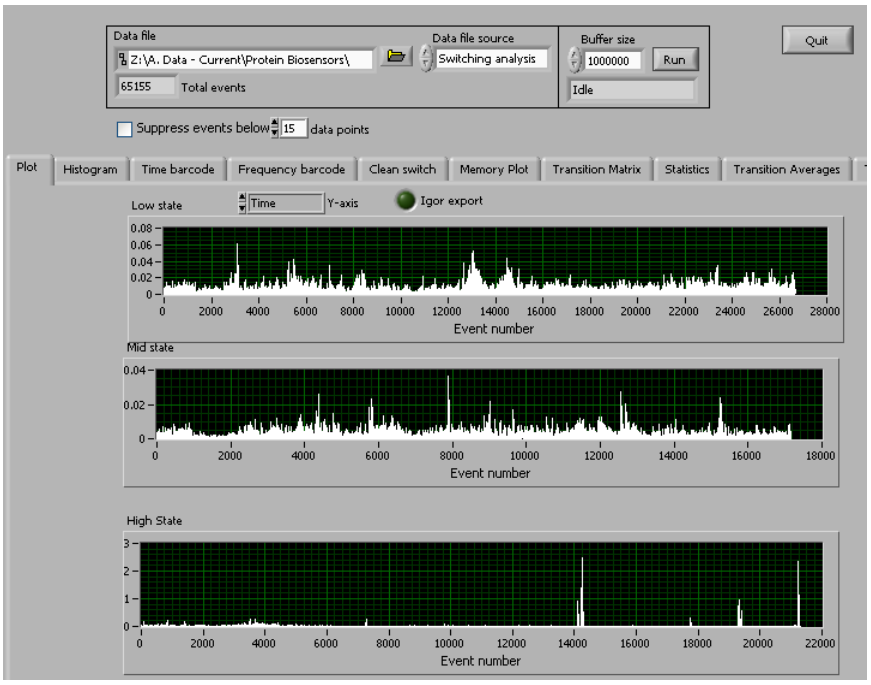


Figure 2.4: Front Panel plotting the duration of the low, middle, and high state events.

With the addition of a third state, transitional information could also be extracted in order to understand how the enzyme transitioned between its various conformational states as shown in Figure 2.5. These matrixes show the percentage of the total switches that corresponded to each transition, the raw number of these transitions, and also the probability of transitioning from one state to another.

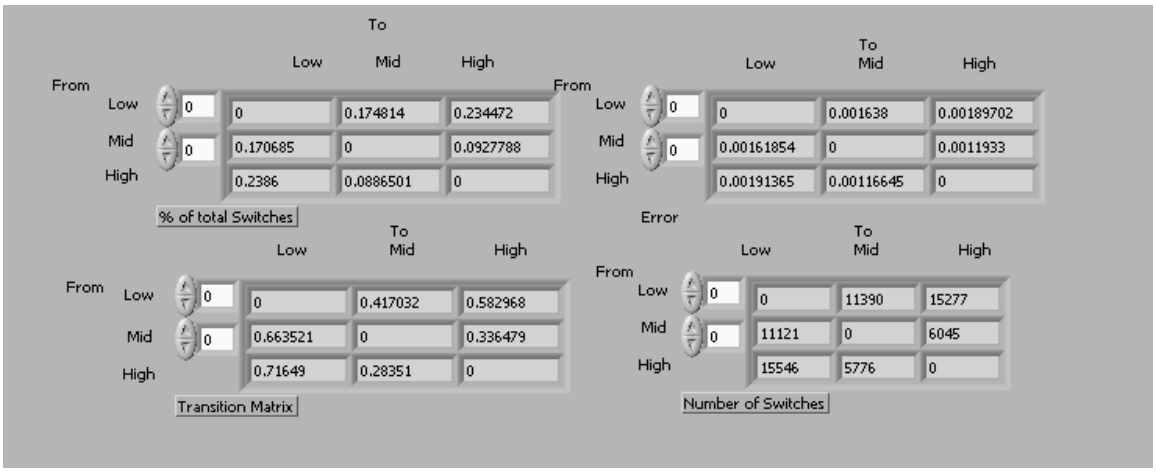


Figure 2.5: Matrices showing the percentage of the transitions with respect to the total number of transitions, the error from counting statistics, the transition probabilities, and the total number of transitions.

To further improve the analysis capabilities, mean, variance, randomness parameter capabilities added to the LabView VI in order to quickly characterize key parameters from the data sets. Figure 2.6 shows these values for each state regardless of what state occurred before and after. Figure 2.7 shows these values for the state that follows after a certain transition. For example, "HL" shows the values of the low-state events that were preceded by a high-state event. This was instituted to determine if the previous state had an effect on the waiting of time of the state that succeeded it. Additionally, it was also useful to consider the average waiting times of events that preceded a certain transition. This capability is shown in Figure 2.8.

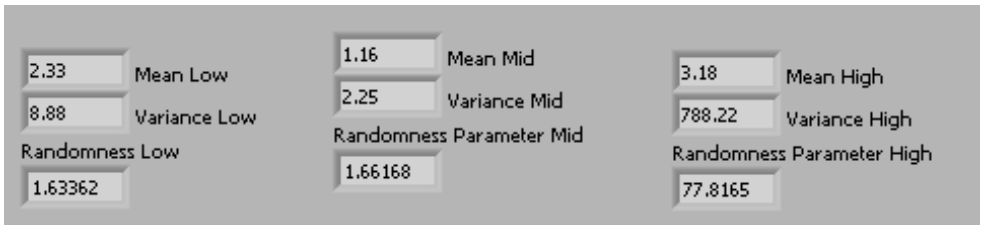


Figure 2.6: The calculated average waiting times, variance, and randomness parameter for the low, middle, and high state events.

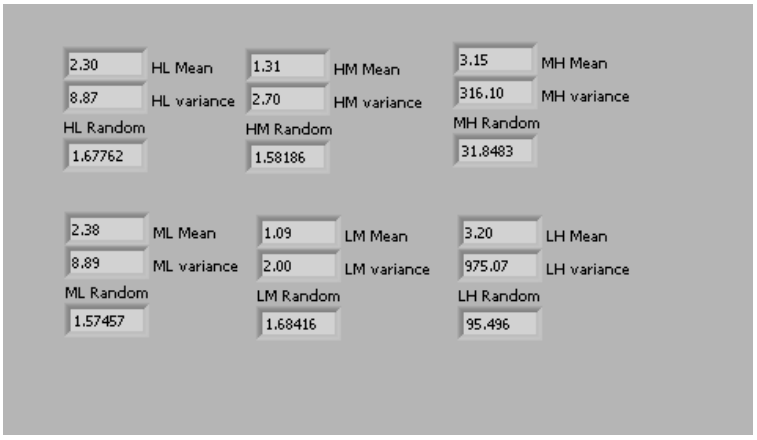


Figure 2.7: The calculated average waiting times, variance, and randomness parameter for the succeeding state of the transition.

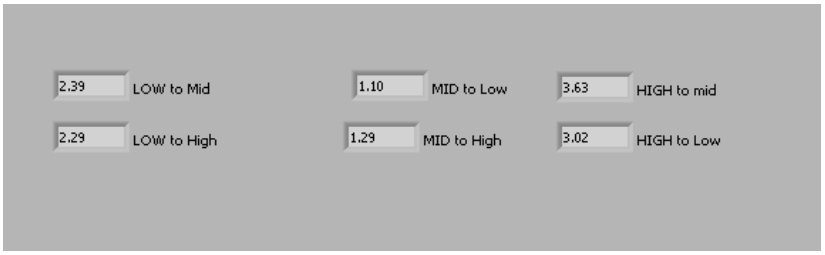


Figure 2.8: The calculated average waiting times for the preceding state of the transition.

To determine the number of steps or the waiting time between certain transitions, a set of histograms was implemented as shown in Figure 2.9. This allowed for the quantification of the number of events or the time that elapsed before the enzyme revisited a certain state or underwent a certain transition.

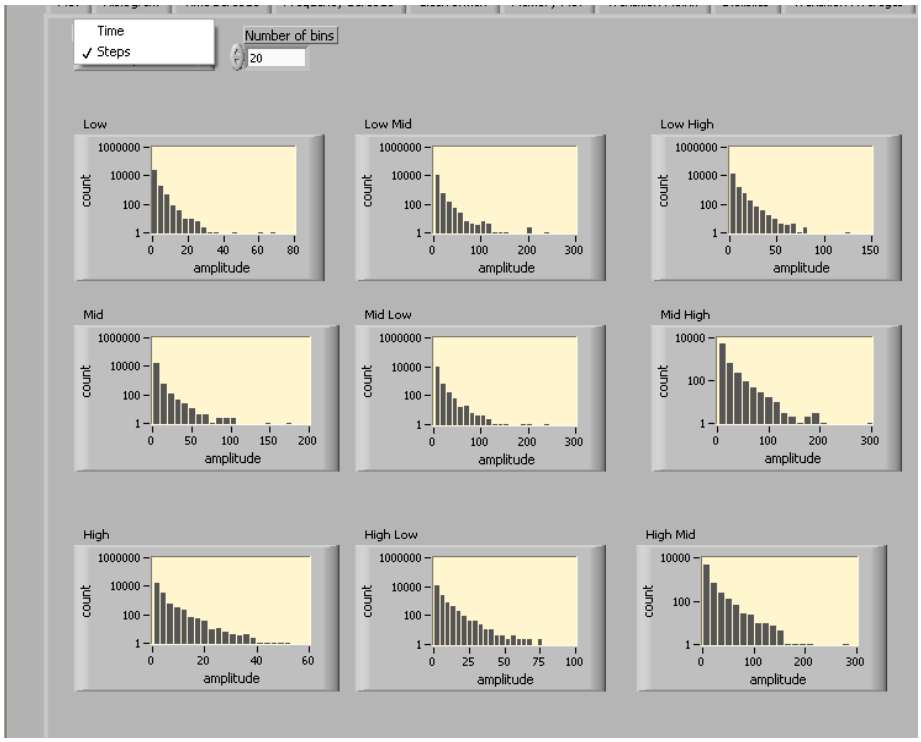


Figure 2.9: Histograms that can show either the number steps or the duration between specific states or transitions.

To track how the mean waiting time of each state varied with time, the mean values of the waiting time could be determined by temporal binning of the data. This capability is shown in Figure 2.10.

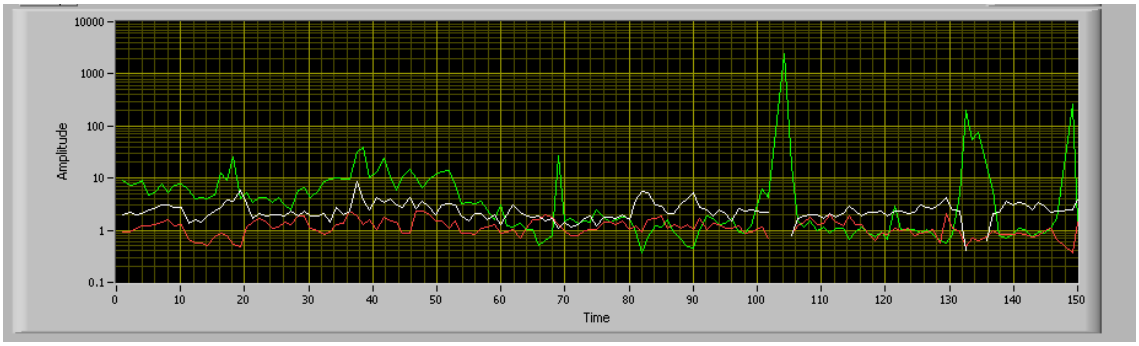


Figure 2.10: Binned-averages versus time of the duration of the low, middle, or high states.

Chapter 3

Protein Conjugation to SWCNTs

In order to use SWCNT sensors to study to the conformational dynamics of individual proteins, a single, active protein must be conjugated to the CNT sidewall. While this has been successfully done, the variation in the conjugation yield under seemingly similar conditions is a limiting factor in the fabrication and measurement of these devices. This chapter will address the experiments conducted seeking to isolate the key sources of variation in the conjugation process.

3.1 The Standard Conjugation Protocol

The conjugation process is a multi-step process with multiple inputs. In general, the process requires three steps. First, the device is submerged in a saturated solution of a bi-functional linker molecule, N-(1-pyrenyl)maleimide (Sigma Aldrich) (pyrene maleimide). Through π-π

stacking, the pyrene functionality of this molecule adsorbs non-covalently on the sidewall of the SWNT, while the maleimide functional group can react with the free thiol of a cysteine residue by forming a stable thioether bond.[54,55] Following this functionalization step is a wash step to putatively limit the number of pyrene maleimide on the device surface and to minimize non-specific adsorption of protein on the oxide surface. The wash step consists of rinsing the device with 0.1% Tween-20 (Acros Organics) b.v. in ethanol and then rinsing the device for 30 seconds with de-ionized water. The last step consists of covering the device with a drop of protein solution (≈ 40 µl) in order to covalently attach a protein molecule to the linker-functionalized SWCNT. In order to stop the reaction, the device is rinsed thoroughly and stored in a salt solution.

Although the process is conceptually simple, there are multiple tunable inputs, dependencies, and measurement considerations that add complexity in determining the important factors in the conjugation process. Some of these tunable inputs are the concentration of the protein in solution, the device incubation time with the protein, and the presence or absence of a surfactant such as Tween-20 in the incubation step. Because of inherent interdependence of the conjugation process on multiple inputs, it is often difficult to isolate which step in the process is limiting the conjugation yield. The success of the entire process is dependent on the success of sequential steps in the process. For example, the first step requires that the pyrene maleimide molecules adsorb onto the side wall of SWCNT while still retaining their reactivity. The rinse step requires that the Tween-20 surfactant removes excess pyrene maleimide molecules, that the surfactant blocks non-specific adsorption of protein on the oxide surface, and that the surfactant allows the maleimide to still react with the thiol group of the protein. The conjugation step

requires that the maleimide group reacts preferentially with the cysteine residue of the protein, that the protein is free from excessive aggregation, that the protein does not coat the surface non-specifically inhibiting the maleimide reaction. If any of these things fail to occur, their effect will cascade throughout the process.

In practice, instrumental, technical, and sample limitations prohibit the investigation of each individual step independently, and, instead, the whole conjugation process is conducted with slight modifications in order to elucidate their effects. To characterize the devices before and after the entire process, tapping-mode atomic force microscopy is used to observe the surfaces of the device topographically.

3.2 Effects of High Protein Concentration on Conjugation

Following the protocol for the SWNT conjugation process from previous reports yielded dramatically varied results from the expected 0.5 attachments per um of exposed SWCNT sidewall. This variation suggests that uncontrolled parameters fill dominant roles in the process of conjugating single proteins to SWCNTs. In order to reproducibly and repeatedly generate usable, functionalized devices, it is imperative to determine and control these unknown factors. As an example, Figure 3.1 (A) shows representative AFM micrographs before and after the standard attachment protocol using PBS with 54μM T4 Lysozyme. These images are in contrast to previous images that show prominent and obvious protein conjugation to the SWCNT as seen in Figure 2.3. Comparing the before and after images of Figure 3.1 (A) confirms that there are no specific attachments of lysozyme to the sidewall of the SWCNT and that the most prominent

difference between the two images is an increase in the roughness of the oxide surface which may be due to non-specific adsorption of protein or protein fragments from solution. This lower yield of conjugation is indicative of an interfering factor that limits the maleimide-thiol reaction.

In order to determine if this interference could be diminished, protocols were conducted using the standard protocol with modifications to the protein concentration as well as the conjugation duration. Comparing Figure 3.1 (A) and (B) demonstrates that increasing the concentration of lysozyme from 54 µM to a nearly saturated concentration of 120 µM has a negligible effect on the conjugation yield. This result suggests that the protein concentration is already in excess at 54 µM with respect to the accessible maleimide groups and that further increasing the concentration provides no tangible benefit in promoting the conjugation reaction. Similarly, the comparison between Figure 3.1 (A) and (C) confirm that increasing the duration of conjugation step using a 54 µM lysozyme solution from 45 minutes to 90 minutes is ineffective in improving the yield. Taken together, Figures 3.1 (A-C) allude to pyrene maleimide molecules that are either inaccessible, absent, or unreactive.

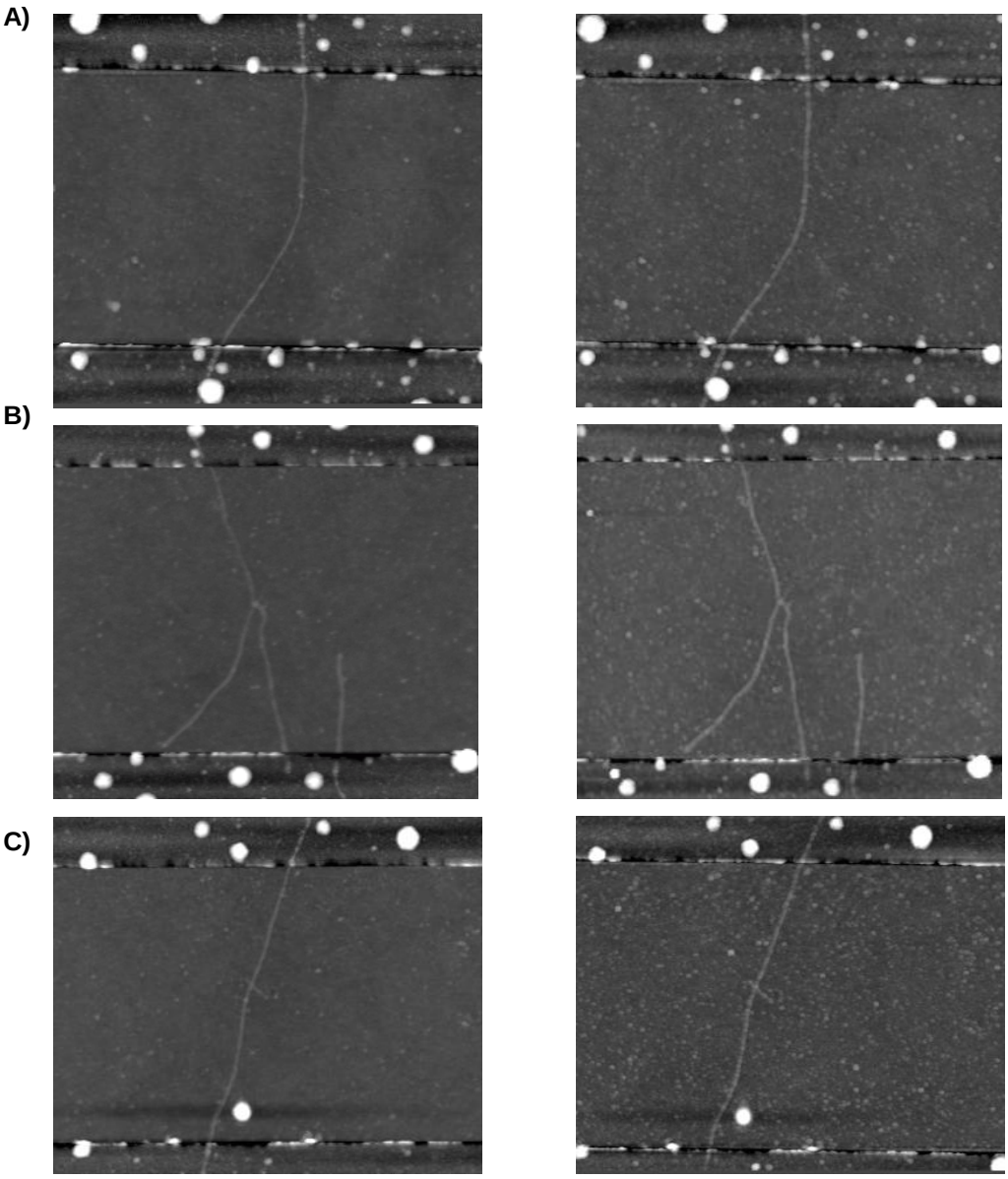


Figure 3.1: Comparing the effects of time and concentration for lysozyme conjugation using standard conjugation protocol. (A) AFM micrographs before (left) and after(right) a 45 minute conjugation using 54 µM T4 Lysozyme. (B) AFM micrographs before (left) and after (right) a 45 minute conjugation using 120 µM T4 Lysozyme. (C) AFM micrographs before (left) and after (right) a 90 minute conjugation using 54 µM T4 Lysozyme. (Samples (A) AKC42-IF 30ac, (B) AKC42-GH 03bd, and (C) AKC42-GH 10eg)

3.3 Effects of Contamination and Defects on the Conjugation Process

One factor that could limit the availability of pyrene maleimide in reaction is the cleanliness of the nanotube sidewall. Before the conjugation procedure, the SWCNTs undergo a number of processing steps in order to form electrolyte compatible electronic devices. These processing steps involve the deposition and removal of polymer films such as PMMA, Lift-Off Resist and Shipley 1808 that physically contact the SWCNT. It has been shown experimentally that chemically dissolving these films leaves behind insoluble, residual contamination on SWCNT and graphene devices, but that thermal treatments in air[58] or Argon/Hydrogen[59,60] environments assist in at least the partial removal of this contamination. Without the adequate removal of this contamination, it is conceivable that this contamination may limit the availability as well as compatibility of sites along the nanotube sidewall that are necessary for the π-π stacking interaction of the pyrene functional group to occur.

Initially to address the concern that the photolithography process leaves behind residual contamination that may affect the ability of the pyrene maleimide molecules adsorbing to the nanotube sidewall, thermal treatments were conducted in air at 300 °C for 30 minutes. This treatment has been used to before to improve the conductivity of CNTs by putatively desorbing cresol molecules from the nanotube sidewall.[58] Figure 3.2 (A) shows atomic force micrographs before and after conjugation of a solution containing 120 μM T4 Lysozyme without a thermal treatment. These images resemble those of Figure 3.1 (B) as there do not appear to be any attachments to the sidewall and there also additional small particles randomly dispersed on the surface. Figure 3.2 (B) shows the effect of a 300° C thermal treatment in air for 30 minutes.

Similar to that of Figure 3.2 (A), Figure 3.2 (B) shows no attachments to the sidewall, but the surface, in contrast, is apparently smoother than even the pre-conjugation image. This decrease in roughness will be discussed later but it may be due to a more uniform and ordered layer of particulates adsorbing onto the oxide surface following the thermal treatment. Regardless, the thermal treatment of the devices had no observable effect on the attachment yield and suggests that the thermal treatment was either insufficient in removing the contamination or that other factors beyond the effects of residual resist impede protein conjugation.

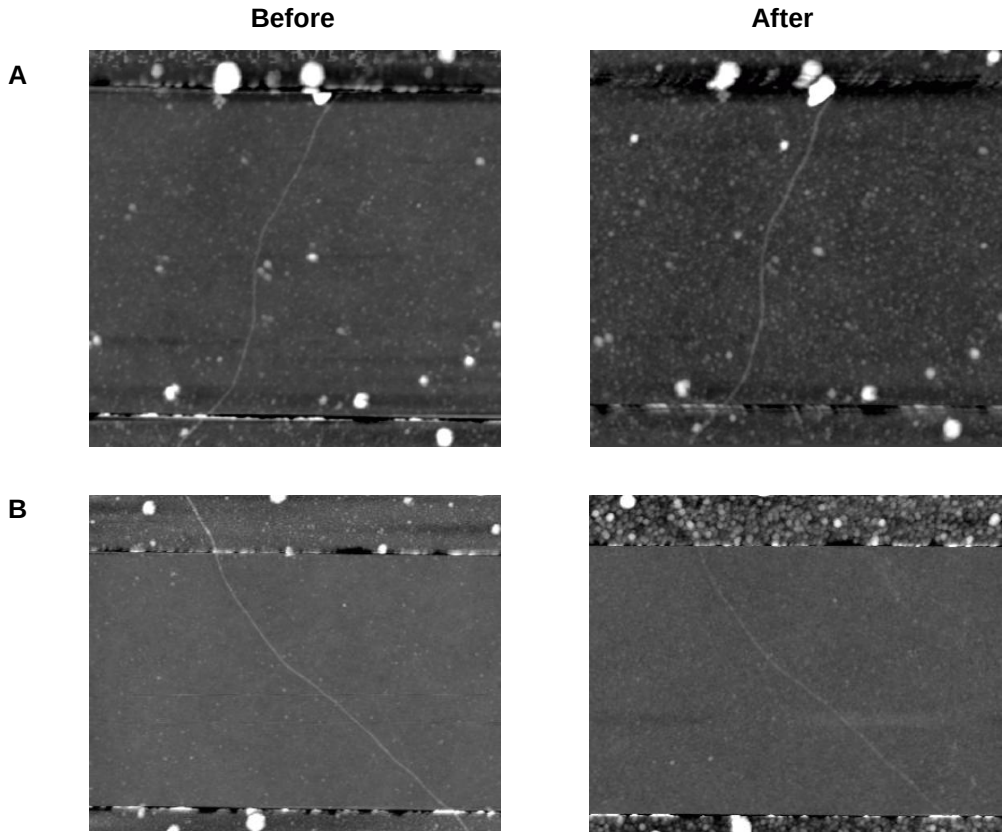


Figure 3.2: AFM micrographs comparing the effect of a thermal treatment versus no-treatment using a 30 minute conjugation with 120µM T4 Lysozyme. (A) AFM micrographs before (left) and after (right) after conjugation without thermal treatment. (B) AFM micrographs before (left) and after (right) conjugation with a thermal-treatment of 300 °C for 30 min. (Samples (A) AKC42-JD 20eg and (B) AKC42-DE 20ab)

To further test the hypothesis that contamination originating from the clean room processing was impeding protein conjugation, SWCNTs were grown from patterned alumina islands covered with catalyst with no additional processing steps. This ensured that the SWCNTs were absolutely free from polymer-based contamination that could interfere with the adsorption of pyrene maleimide to the SWCNT sidewall. Also this patterning of catalyst allowed for the same surface area to be observed using atomic force microscopy before and after the conjugation process to evaluate any change along the SWCNTs or on the surface.

Figure 3.3 shows the results of the conjugation process conducted on the as-grown nanotubes. The devices shown in Figure 3.3 (A) and (B) show the results of an incubation using 50 nM T4 Lysozyme solution for 17 hours without a Tween-20 rinse. From Figure 3.3 (A) and (B), there is an increase in the number of particles on the surface and also a corresponding increase in the surface roughness. Although additional particles appear to be on the surface, none appear to be localized on the nanotube, but they instead appear to be randomly distributed on the surface. However, there does appear to be an apparent increase in the diameter of the SWCNTs ranging from 0.5 nm to 2.0nm. Figure 3.3 (C) shows similar results even after just 15 minutes in a 50 nM T4 Lysozyme solution. This suggests that the particles from solution rapidly and non-specifically adsorb onto the surface. The apparent change in diameter could be explained by the pyrene maleimide or the protein itself is adsorbing to the sidewall of the nanotube. The range in diameters however makes it difficult to discern between the two.

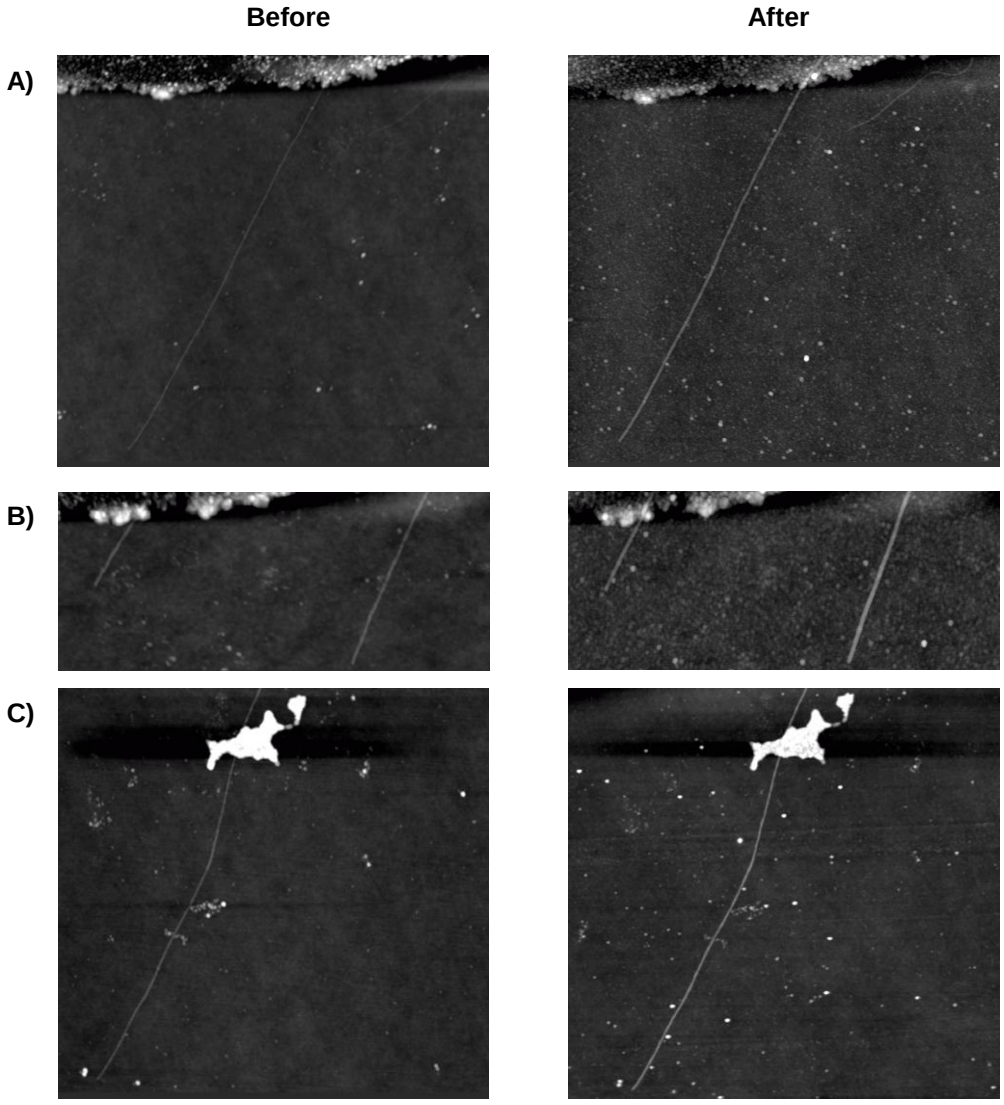


Figure 3.3: AFM micrographs examining the effect of the conjugation process on as-grown SWCNTs. (A) AFM micrographs before (left) and after (right) conjugation using a 50 nM T4 Lysozyme solution for 17 hours. (B) AFM micrographs before (left) and after (right) conjugation using a 50 nM T4 Lysozyme solution for 17 hours. (C) AFM micrographs before (left) and after (right) conjugation using a 50 nM T4 Lysozyme solution for 0.25 hours. (Samples (A & B) Alumina G5, and (C) Alumina G5b)

Furthermore similar conjugation tests were conducted with cAMP-dependent protein kinase (PKA). Figure 3.4 shows the atomic force micrographs before and after a conjugation with 100 nM PKA for 2 hours on the as-grown SWCNTs. Similar to Figure 3.3, the SWCNTs showed a

similar increase in diameter of 1 to 2 nm even though a PKA molecule is nearly twice the mass of T4 Lysozyme. Therefore, this apparent diameter is suspected to be due to pyrene maleimide adsorption and possible dimerization on the sidewall.

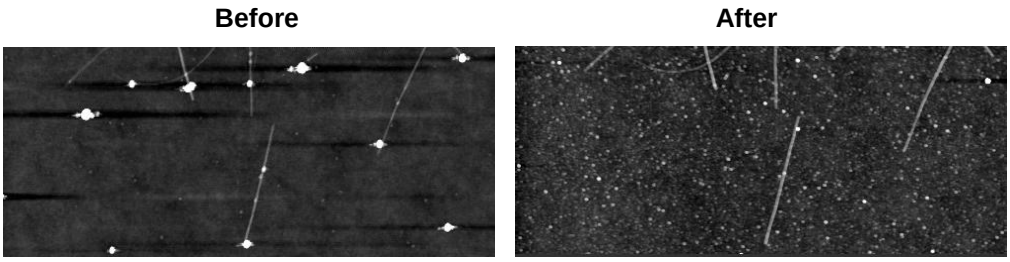


Figure 3.4: AFM micrographs examining the effect of the conjugation process on as-grown SWCNTs before (left) and after (right) conjugation using a 100 nM PKA solution for 2 hours. (Sample W158 F17 Alumina Island)

Exposing carbon nanotubes to UV/Ozone can introduce reversible defects into the sidewall of a carbon nanotube that may affect the ability of protein to conjugate to the sidewall of the nanotube. Theoretically studies have suggested that the defects may interfere with the ability for pyrene to π-π stack on the nanotube sidewall[61], but they have been shown to have enhanced reactivity[62]. Here we investigated the effects of UV/Ozone introduced defects to examine if defects in the nanotube serve a prominent role in conjugation process.

Figure 3.5 provides evidence that defects introduced using UV/Ozone have an insignificant effect on the conjugation process and that the enhanced reactivity of these sites does not promote specific adsorption of T4 lysozyme to the sidewall. This is reasonable as defects in the sidewall theoretically should make the π-π stacking energetically unfavorable, should have minimal effect

on the maleimide-thiol reaction, and should be unable to covalent bind without additional chemical modifications to the functional groups introduced at the defect site.

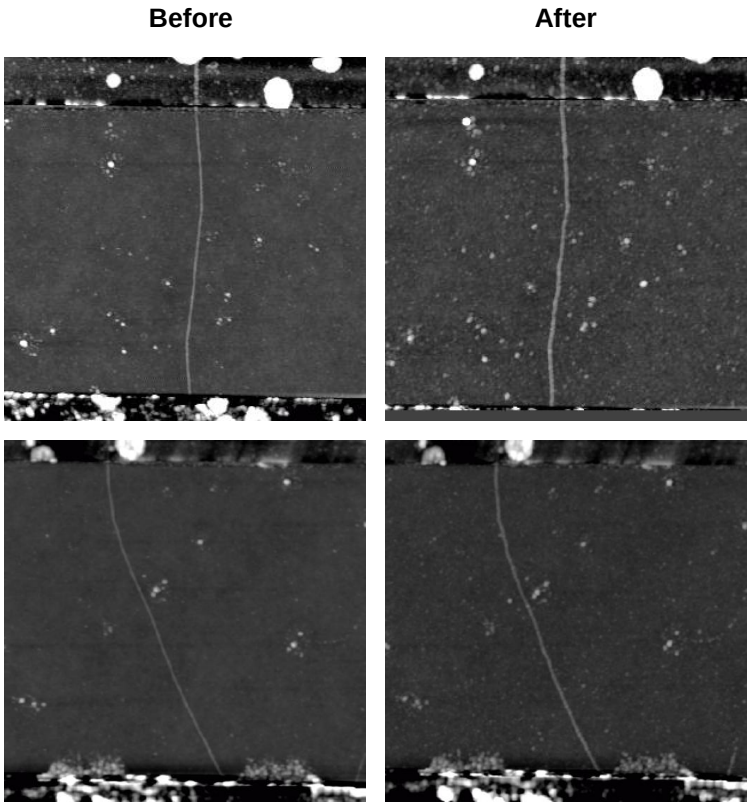


Figure 3.5: AFM micrographs before and after in conjugation using 50 nM T4 Lysozyme for 18.5 hours following UV/Ozone treatment. (Samples AKC48-DE 22de and 22ef)

3.4 Effects of Tween-20 on the Conjugation Process

The previous experiments suggest that the cleanliness of the nanotube sidewall does not appear to be the limiting factor in the conjugation process. While a nanotube surface free of residual resist contamination should improve the density of pyrene maleimide molecules adsorbed, a failure to see any enhancement implies that there are a limited number of pyrene maleimide

molecules in solution that can adhere to the nanotube or that there is an abundance of pyrene maleimide molecules adsorbed to the sidewall but that they are either inactive or inaccessible.

A maleimide functional group can become physically inaccessible if another molecule covers or self-assembles on the surface of the nanotube or oxide. This inaccessibility is reasonable considering that proteins such as hen egg-white lysozyme can form mono- and multilayers on surfaces.[63,64] Furthermore, surfactants such as Tween-20 have been shown to hydrophobically adsorb onto CNTs and oxide surfaces thus preventing non-specific protein adsorption.[65] It follows that the formation of protein layers or the adsorption of Tween-20 onto the nanotube sidewall may limit the accessibility of the maleimide functional group to interact with the cysteine residue of the protein.

To test the effect of Tween-20 on the conjugation step, the Tween-20 rinse was removed from the conjugation process. Figure 3.6 shows the effect of removing the Tween-20 rinse after the pyrene maleimide incubation step with devices that were and were not thermally-treated. For the thermally-treated device as seen in Figure 3.6 (A), the surface appears to have additional aggregates, fibrils, and particulates that have nearly buried the nanotube. This is in contrast to Figure 3.2 (B) where the thermally-treated tube with the Tween-20 rinse is still clearly visible. Figure 3.6 (B) shows a non-thermally-treated tube without the Tween-20 rinse. Comparing Figure 3.6 (B) with Figure 3.2 (A) shows a subtle difference. Figure 3.6 (B) contains regions that appear as divots in the topography. These divots are not visible in the before image and may be due to the monolayer formation of protein on the surface.

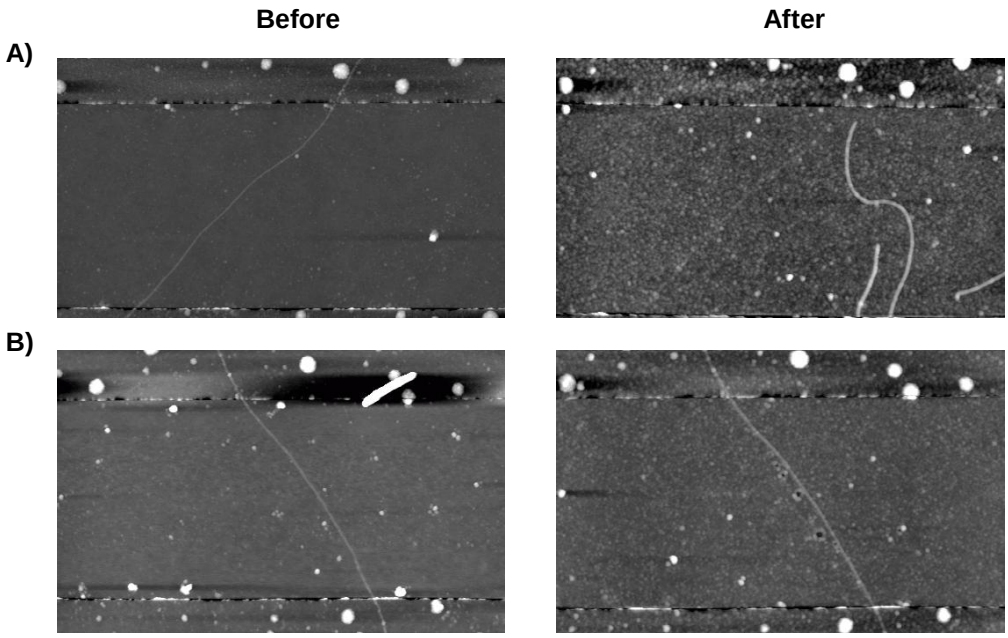


Figure 3.6: Comparison of conjugation on (A) thermal-treated (T = 300° C; 30 min; air) and (B) non-treated devices without a Tween-20 rinse and with 120 μM T4 Lysozyme for 90 minutes. (Samples (A.) AKC42-FB 00ab, and (B.) AKC42-FD 20bc)

While divots in Figure 3.6 (B) provide some evidence for the formation of protein layers, Figure 3.7 further solidifies this hypothesis even with the Tween-20 rinse. Figure 3.7 (A) shows the results before and after a standard protein conjugation using a concentration of ≈ 50 μM of T4 Lysozyme for 45 minutes. These images confirm that particles originating from the protein solution are obfuscating the tube. In support of this, the effect appears to scale with concentration and the conjugation duration as seen from Figure 3.7 (A-D). As the concentration and time in solution decreases, the tube is more visible by atomic force microscopy. These results implicate that the protein concentration and conjugation duration could have a prominent effect in limiting the accessibility maleimide groups to form covalent bonds with the protein. It also provides evidence that the Tween-20 rinse is insufficient in preventing non-specific

adsorption.

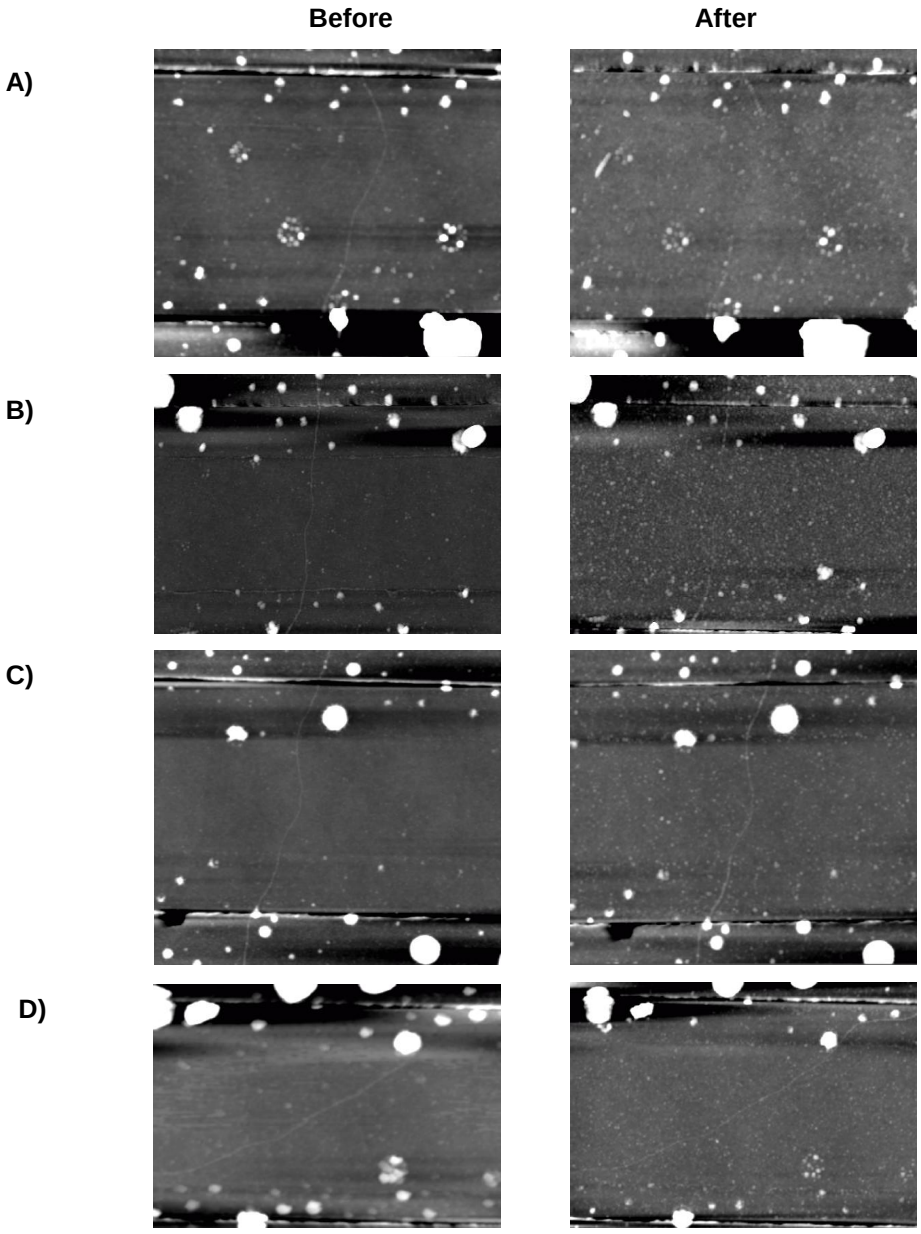


Figure 3.7: Comparing the effects of protein concentration and time using standard lysozyme attachment protocol. (A) AFM micrographs before (left) and after(right) a 45 minute conjugation using ≈ 50 μM T4 Lysozyme. (B) AFM micrographs before (left) and after(right) a 30 minute conjugation using ≈ 25 μM T4 Lysozyme. (C) AFM micrographs before (left) and after (right) a 30 minute conjugation using ≈ 5 μM T4 Lysozyme. (D) AFM micrographs before (left) and after (right) a 90 minute conjugation using ≈ 5 μM T4 Lysozyme. (Samples (A) AKC47-LF 31fh, (B) AKC47-HL 10ac, (C) AKC47-JL 00ce, and (D) AKC47-GJ 11fh)

More obvious evidence of protein is coverage can be seen when conducting the conjugation process with camp-dependent protein kinase (PKA). Figure 3.8 (A) shows the effect of the standard conjugation protocol and with a modification that introduces Tween-20 into the protein conjugation step. The top die in Figure 3.8 (A) provides visual verification of protein adsorption due to the localized color change from thin-film interference due to the build-up of protein on the surface. This layer formation is ameliorated with the addition of 0.1% Tween-20 to the protein solution as seen in the bottom die of Figure 3.8 (B). Even at concentrations of 13 μM and 4μM the protein readily adsorbs to onto the oxide surface as seen in Figures 3.8 (B and C), respectively, where the tube is no longer visible after the conjugation process without Tween-20 present. With the addition of Tween-20 into the conjugation step, there is a significant reduction in the non-specific adsorption. There also appears to be some particles on the nanotube which may suggest that Tween-20 does not completely block protein conjugation to the nanotube.

Similar tests were conducted using T4 Lysozyme to establish if Tween-20 during the conjugation step enhanced the conjugation yield by preventing the non-specific coverage of lysozyme on the surface. Even with the addition of Tween-20 in the conjugation process Figure 3.9 (A) shows the gradual build-up of non-specifically bound protein after 45 minutes and 90 minutes with 54 μM T4 Lysozyme. As seen from Figure 3.9 (B), 18 μM T4 Lysozyme still adsorbs non-specifically on the surface. In comparison with the results found in Figure 3.1, the results in Figure 3.9 are quite similar with regards to the additional particulates on the surface, but when compared to Figure 3.7, Figure 3.9 shows a significant improvement. Even with the addition of Tween-20 in the conjugation step, there is still a considerable amount of protein on the surface.

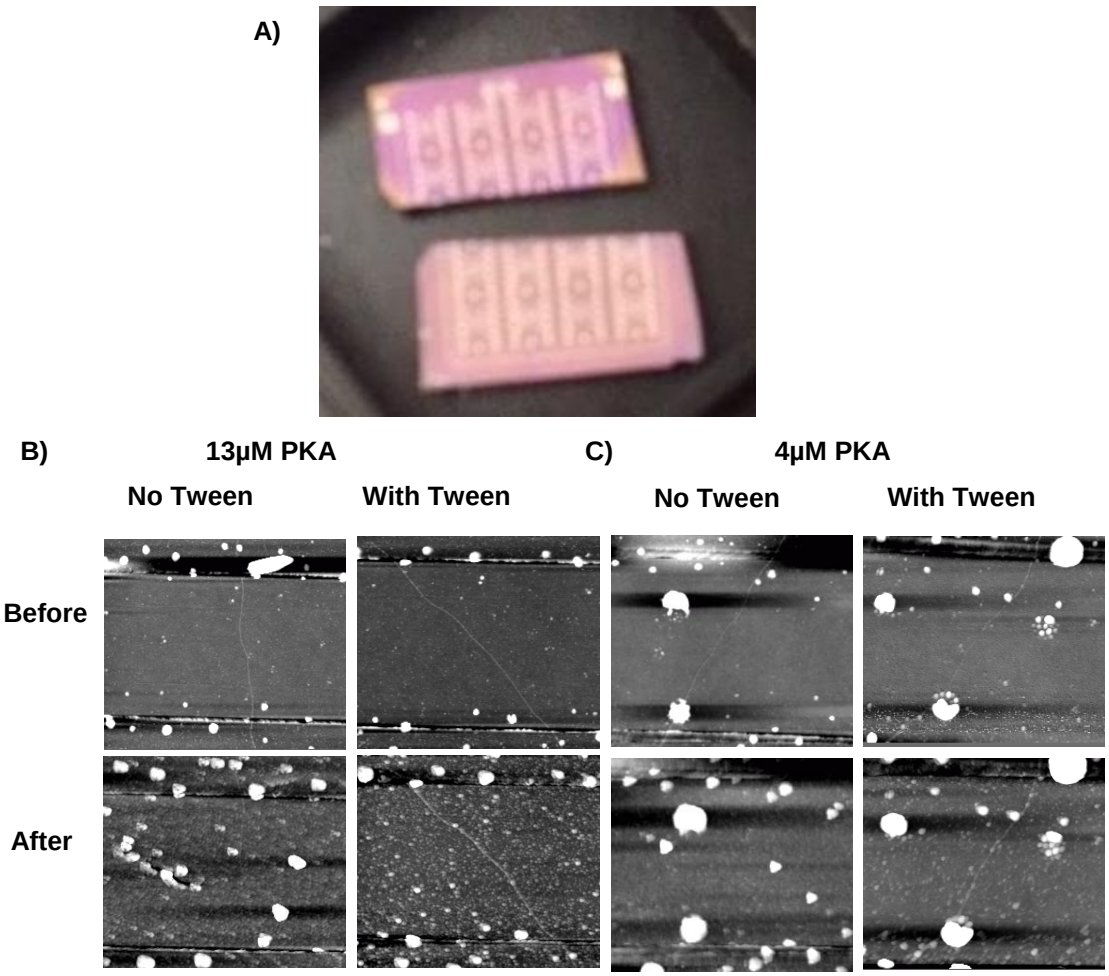


Figure 3.8: Demonstration of the effectiveness of using Tween-20 during the conjugation step of PKA in order to prevent surface adsorption. (A) A photograph contrasting the absence (top) and presence (bottom) of 0.1% Tween-20 in the protein conjugation step. In the absence of Tween-20, PKA effectively adsorbs to the chip surface and is visually evident by the localized color change due to thin-film interference. (B) AFM micrographs contrasting before (top) and after (bottom) a 45 minute conjugation with 13 μM PKA with and without 0.1% Tween-20 present. (C) AFM micrographs contrasting before (top) and after (bottom) a 45 minute conjugation with 4 μM PKA with and without 0.1% Tween-20 present. (Samples (A) AKC42-BH, (B) AKC42-GG 10ce and 13fh, and (C) AKC47-CC 10ab and 02ef)

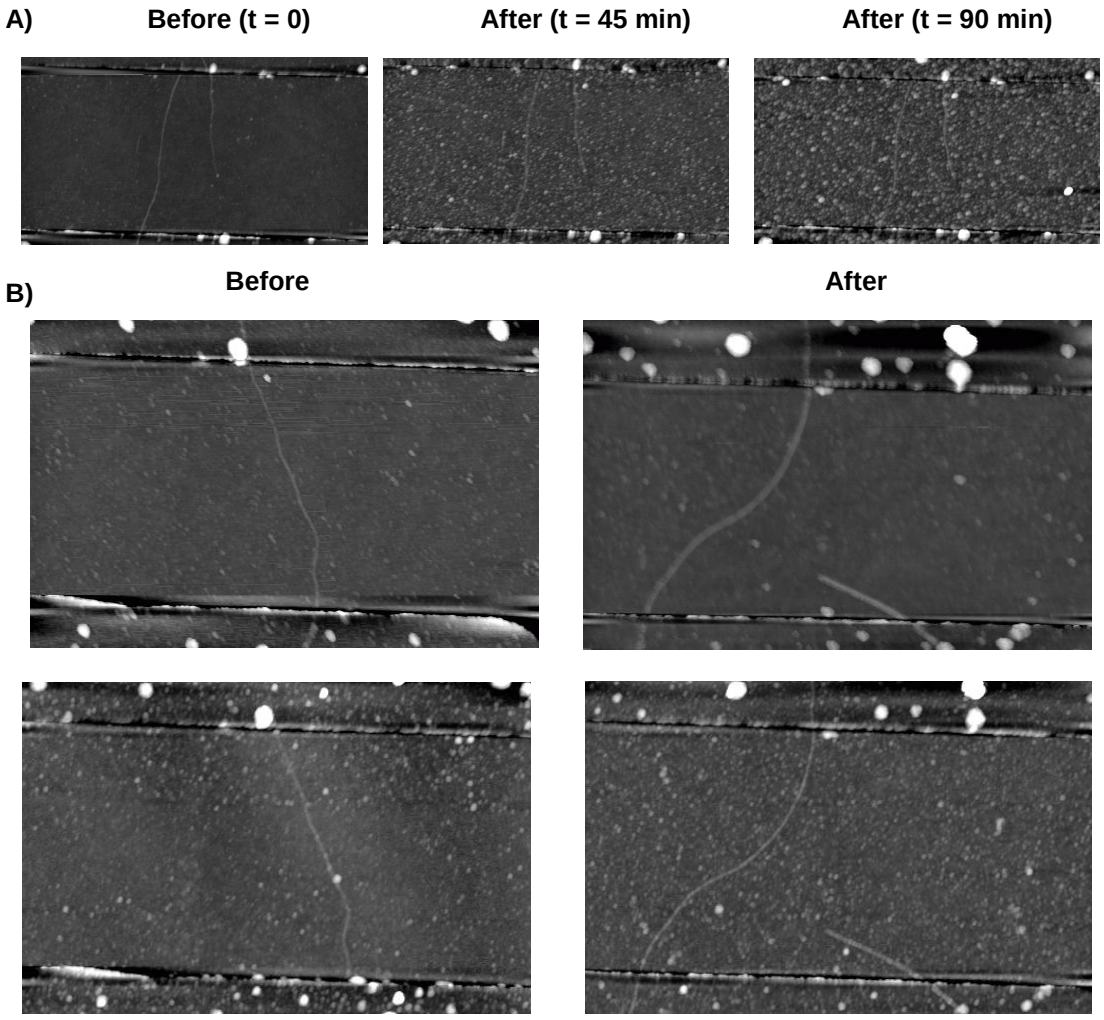


Figure 3.9: Comparing the effects of concentration with 0.1 % Tween-20 in the conjugation solution of T4 Lysozyme. (A) AFM micrographs before (left), after 45 minutes (center), and 90 minutes (right) for a 54 µM of T4 Lysozyme. (B) AFM micrographs before (left) and after (right) a 45 minute conjugation with an 18 µM solution of T4 Lysozyme. (Samples (A) AKC42-AF 22ef, (B) AKC42 AF 03ef, and 02gh)

3.5 Effects of Long Duration and Low Protein Concentration

One way to thwart the coverage effects of high concentrations is to use low concentrations for long-time. This has precedent as researchers have used this approach to functionalize graphene.[66] Figure 3.10 shows three devices with 50 nM solutions of T4 Lysozyme imaged using atomic force microscopy at different times. It shows the build-up of particles over the course of the incubation. Comparing the images over the course of the incubation revealed that the particles on the surface are non-stationary suggesting that the particles can either migrate on the surface or diffuse back into solution. Additionally after 18.5 hours in solution, the surfaces begin to have aggregates forming or depositing on them. This can due to surface mediated aggregation on the surface or that proteins are beginning to aggregate in solution after being at 25 °C for 18.5 hours. What is evident from these images is that even after an hour there are some particles adhering to the chip surface even at concentrations 1000x less than the original protocol of 50 µM. However there is still a low yield on proteins specifically conjugated to the CNT sidewall which again suggests that reaction is still being limited.

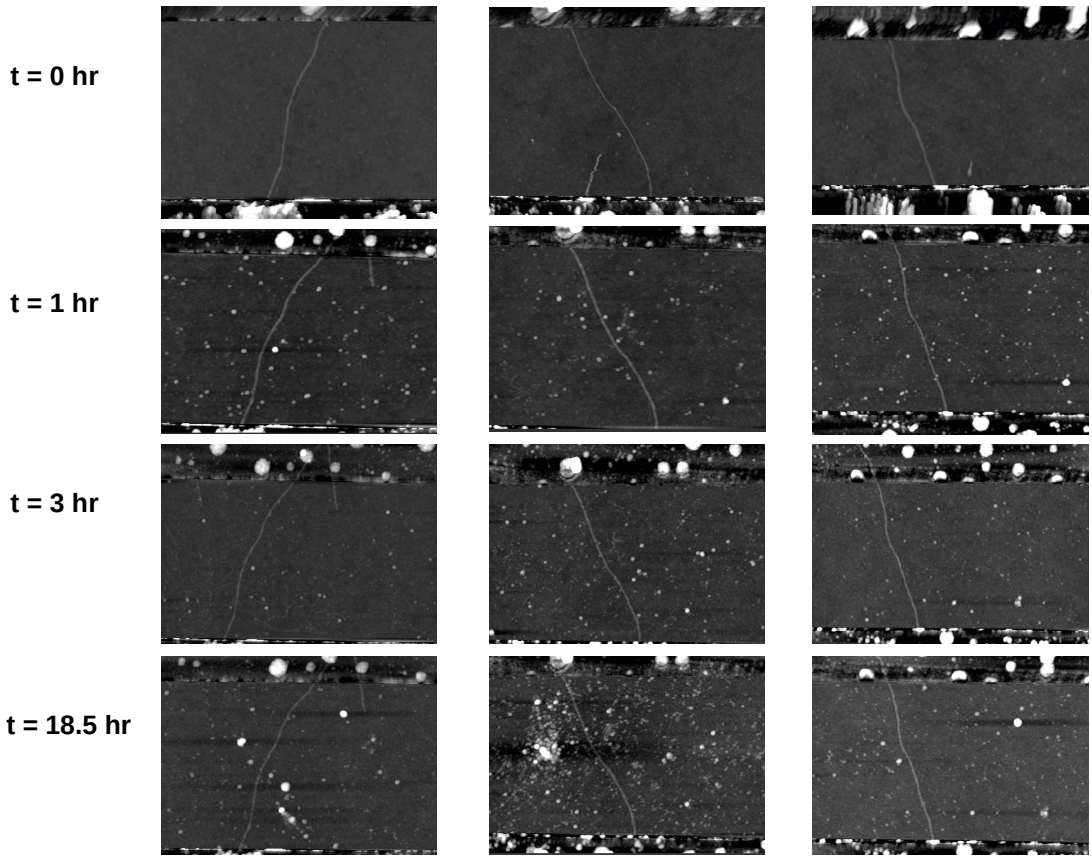


Figure 3.10: Time-dependent adsorption of T4 Lysozyme for three devices at time stamps of 0, 1 hr, 3hr, and 18.5 hr with a 50 nM T4 Lysozyme solution. (Samples AKC48-FL 10gh, 31ef, and 32ef)

The Klenow Fragment of DNA Polymerase 1 appears to have higher stability and is larger than lysozyme making it more amicable for atomic force microscopy imaging and for long duration conjugations. Figure 3.11 shows the results of conjugation Pol1 to thermally treated devices (300 °C, 40 minutes, air) in the absence of a Tween-20 rinse. Figure 3.11 (A) shows the results of the conjugation using 300pM Pol1 for 16 hours and shows very little non-specific protein adsorption even in the absence of a Tween-20 rinse before the conjugation step. Also there appear to be visible attachments of protein to the sidewall. Figure 3.11 (B) shows 3 nM Pol1 for

the same amount of time and appears similar. Interestingly, the attachment yield remained constant with the increase in concentration. This suggests that even with reduced coverage of protein the accessible pyrene maleimide molecules are inactive and unable to form thioether bonds. This attachment procedure of Figure 3.11 (A) was repeated as seen in Figure 3.11 (C) and showed similar conjugation yields.

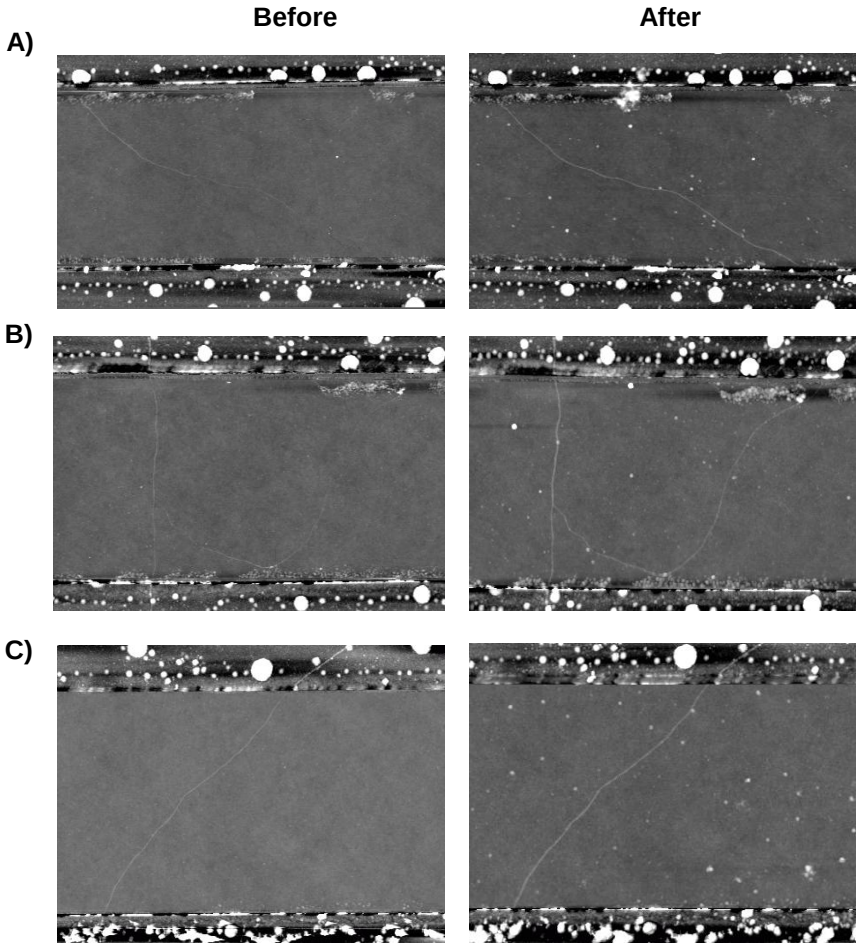


Figure 3.11: Conjugation of Klenow Fragment on thermally-treated devices without Tween-20. (A) AFM Micrographs before (left) and after (right) of 300 pM of Klenow Fragment for 16.5 hours. (B) AFM Micrographs before (left) and after (right) of 3 nM of Klenow Fragment for 16.5 hours. (C) AFM Micrographs before (left) and after (right) of 300 pM of Klenow Fragment for 20 hours. (Samples (A) AKC48-AJ 33ab, (B) AKC48-AJ 20ef, and (C) AKC48-DL 31de)

3.6 Effects of Solution-dependent Variation on Conjugation

One of the difficulties in achieving repeatable and reproducible results arises from solution dependent variablilty. This variability arises as the protein ages and can be due to disulfide bonding, oxidative processes, protease activity, and cascading aggregation in solution. Figure 3.12 (A) shows 50 nM of T4 Lysozyme for 18.5 hours. Figure 3.12 (B) shows 100nM Lysozyme for 17 hours. Figure 3.12 (C) shows 250 nM for 16 hours. From Figure 3.12 it is evident that the variability caused by these solution-dependent processes can dominate even the effects of a 5-fold change in concentration. As demonstrated from these images, the protein stability in solution plays a critical role in being able to achieve reproducible results. The time-dependence of the solutions is additional complication in being able to get repeatable and reproducible attachment to the CNT sidewall. This result conveys the importance of characterizing and using the solutions quickly in order to mitigate the effect of these aging processes.

Figure 3.13 gives another example of the variability. Figure 3.13 (A) fibrils have formed in solution and have deposited onto the oxide surface. In Figure 3.13 (B), a freshly purified solution of the same concentration was used yielding drastically different results. In order to overcome this obstacle, protein solutions should be freshly prepared and purified before attachment.

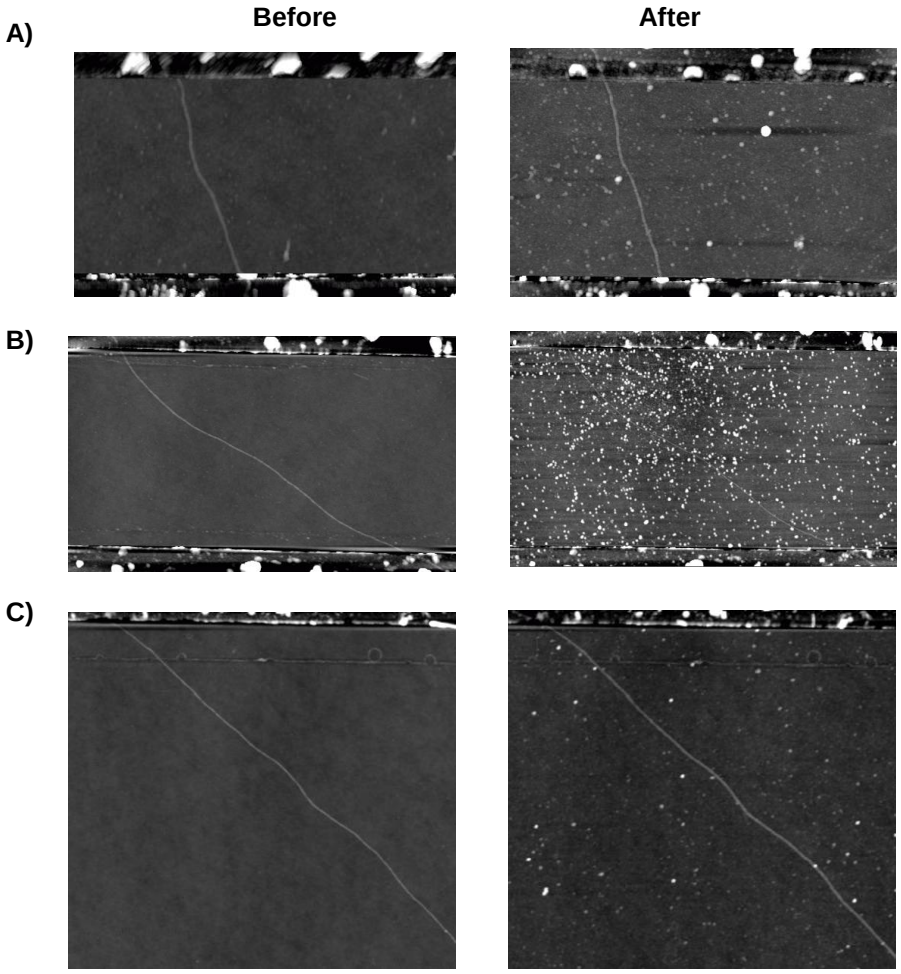


Figure 3.12: Variability of long duration conjugation of T4 Lysozyme. (A) AFM micrographs before (left) and after (right) an 18.5 hour conjugation with 50 nM T4 Lysozyme. (B) AFM micrographs before (left) and after (right) a 17 hour conjugation with 100 nM T4 Lysozyme. (C) AFM micrographs before (left) and after (right) a 16.5 hour conjugation with 250 nM T4 Lysozyme. (Samples (A) AKC48-FL 32ef, (B) AKC53-KG 11fh, and (C) AKC53-AD 12fg)

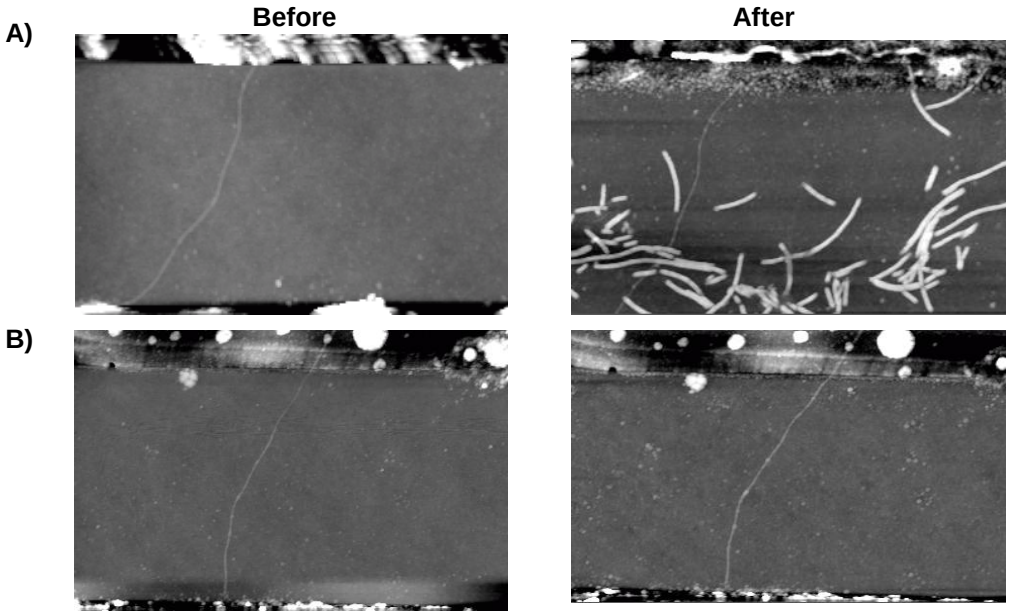


Figure 3.13: Time-dependent variability of protein solutions. (A) AFM micrographs before (left) and after (right) a 60 minute conjugation with 50 nM of T4 Lysozyme show the formation and deposition of fibrils on the oxide surface. (B) AFM micrographs before (left) and after (right) a 120 minute conjugation with 50 nM T4 Lysozyme with a recently prepared solution showing no aggregation or fibril formation. (Samples (A) AKC48-DM 32ab and (B) AKC48-DM 00ef)

3.7 Summary

The procedure for the conjugation of proteins to the sidewall of the nanotube is a complicated and still ill-understood process. The measurements presented here suggest that at high concentrations of protein the pyrene maleimide groups could be inaccessible due to the formation of mono- or multilayers of protein on the surface. They suggest that Tween-20 is most effective at preventing the non-specific binding of protein when included in the incubation step. They also examined the effect of minimizing the effects of contamination. Even with these issues accounted for, the conjugation yield is still low which suggests that pyrene maleimide

molecules are absent or inactive. An absence could be understood due to the low-solubility of pyrene maleimide in ethanol or that they have reacted to form a different compound. If they are indeed conjugated on the nanotube, the inactivity could be understood by competitive reactions that may occur with the reducing agent TCEP which is present at a concentration that exceeds the protein in the protein conjugation solution in order minimize disulfide formation. Because of this TCEP may also compete with the cysteine residues of the protein in reacting with available maleimide groups.

In order to continue this work, it would be useful to investigate the effect of pyrene maleimide solubility on the conjugation process since this or competing reactions may be the first bottleneck in the process. This could be done using solvents such as acetylnitrile, DMSO, or isopropanol. To test for competitive reactions, it may be necessary to eliminate TCEP from the protocol or to examine the conjugation with a different pyrene linker that can conjugate to amine groups. This may give some insight into the density of the pyrene on the SWNT as well as give additional information on how well the maleimide chemistry is performing. Once solubility is accounted for, then it should be possible to investigate systematically how the yield varies under different conditions and treatments in order to pinpoint other bottlenecks in the process. If these solvents lead to a substantial improvement in the conjugation procedure it may be necessary to devise a new windowing process that is compatible with the new solvent.

Chapter 4

Single-Molecule Signal Transduction in SWCNT FETs

Here, we investigate the hypothesis that signal transduction is driven by a simpler, electrostatic mechanism in which conformational motion of the lysozyme molecule electrostatically gates a short portion of the SWNT channel. Protein engineering was used to dissect the through-space interaction between eight different lysozyme variants and SWNT FET devices. The results prove the critical roles of two charged, side chain functionalities located close to the SWNT. Since all proteins have charged amino acids present on their surfaces, this transduction mechanism is straightforward to expand to a wide range of bioelectronic measurements.

4.1 Debye Screening in Single-Molecule SWNT FETs

One method of probing the interaction between lysozyme's enzymatic activity and the SWNT electrical signal I_{sd}(t) created by it is to vary the screening length of the surrounding electrolyte. I_{sd}(t) from the S90C lysozyme variant was measured in phosphate buffer (10 mM, pH 7.5) with a variable level of NaCl from 10 to 300 mM (Figure 4.1 (A)) to examine the role of the

electrolyte's ionic strength in screening electrostatic effects[39,45,67]. The magnitude of single-molecule fluctuations $|\Delta I_{sd}(t)|$ of the S90C lysozyme variant-containing devices peaked at a salt concentration of 50 mM and dropped sharply with increasing salt concentration.

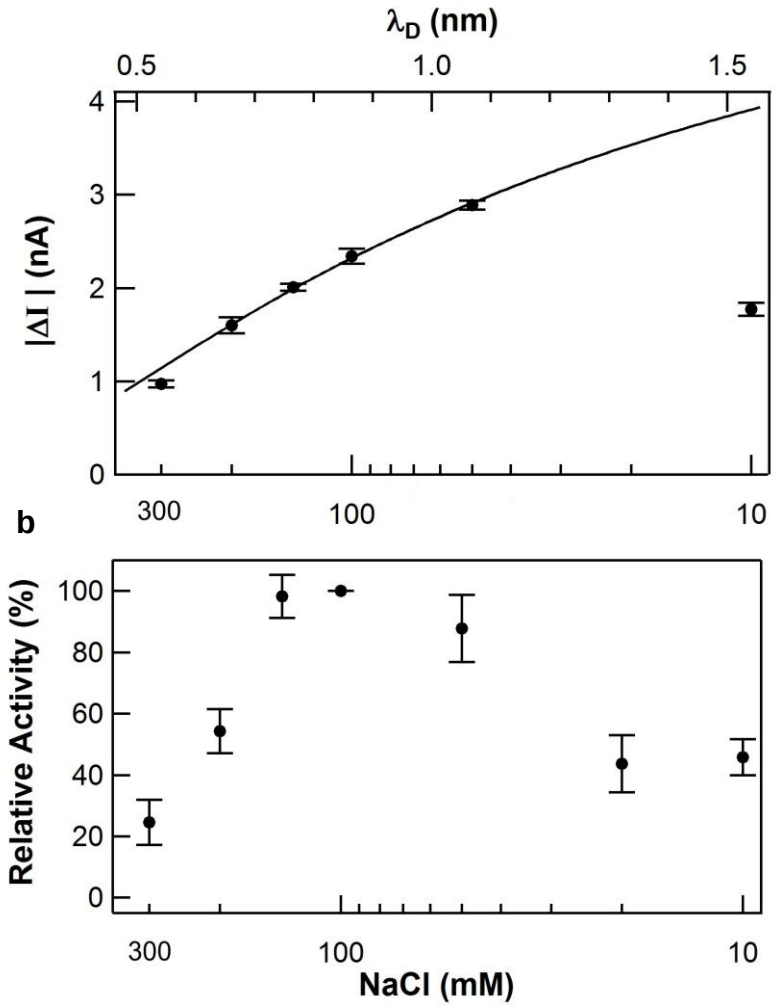


Figure 4.1: Debye screening of signal transduction. (A) The signal amplitude ΔI of a typical lysozyme SWNT FET as a function of the buffer salt concentration (bottom axis) and corresponding Debye length λ_D (top axis). The solid line is a fit to the Debye–Hückel screening model described in the text. Note that the phosphate buffer includes an additional 10 mM sodium phosphate. (B) Ensemble measurements of lysozyme activity over the same concentration range show varying enzymatic activity. The drop in activity and thus signal transduction at the lowest salt concentrations is likely due to enzyme denaturation. All error bars depict $\pm 1\sigma$. Reproduced from [53].

As the magnitude of ΔI decreased, the frequency distribution of the I_{sd}(t) fluctuations was substantially unchanged. An independent, fluorescence-based ensemble assay verified enzymatic activity over the tested range of salt concentrations (Figure 4.1 (B)). The ensemble measurements suggested a concentration dependence, which was not observed in single-molecule recordings. This disagreement is likely due to the combination of a broad, biexponential distribution of events and the relatively poor sampling of the full range of lysozyme's dynamic disorder (even a 600 s recording observes fewer than 10^4 catalytic events). Presumably, infinite-duration single-molecule measurements would reproduce ensemble rates. Thus, our investigation of signal transduction focused exclusively on the ΔI magnitude, which varied reproducibly and systematically between recordings as short as 10 s.

Except for measurement in 10 mM NaCl, the magnitude of ΔI fluctuations from the S90C variant of lysozyme can be described by the Debye–Hückel expression[68]

$$|\Delta I(t)| = \frac{A}{x_0} e^{-\frac{x_0}{\lambda_d}} \qquad (4.1)$$

where λ_D is the electrolyte Debye length[69] and x_o is the relevant screening distance for gating the SWNT FET. λ_D varies from 0.54 to 1.54 nm over the range of NaCl concentrations used here, and it is plotted on the top axis of Figure 4.1 (A). Even though the experimental range of λ_D was narrow, the data fit Equation 4.1 very well, and fitting determines the value $x_o = 1.03 \pm 0.10$ nm. The fit implicates an electrostatic mechanism rather than a purely mechanical (e.g., strain-based) one. Experiments by other laboratories have drawn similar conclusions[39,45,67]; for example, Stern et al. have used linker molecules of differing lengths to show that the parameter x_o accurately describes the distance between point charges and a sensitive, nanowire FET.

The small x_o value is remarkable given that a lysozyme molecule has physical dimensions of 5–7 nm. The active site for peptidoglycan catalysis is located 3.1 nm from the C90 attachment site, a distance of $3x_o$. Thus, the small x_o value suggests that the SWNT is responding to charge motions close to the C90 attachment site, rather than from events occurring exclusively at the active site, such as substrate binding. As predicted by theoretical modeling[70,71], single-molecule events at the enzyme's active site should be very difficult to detect electronically under these screening conditions. More likely, large-scale, substrate-induced conformational motions alter the positions of amino acids near the SWNT C90 attachment site.

This conclusion is further supported by two observations. First, multilevel I_{sd}(t) signals were observed when devices were fabricated using an alternate attachment site (Figure 4.2). Although both variants exhibited similar catalytic activities, the second attachment

site (S36C instead of S90C) reproducibly generated more complex, multilevel I_{sd}(t) signals. Second, the magnitude of the ΔI_{sd}(t) signal did not distinguish between catalytic processing and nonproductive binding of substrate[11,46], indicating that sensitivity is to mechanical motions of the enzyme rather than substrate binding and hydrolysis. Thus, we conclude that the ΔI_{sd}(t) electronic signal is generated by the enzyme's mechanical conformational motions near the attachment site and not its catalytic activity.

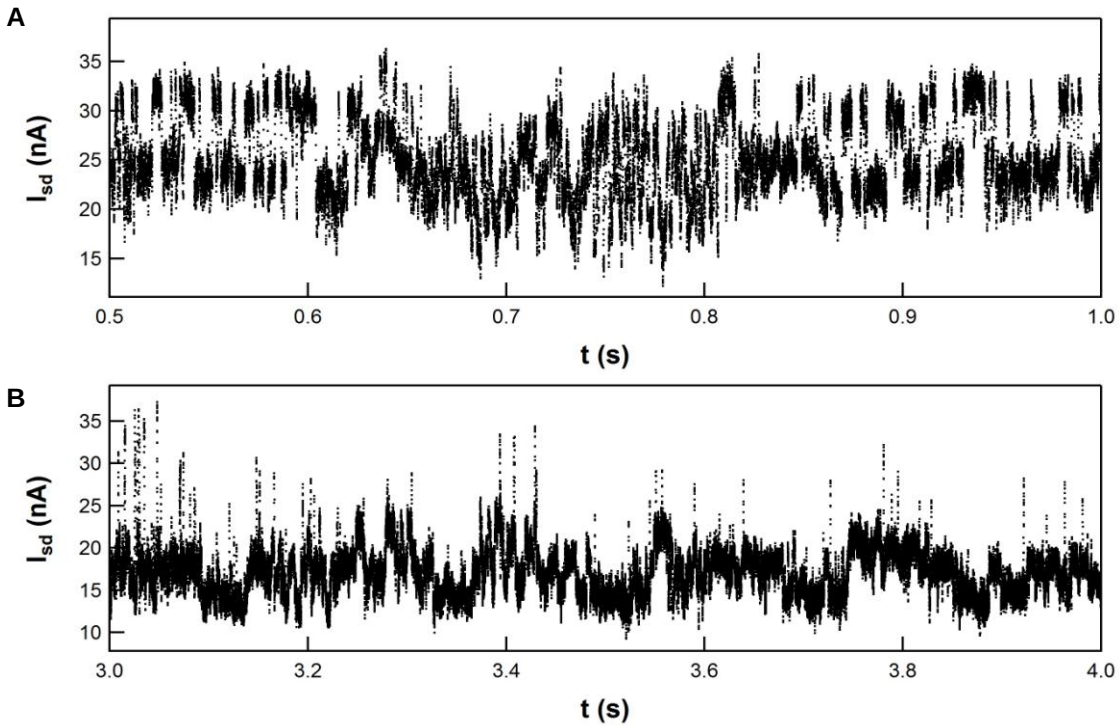


Figure 4.2: Examples of single molecule measurements with the S36C variant, in which simple two-level switching is accompanied by higher-frequency fluctuations (A) and/or multi-level switching (B). Reproduced from [53].

These results highlight the importance of the enzyme attachment site in lysozyme-functionalized SWNT FETs. The simple, two-level I_{sd}(t) signal of the S90C variant of lysozyme provided an ideal system for more detailed investigations. Comparisons of the X-ray crystal structures of lysozyme in the open (unbound) and closed (substrate bound)

states[72,73] reveal many charged residues within ~x_o of the C90 attachment site. Two of these, K83 and R119, are approximately 1.5 nm from the C90 attachment site and are particularly interesting as their charged side chain functionalities move substantially when the enzyme transitions from an open to a closed state (Figure 4.3). As the enzyme moves from an unbound to a substrate-bound state, positively charged K83 and R119 move further from the SWNT by approximately 0.15 nm each[57,72]. Unlike other surface charges, which remain relatively fixed in place, net movements of K83 and R119 could potentially affect the SWNT FET electrostatically. Consequently, we decided to directly measure the electrostatic contribution of each side chain functionality.

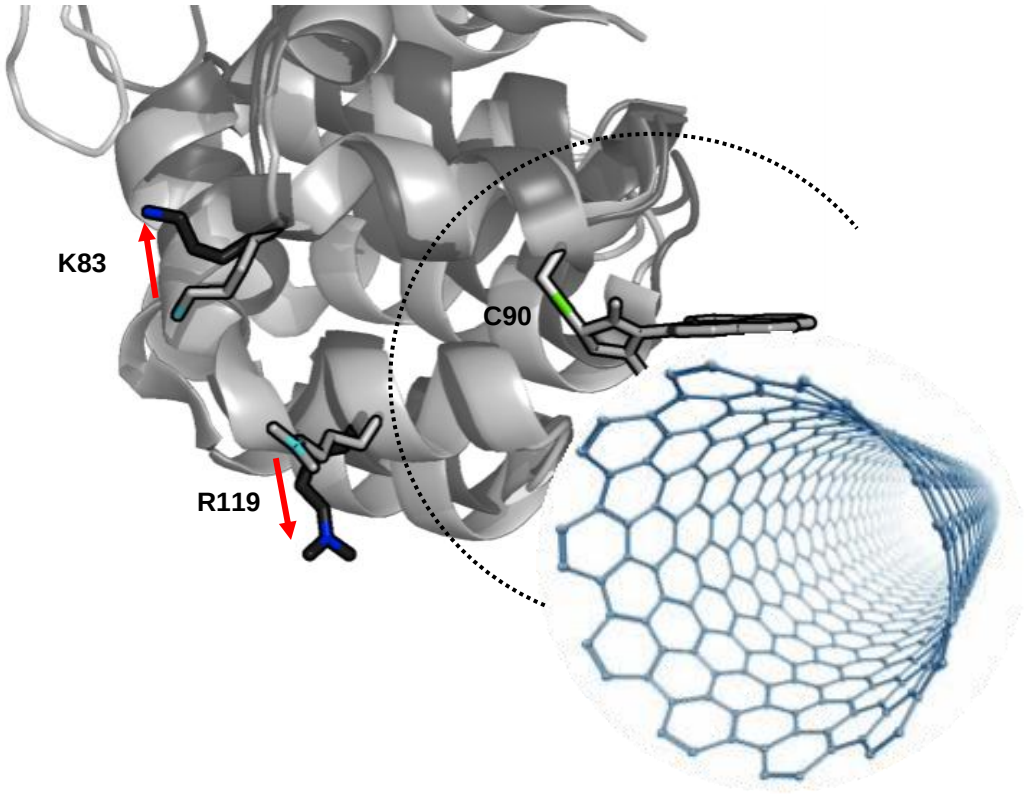


Figure 4.3: Detailed view of the lysozyme-SWNT interface, showing X-ray structures of a small portion of the protein in its open (light gray) and closed (dark gray) conformations (Protein Data Base 1QTV and 148L, respectively). The C90 attachment to the pyrene-maleimide linker molecule can provide a fixed reference point, and the dashed line depicts the distance x_o = 1.0 nm described in the text. In the vicinity of C90, only the amino acids at positions 83 and 119 have charged side chains that move appreciably (highlighted). The pyrene and SWNT are independently free to rotate around the C90 site, but this illustration depicts an energetically likely orientation. Reproduced from [53].

4.2 Electrostatic Effects of Specific Amino Acids

Site-specific engineering of proteins offers a powerful tool to probe the relationship between protein structure and function[74]. In this work, mutagenesis allowed the role of specific amino acids at the SWNT-lysozyme interface to be dissected. Seven variants of the S90C lysozyme were designed and synthesized; for each variant, the wild-type K83 and R119 residues were substituted with either neutral alanines, negatively charged glutamate residues, or a combination of the two amino acids. In the remainder of this report, the variants are frequently described in terms of a charge N, which here is defined as the sum of the bare elementary charges for only the two residues of interest, independent of the rest of the protein, electrolyte, or counterions. The variants were designed to have the net charge at positions 83 and 119 spanning from $N = +2$ to -2, with the initial S90C lysozyme variant accounting for the highest, $N = +2$ value.

To demonstrate the role of charged functionalities in signal transduction, Figure 4.4 shows representative signals from two of these SWNT FET devices. In the presence of substrate, both devices exhibited two-level switching with overall statistics that match our previous results. The main difference between the two examples in Figure 4.4 is a change in sign of the short-duration, transient events that correspond to the closed, substrate-bound conformation. The R119A variant has a single positive charge ($N = +1$) and produces positive $I_{sd}(t)$ fluctuations above a baseline current (Figure 4.4 (A)). The K83A/R119E variant has a single negative charge ($N = -1$), and produces $I_{sd}(t)$ fluctuations with the opposite sign (Figure 4.4 (B)).

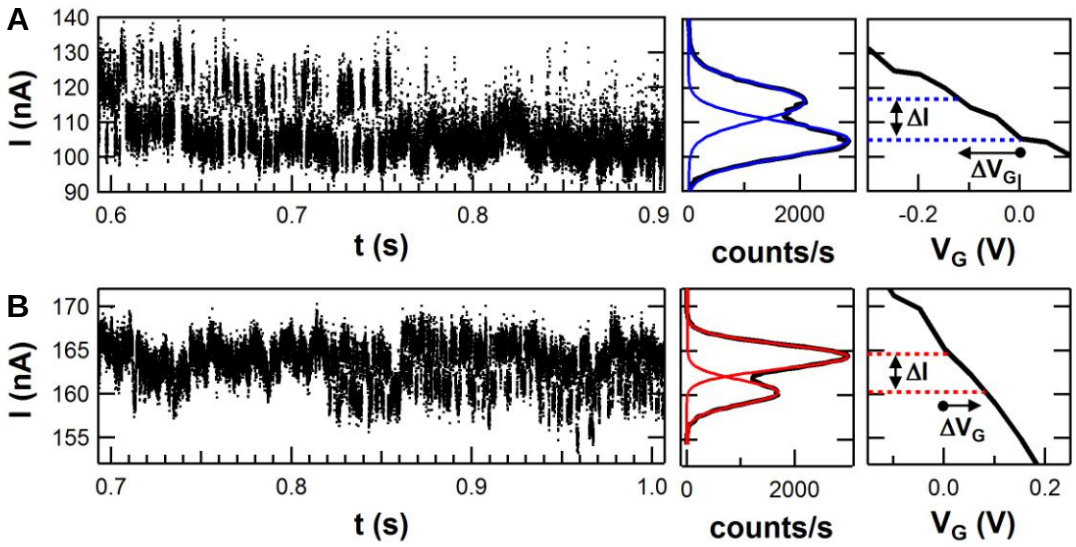


Figure 4.4: Dynamic I_{sd}(t) signals during catalytic processing and inactive, substrate-free moments. (A) A positively charged variant (R119A, N = +1) produces short duration I_{sd}(t) increases each time lysozyme closes upon the substrate. (B) A negatively charged variant (K83A/R119E, N = −1) produces I_{sd}(t) decreases, with the opposite sign but otherwise similar timing and statistics. Next to each segment of raw data, a histogram is shown for one full second of filtered signal. Each histogram is fit to two Gaussians, the peaks of which determine a transduction magnitude ΔI for the device. The unique electrolyte gating response $I(V_G)$ of each device (right) can be used to convert the closing action of the lysozyme enzyme into an effective change of gating ΔV_G from the operating point at V_G = 0 V. Reproduced from [53].

The left portions of Figure 4.4 show 0.3 s of raw I_{sd}(t) data from each, particularly selected to show a transition between active substrate-bound and the inactive, substrate-free conformation (Figure 4.4 (A, B)). Because the inactive enzymatic periods do not exhibit two level fluctuations, these transitional moments unambiguously identify the direction of the I_{sd}(t) signal upon hinge closure and therefore confirm a difference in sign for ΔI_{sd}(t) produced by the two variants. The middle portions of Figure 4.4 show histograms from longer, 1 s data sets obtained by first applying a 10-Hz, highpass filter to

each I_{sd}(t) signal. Both histograms are composed of a dominant peak for the hinge-open conformation and a smaller peak for the hinge-closed conformation, again revealing the difference in ΔI_{sd}(t).

Multiple electrical parameters were measured for each device. Two parameters that proved important for comparisons among devices were the size of two level fluctuations ΔI_{sd}(t) and the device's intrinsic sensitivity to electrolytic gating $I(V_G)$. Other than ΔI_{sd}(t) and $I(V_G)$, most other electrical characterization proved inconsequential to lysozyme transduction. In particular, we observed no dependence on device-to-device variation in resistance, or to the precise characterization of each SWNT as semiconducting or metallic. Device resistances varied widely from 0.2 to 20 megohms, a typical range for SWNT FET research that is associated with the contact resistance to individual SWNTs[75-78]. Because all of the measurements were performed with a fixed bias voltage of 100 mV, this resistance variation caused some devices to have mean currents $<I_{sd}(t)>$ of up to 500 nA while others carried as little as 5 nA. The magnitude of lysozyme-driven, two-level fluctuations increased proportionally to this mean value $<I_{sd}(t)>$.

Since each SWNT had a unique resistance and gate sensitivity, the mean value $<I_{sd}(t)>$ was completely independent of the lysozyme attachment. Nevertheless, we developed a robust and illuminating way of comparing the lysozyme component of ΔI_{sd}(t) from dissimilar devices. First, every lysozyme-functionalized SWNT was electrolytically gated in a substrate-free buffer to record its baseline response to gate voltages $I(V_G)$. The

relevant portion of $I(V_G)$ is the mean transconductance, or slope $\Delta I/\Delta V_G$, in the vicinity of the V_G = 0 V operating point, as depicted graphically in Figure 4.4 (right). Second, I_{sd}(t) histograms like those shown in Figure 4.4 were fit to two Gaussian peaks, the positions and widths of which depended solely on the SWNT properties. Third, the separation ΔI in peak position was converted to an effective change in gate voltage ΔV_G, as determined by each SWNT's $I(V_G)$ curve. The quotient of the separation ΔI divided by the transconductance $\Delta I/\Delta V_G$ is lysozyme's effective gating ΔV_G for any particular device. This step accounted for the fact that some SWNT FETs were semiconducting and very sensitive to electrostatic gating, while others were semimetallic and much less so. The conversion from ΔI to ΔV_G removed all of the device-specific differences to produce device-independent ΔV_G values. In past work, this process for calculating ΔV_G was applied to the S90C lysozyme variant, and a consistent ΔV_G value of -0.19 ± 0.02 V was obtained, even when measured across 18 different SWNT devices varying from semiconducting to metallic[11]. Thus, the ΔV_G should serve as a good variable to compare signal transduction by different lysozyme variants.

This normalization process is depicted graphically for the R119A (N = +1) and K83A/R119E (N = −1) lysozyme variants (Figure 4.4, right). The Gaussian fits are overlaid on each I_{sd}(t) histogram in color, and the peak positions are extended by dashed lines onto the $I(V_G)$ curves shown immediately to their right. The dominant peak of the R119A (N = +1) lysozyme variant at 105 nA corresponds to a device operating point around the applied gate bias of V_G = 0 V. The smaller peak at 117 nA shows that enzyme closure provides an effective change in gate of $\Delta V_G = -119 \pm 52$ mV (Figure 4.4 (A),

right). The operating point for the K83A/R119E ($N = -1$) lysozyme variant at 165 nA was shifted to a lower current by an effective gating $\Delta V_G = +77 \pm 23$ mV (Figure 4.4 (B), right). In both cases, the error in ΔV_G is estimated from the width of the Gaussian fits. As demonstrated by Figure 3.4, this width is primarily due to the large background noise typical of SWNT devices[79-81] and biosensors[45,82]. Thus, the error does not necessarily indicate variations in the dynamic disorder or signal transduction by the enzyme.

Figure 4.5 summarizes the individual responses from each of 30 different SWNT devices tested, color coded according to the particular variant of lysozyme attached. This scatter plot shows the fluctuation magnitude $\Delta I(t)$ and the transconductance $\Delta I/\Delta V_G$ of each device, normalized by $\langle I(t) \rangle$. Normalization had no effect on the computed value of ΔV_G from any individual device. On normalized axes, all of the data from samples with one particular variant lie on the straight line corresponding to a singular ΔV_G value. This representation proved useful for guiding ongoing experimentation. It became clear that more precise values of ΔV_G could be obtained from line fits in Figure 4.5 if the devices covered a wide range of $\Delta I/\Delta V_G$. Initial efforts fabricating many devices with a particular variant (e.g. S90C) were replaced by a more methodical effort to select devices spanning a wide range of $\Delta I/\Delta V_G$. (e.g. K83A/R119A and K83E/R119A). Using this technique, comparably small ΔV_G error bars were achieved for each variant using as few as three or four devices in some cases.

The ΔV_G from 30 different SWNT FETs, incorporating one of the seven charged lysozyme variants revealed the role of charged functionalities in signal transduction (Figure 4.6). The ΔV_G of each charged variant proved to be characteristic and ranged from −205 to +135 mV. The positive variants had $\Delta V_G < 0$ V, whereas the negative variants had $\Delta V_G > 0$ V. The two variants with $N = \pm 2$ exhibited the strongest signals, being approximately twice as large as from $N = \pm 1$ variants. Furthermore, a single charged functionality could effectively transduce signal from enzyme to SWNT with a large ΔV_G value.

Direct, quantitative comparisons of each lysozyme variant's ability to transduce signal were generated by plotting ΔV_G as a function of N. The observation of two-level switching by the neutral, K83A/R119A lysozyme variant ($N = 0$) identifies the likely contributions of all other charged residues at positions near residues 83 and 119. The observed gating of $\Delta V_G = -34$ mV in the neutral case agrees with previous calculations[71] based on the distal domain's net charge of +3 and its substantial hinge motion relative to C90. Figure 4.6 (B) shows the effective gating ΔV_G of each variant, with (open squares) and without (solid squares) this contribution. After adjustment, the entire set of values became nearly symmetric about zero and linear to N for all six charged variants. The average slope $d\Delta V_G/dN = -91$ mV per unit charge is a sensitivity nearly three times greater than from the rest of the protein combined. A more detailed consideration of signal transduction by these two positions follows.

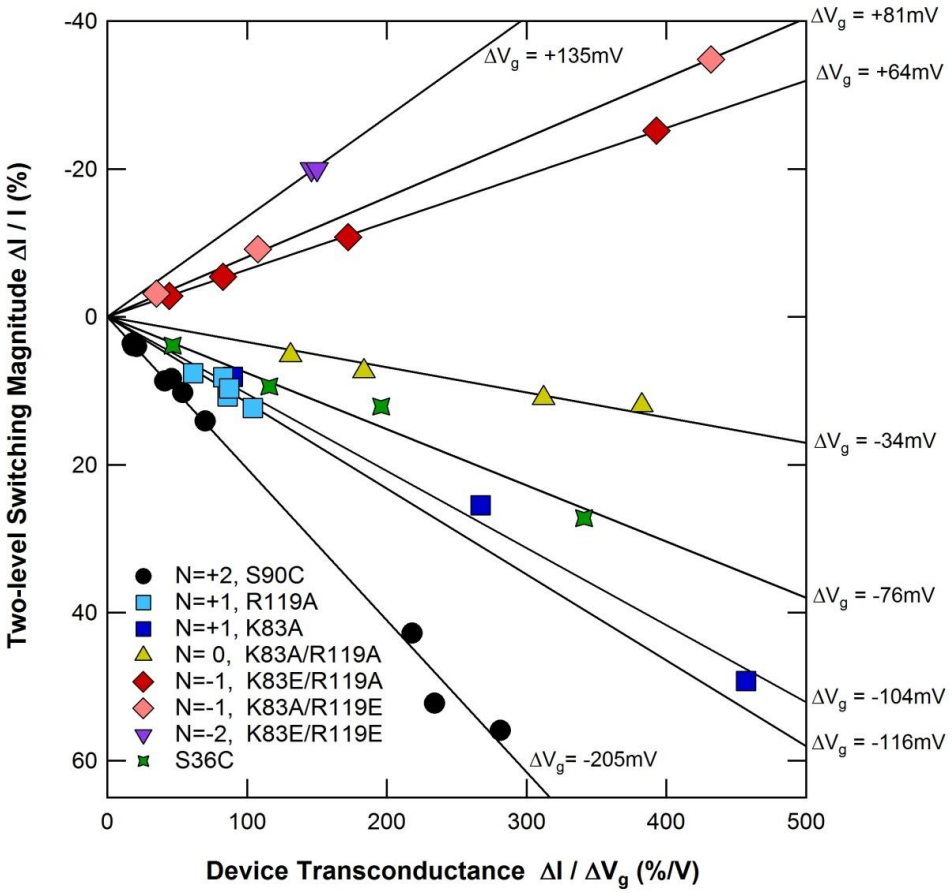


Figure 4.5: Compilation of switching amplitudes for all seven S90C variants and the S36C variant. Each data point represents one SWNT device functionalized with one of the possible lysozyme variants. Reproduced from [53].

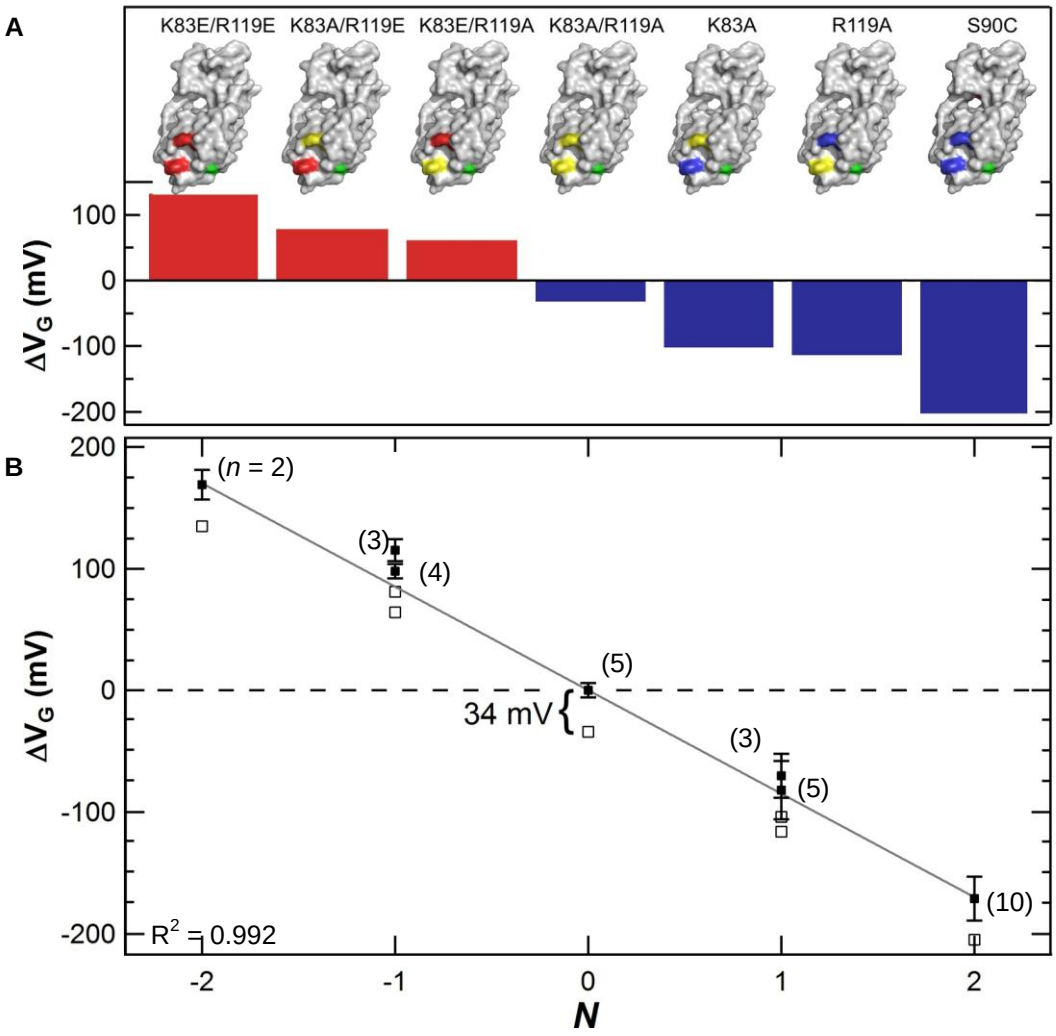


Figure 4.6: Average transduction by seven charged variants. (A) Lysozyme positions 83 and 119 were mutated to have positive (blue), neutral (yellow), or negative (red) charged side chains. The effective gating ΔV_G by each variant varied from 135 to −205 mV, with a value of −34 mV for the neutral $N = 0$ variant. (B) For all variants, ΔV_G is nearly proportional to N, with a slope of −85 ± 2 mV per unit charge. Raw data (open squares) shifted up +34 mV (solid squares) results in a response symmetric around zero. Error bars indicate three standard deviations as determined from n (indicated in parentheses) different devices fabricated with each particular variant. Reproduced from [53].

4.3 Electrostatic Mechanism

Taken together, results from Debye screening and site-directed mutagenesis demonstrate an electrostatic mechanism in which charged functionalities at S90C lysozyme positions 83 and 119 play a dominant role in signal transduction by gating the SWNT FET. Unique to these positions are key factors that, we believe, predict good quality signals. First, these positions have charged side chains that move substantially as a result of catalytic processing. Second, these residues are much closer to the SWNT than other, similarly charged residues, making them less shielded than distant charges. The Debye screening experiments also suggest that salt concentration can be optimized within a biologically relevant range to maximize the signal from these two positions. For example, decreasing the salt concentration improves the signal-to-noise ratio, until low salt concentration prevents the enzyme from functioning normally.

To analyze the electrostatic mechanism further, we have calculated the theoretical electric fields created by charges at lysozyme positions 83 and 119 (Table 4.1). Comparisons of the X-ray structures of lysozyme in its open and closed configurations provided the vector movement of each charge relative to C90 and to the attached pyrene-maleimide linker. The principal qualitative feature of the calculations is that both residues move away from the attachment site as lysozyme binds its substrate. Thus, the net electric field during closure becomes less positive in the $N = +2$ case. In the $N = -2$ case, the field

becomes more positive. For both variants, the sign of the change agrees with the ΔV_G observed experimentally.

Since the orientations of both lysozyme and the SWNT with respect to the pyrene-maleimide linker are not easily defined, there is uncertainty in the electric fields at the SWNT sidewall. Nevertheless, we have modeled an energetically likely orientation of the lysozyme with respect to pyrene-maleimide and the SWNT (Figure 4.3). In this model, the dihedral angle of pyrene with respect to maleimide is fixed at its lowest energy conformation at an angle of −50°. This consideration restricted the orientation of lysozyme with respect to the SWNT to two possible lowest energy thioether rotamers[74]. One cysteine rotamer maintains the 83 and 119 residues at similar distances from the SWNT, resulting in nearly equal electrostatic effects from movements at either position. The second rotamer would cause a charged residue at 119 to have three to five times the gating effect as one at position 83, which is an asymmetric effect that has not been observed for any device to date. The data in Figure 4.6 show both positions to have nearly equal gating effects on the SWNT, leading us to depict the first rotamer in Figure 4.3.

Table 4.1: Electric field magnitudes generated by point charges of interest. Reproduced from [53].

	K83E/R 119E	**K83A/ R119E**	**K83E/R 119A**	**K83A/ R119A**	**K83A**	**R119A**	**S90C**
N	-2	-1	-1	0	+1	+1	+2
Q_{83}	-1	0	-1	0	0	+1	+1
$r_{83,\ open}$ (nm)*	2.33		2.33			2.33	2.33
$r_{83,\ closed}$ (nm)*	2.51		2.51			2.51	2.51
$\Delta\lvert r_{83}\rvert$ (nm)*	0.18		0.18			0.18	0.18
Q_{119}	-1	-1	0	0	+1	0	+1
$r_{119,\ open}$ (nm)*	1.90	1.90			1.90		1.90
$r_{119,\ closed}$ (nm)*	1.98	1.98			1.98		1.98
$\Delta\lvert r_{119}\rvert$ (nm)*	0.09	0.09			0.09		0.09
E_{open} (V/μm)	-26.9	-18.4	-8.9		18.4	8.9	26.9
E_{closed} (V/μm)	-22.0	-16.5	-6.6		16.5	6.6	22.0
ΔE (V/μm)	4.9	1.9	2.2	0.0	-1.9	-2.2	-4.9
ΔV_G (mV) (expt.)	135	81	64	-34	-104	-116	-205
ΔV_G+ 34 mV	169	115	98	0	-70	-82	-171

*measured relative to the center of pyrene-maleimide.

The calculated fields predict that positions 83 and 119 should be somewhat distinguishable, as expected for any two charges located at slightly different positions. In fact, the main experimental difference between the two positions in Figure 4.6 is not a difference in sensitivity $d\Delta V_G/dN$, such as would arise from differing distances, but rather a reproducible offset that is systematically higher than the $\Delta V_G = -34$ mV value of the neutral variant. Specifically, the two $N = \pm 1$ variants with charge at position 119 result in a fit to the expression $\Delta V_G = (-92N - 11 \pm 8)$ mV, whereas charges at position 83 give $\Delta V_G = (-90N - 26 \pm 6)$ mV. The charge-symmetric response from both positions has a

nearly identical slope $d\Delta V_G/dN$, but with position-dependent offsets that are up to 2σ more positive than from the neutral variant.

The offset described above indicates that assigning a single, fixed ΔV_G to all the nontargeted charges in the enzyme is too simplistic. Structural differences among the variants are expected to be minor, as the variants remain functional and fold consistently into similar circular dichroism-measured structures. Furthermore, protein structure typically remains indifferent to the substitution of small numbers of surface-exposed residues, as shown for many proteins; for example, T4 lysozyme has been mutated at position 119 without affecting its thermal stability[83]. An alternative and more attractive interpretation reconsiders the complexity of the charge substitutions themselves. The side chain functional groups are not true point charges, but rather charge distributions resulting from different chemical functionalities in a complex, screening environment. Pursuing this hypothesis, we observe that small shifts of $\Delta N = -0.1$ and -0.2 at the positions 83 and 119, respectively, can align the data to a single, constant offset $\Delta V_G = -34$ mV. A more detailed analysis requires precise knowledge of the linker's orientation, the SWNT's response to the resultant fields, and a more accurate model of electrolyte screening in the immediate vicinity of the linker, all of which are formidable characterization challenges.

Another detail apparent in Table 4.1 but not in Figure 4.6 is the joint effect of the $N = \pm 2$ variants. Placing charges at both positions 83 and 119 approximately doubles the effective gating and suggests an additive effect. In fact, ΔV_G is not quite twice as large as

measured when $N = \pm 1$, rather being greater by only a factor of 1.87. Experimentally, $d\Delta V_G/dN = -85$ mV per unit charge, whereas the sum of the individual charges would predict $d\Delta V_G/dN = -91$ mV. An inspection of Figure 4.3 reveals the cause: the two side chains do not move in parallel to each other; thus, the vector sum of their fields must be less than the sum of the two magnitudes. The vector calculation in Table 4.1 accounts for this geometry.

4.4 Summary

Finally, we conclude with a short summary of factors that impact the effectiveness of these devices, since understanding their operation at the molecular level could generalize the approach to other single-enzyme experiments. Remarkably, the role of the particular SWNT is quite minimal, as both metallic and semiconducting SWNTs produce comparable signal-to-noise ratios. This ratio is not substantially improved by seeking the steeper $I(V_G)$ curves of semiconducting SWNTs, since their enhanced sensitivity is accompanied by greater noise from background fluctuations. These observations prove that transduction and sensitivity of the lysozyme-functionalized SWNT FETs is not merely due to carrier accumulation or depletion, as in more traditional semiconductor-based sensors. Instead, we note that the electrostatic $I(V_G)$ response in the functionalized devices is different from that of pristine SWNTs. In practice, the DC resistance of every SWNT FET is raised by the biofunctionalization[11], with the added scattering located at the point of attachment. Thus, sensitivity is not controlled by electrostatic doping nor by selecting a SWNT with a particular bandstructure; rather, it results from a local scattering

barrier induced by the attachment itself. This colocalization of the chemical sensitivity and electrical transduction, which has been studied in detail for covalent SWNT defects[42,80-82], leads to signal amplification. We hypothesize that the enzyme's motion modulates the height and/or width of this barrier, leading to an electostatic field effect that is distinct from carrier accumulation. Additional theoretical work in this area would be very beneficial, since past attempts to model SWNT sensitivity have pursued more traditional bandstructure or charge transfer models.

In addition to the proximity of charged functionalities to the enzyme attachment site described above, the location of this site within the overall protein structure is also critical to successful transduction. First, the attachment site does not need to be located near the enzyme's active site. In fact, attachments at such positions might interfere with activity and could perturb enzymatic function. Second, we have selected an attachment site that is relatively rigid with respect to the molecule's center of mass. C90 moves by less than 0.15 nm during catalytic processing. We suspect that similar positions of minimal motion could be key aspects of good attachment sites, since they can minimize perturbations to the enzymatic activity and mechanical stresses on the SWNT linkage. Third, the presence of one or more charged groups moving in concert near the attachment site is critically enabling. The measurements here prove that the immediate environment of the attachment site is most important for transduction.

In conclusion, these results support a very simple, electrostatic gating mechanism for signal transduction by single enzymes in SWNT FETs. By varying the surrounding

electrolyte and the enzyme's surface charges, we have built a precise understanding of signal generation in these devices. The data show that mechanical displacements of charged functionalities resulting from distal motions are the primary sources of transduction. Furthermore, through selection or introduction of such functionalities, the signal strength can be optimized. The findings suggest design rules by which structural data can guide the creation of similarly effective nanocircuits for single-molecule studies of other enzymes, binding proteins, aptamers, and ribozymes. In addition, single-mutation sensitivity has been demonstrated, providing a promising platform for the further study of molecular function with single-molecule resolution.

Additional work is required to understand if this approach can be used to tailor the signal of other enzymes such as Protein Kinase A or DNA Polymerase. It may be possible to introduce a highly-charged and mobile region to an enzyme in order to enhance the signal to noise even further or to choose an attachment site such that binding of a charged substrate would give a substantial signal. Also since an enzyme can be made to have charged regions within a Debye length of the SWNT, it may be possible modulate the potential of the SWNT via the electrolytic gate at frequencies that could drive motions of the enzyme through electrostatic attraction and repulsion. By doing so, it may be possible to control the rate of catalysis of an enzyme.

Chapter 5

Single-Molecule Measurements of cAMP-Dependent Protein Kinase (PKA)

Recently, we demonstrated a new electronic method for monitoring and deciphering enzymatic processing and kinetics with single molecule resolution.[11,46,53] Single molecules of T4 lysozyme were non-covalently bioconjugated to single-walled carbon nanotube (SWNT) electronic devices. The motions by the lysozyme active site during chemical catalysis move charged functionalities close to the SWNT to convert conformational changes of the protein into an electronic signal.[53] Analysis of long-duration records from single molecules established lysozyme as a processive enzyme, with multiple independent timescales governing its productive and non-productive motions.[11]

Here, we apply this electronic monitoring technique to examine the catalytic subunit of cAMP-dependent protein kinase (PKA). Electronic transduction clearly resolves each

step in the formation of the active, ternary complex. The results allow independent measurements of multiple kinetic parameters involved in PKA catalysis.

5.1 cAMP-dependent Protein Kinase (PKA)

The enzyme PKA regulates cell function by phosphorylating a wide-range of proteins involved in cell signaling, transcription, and metabolism.[84-87] The phosphoryl transfer reaction catalyzed by PKA mechanism requires the enzyme to simultaneously bind adenosine triphosphate (ATP) and a phosphate acceptor peptide or protein. In the presence of Mg^{2+}, this ternary complex transfers the gamma phosphate group from ATP to the hydroxyl group of a serine or threonine residue on the substrate.[84,85,88,89] A key player in cell function and cell division, PKA also offers an archetypical protein for the study of kinase regulation and function. Furthermore, single molecule studies of PKA could address such outstanding issues as the basis for its regulated activity, the breadth of its dynamic range, and the full spectrum of kinetic parameters forming the basis of its activity.

In order to examine PKA and its kinetics, individual molecules were attached to SWNT transistors using methods similar to past work.[11,46,53] First, a surface-exposed, cysteine residue was introduced into a PKA variant by oligonucleotide-directed mutagenesis encoding the T32C substitution to provide a thiol functionality for site-specific attachment to SWNT devices. A number of different sites to attach PKA to the SWNT through cysteine thiol reaction with pyrene-maleimide were explored, but the

T32C variant of PKA emerged as the mutant protein with the best overexpression levels. At the end of the A-helix, yet near the conserved start of the kinase core, the T32C bioconjugation site falls between regions of secondary structure. This design aimed to limit the impact of the cysteine modification on protein stability. After PKA over-expression and purification, the enzyme was incubated with SWNT transistors that had been noncovalently functionalized with pyrene-maleimide linker molecules. The maleimide functionality of the linker formed stable thioether bonds with the target thiol functionality on a PKA molecule. During functionalization, a solution of ATP and $MgCl_2$ (2 mM each) was used to sterically block another, naturally-occurring cysteine sidechain in PKA.[56] Figure 5.1 (A) depicts the geometry of a SWNT device and its PKA attachment based on the position of the T32C site, and Figure 5.1 (B) shows an atomic force microscopy image of an actual device after protein bioconjugation. Charged residues in motion near to T32 during enzyme opening and closing could allow SWNT device response to conformational changes during enzymatic catalysis (Figure 5.1 (C)).

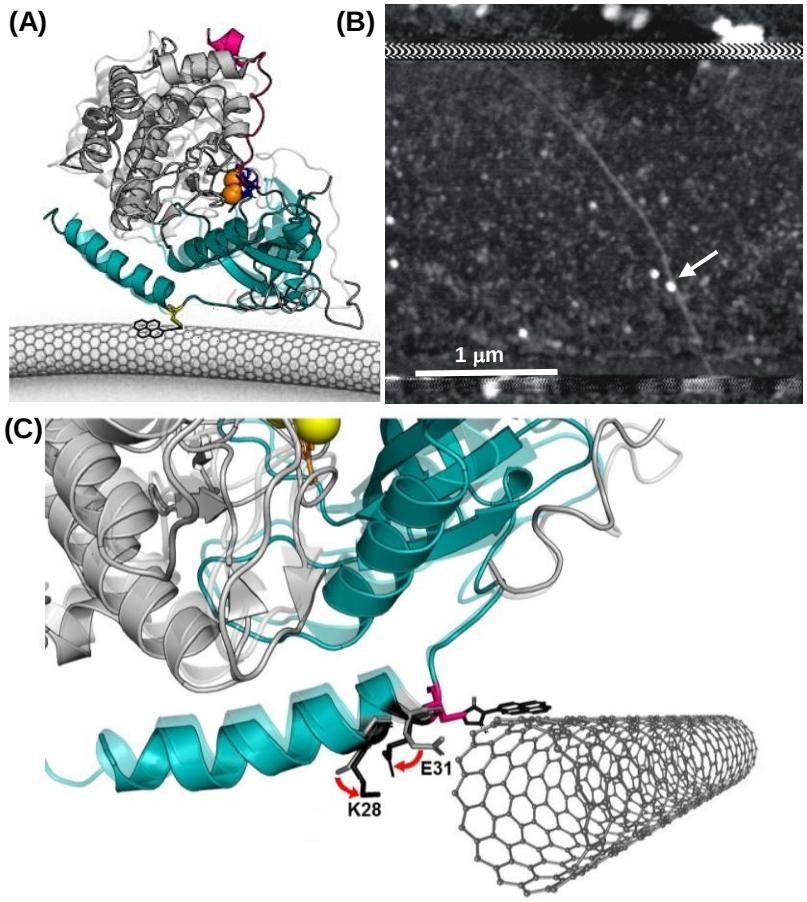


Figure 5.1: PKA-labeled, SWNT-based nanocircuits for single molecule electronic monitoring (A) Schematic of a single core catalytic subunit of PKA (small lobe in cyan and large lobe in gray) attached to an SWNT-based circuit through a single cysteine (yellow). Two magnesium ions (orange) position ATP (blue) in the binding pocket. As PKA catalyzes the transfer of γ-phosphate from ATP to its substrate, Kemptide (magenta), the protein undergoes a conformational change from the open (opaque, PDB: 1J3H) [90] to the closed (transparent, PDB: 1ATP) [91] state. (B) Example atomic force micrograph of a SWNT device with a single protein attachment (arrow). Horizontal stripes at top and bottom show the extent of a passivating polymer that covers the distant source and drain electrode connections. (C) Schematic diagram of the PKA-SWNT interface, showing close-up X-ray crystal structures of PKA in its closed(opaque) and open (transparent) conformations (PDB: 1ATP and 1J3H, respectively). The C32 attachment to the pyrene-maleimide linker molecule provides a fixed reference point. In the vicinity of C32, residues 28 and 31 have charged side chains that move appreciably from the open configuration (light gray) to the closed conformation (black). The pyrene and SWNT are independently free to rotate around the C32 site, but this illustration depicts an energetically likely orientation. Reproduced from [12].

After bioconjugation, devices were stored and then measured in a buffered aqueous solution (100 mM MOPs, 9 mM $MgCl_2$, 100 μM TCEP, pH 7.2). Measurements were performed by applying a fixed, 100 mV source-drain bias along the SWNT conductor while continuously monitoring the source-drain current $I_{sd}(t)$. The attached PKA then interacted with its co-factor ATP or its peptidic substrate Kemptide[88] added singly or as mixtures to the electrolyte. $I_{sd}(t)$ recordings extended continuously for at least 300 s in each experiment; this $I_{sd}(t)$ measurement was digitized at 100 kHz and stored for subsequent analysis. To assist stability during long duration measurements, the electrolyte potential was controlled at -300 mV relative to the drain electrode using a Pt pseudo-reference electrode.

5.2 Control Measurements

Control measurements were conducted using a device from the same chip that had a successful protein attachment. The control and functionalized devices simultaneously underwent the protein attachment protocol, but the control device failed to yield an attachment. This device was then electrically measured in the buffered aqueous solution (pH 7.2), buffered aqueous solution (2 mM ATP), buffered aqueous solution (100 μM Kemptide), and buffered aqueous solution (2 mM ATP, 100 μM Kemptide). As shown in Figure 5.2, no processive fluctuations from the baseline were observed.

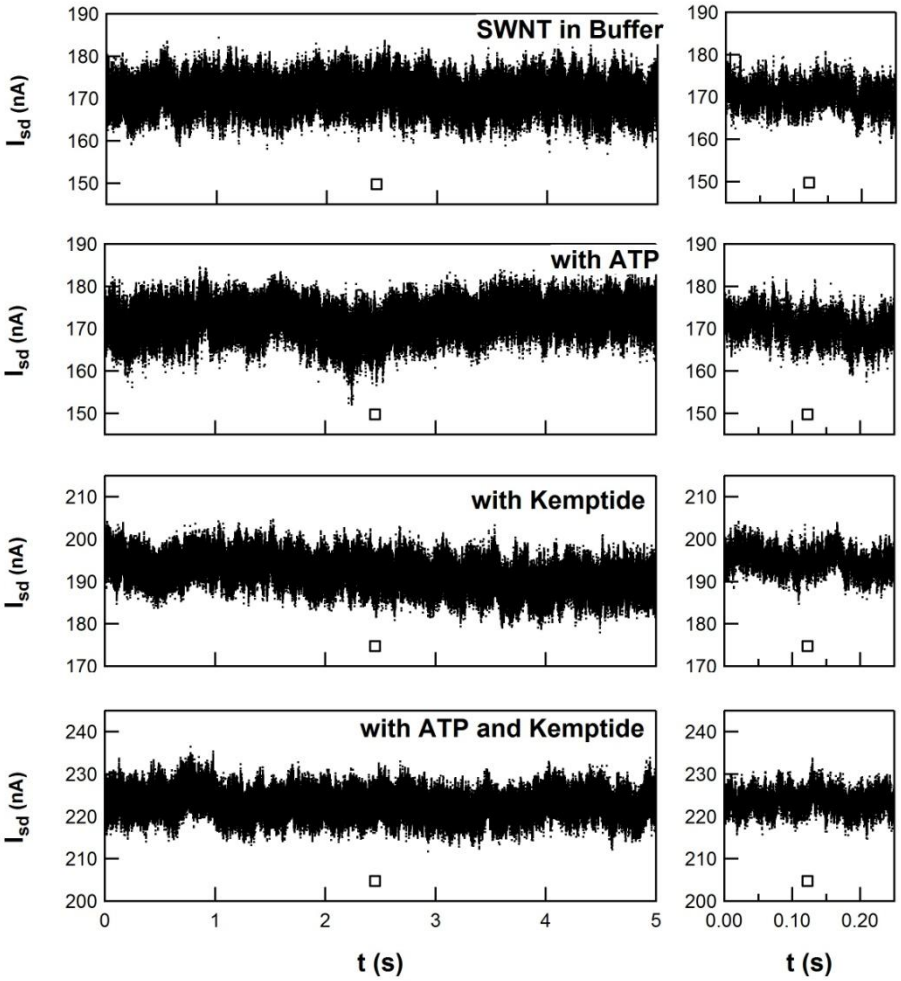


Figure 5.2: Control measurements of a pyrene-maleimide coated SWNT device, with no attached PKA. In the presence of ATP and/or Kemptide, I_{sd}(t) through the device shows no fluctuations except for the characteristic pink noise found in all SWNT electronic devices. Reproduced from [12].

5.3 Electronic Measurements of PKA Binary Complexes

Figure 5.3 depicts typical I_{sd}(t) signals and signal distributions measured from a PKA-functionalized SWNT in various solutions. With PKA in buffer, I_{sd}(t) merely fluctuated about a mean baseline value (Figure 5.3 (A)) with a distribution determined by the 1/f

noise of the SWNT device. Following the addition of ATP or Kemptide to the PKA-conjugated nanocircuit, new, quasi-stable levels of I_{sd}(t) were observed below this baseline (Figures 5.3 (B-E)). Figure 5.3 (B) shows the results of measuring I_{sd}(t) while the PKA was incubated in a 2 mM concentration of ATP, yielding a 2:9 molar ratio of ATP:Mg^{2+}. In the presence of ATP, I_{sd}(t) exhibited transient excursions ΔI of approximately -8 nA, or nearly -19%. Qualitatively similar excursions were observed when PKA was measured in a 100 μM solution of Kemptide substrate (Figure 5.3(C)). This concentration was slightly below the K_D for the PKA-Kemptide complex (230 ± 70 μM),[92] which could decrease the apparent affinity for Kemptide measured here.

Differences in either amplitude or duration were investigated as possible metrics for distinguishing PKA-ATP excursions from PKA-Kemptide ones in mixtures of the two reagents. However, neither approach proved practical. The amplitude distributions of binding to either ATP or Kemptide almost completely overlapped, and the mean durations of each binding event concealed a wide, nonstationary distribution, which is discussed further below. Nevertheless, the mean duration of many thousands of excursions was distinguishably different in measurements made individually with either ATP or Kemptide, measuring 3.1 ms for ATP and only 1.8 ms for Kemptide. By also analyzing the waiting times between each excursion, we extracted rates for one cycle of binding and unbinding by each ligand of 125 s^{-1} and 286 s^{-1} for ATP and Kemptide, respectively. Thus, the enzyme cycles through binding and unbinding to Kemptide faster than to ATP. The results reported here confirm classic ensemble measurements showing PKA can bind independently to both Kemptide and ATP, but the exact order is largely random.[93,94]

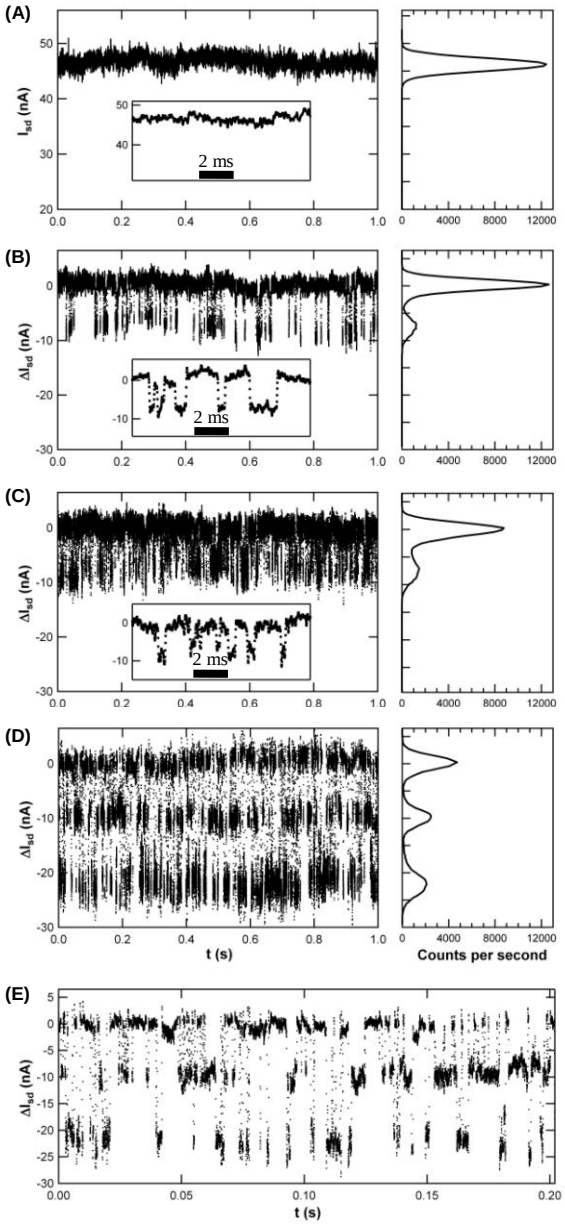


Figure 5.3: Representative ΔI_{sd} (t) signals and signal distribution histograms for a PKA-conjugated SWNT device. (A) Unfiltered, raw data as measured in buffer, showing the absolute value of I_{sd} (t). (B-E) ΔI_{sd} (t) relative to the baseline current, as measured in the presence of (B) 2 mM ATP, (C) 100 µM Kemptide, and (D,E) both ATP and Kemptide. The magnified view in the insets and (E) indicates the high level of detail discernible in individual transitions. In the discussion, the high, mid and low current states are assigned to the apo, the substrate- or ATP-bound (intermediate), and the catalytically functioning (fully closed) enzyme conformations, respectively. Reproduced from [12].

Table 5.1. PKA binding rates.[a]

	Single-Molecule						Ensemble
ATP	τ	±	σ	<t>	±	σ	<t>
bound (ms)	1.99	±	0.03	3.1	±	4.3	5.3[b]
unbound (ms)	0.77	±	0.01	5.0	±	19	> 0.25[c]
binding / unbinding cycle (s^{-1})	362	±	5[d]	125[e]			< 190[c,f]
Kemptide	τ	±	σ	<t>	±	σ	<t>
bound (ms)	0.77	±	0.01	1.8	±	2.9	<2[g]
unbound (ms)	0.67	±	0.01	1.7	±	3.7	<20[h]
binding / unbinding cycle (s^{-1})	696	±	8[d]	286[e]			>46

[a]Where τ is the characteristic time from an exponential fit to the data reported in Figure 5.4, and <t> is the arithmetic mean from the distribution shown in Figure 5.4.

[b][95]

[c]Estimated by extrapolation to saturation conditions from the experimental data of Ni et al.[95]

[d]$1/(\tau_{bound} + \tau_{unbound})$

[e]$1/(<t_{bound}> + <t_{unbound}>)$

[f]Estimated from ligand exchange with AMP-PNP

[g][96]

[h][97]

We interpret each transient excursion $\Delta I_{sd}(t)$ to result from one PKA binding event. Table 5.1 shows that this interpretation results in average waiting times and rates for a complete cycle of binding and unbinding that agree well with ensemble values. Negative control measurements further support this analysis by showing that in the absence of an attached PKA, pyrene-maleimide functionalized SWNTs (Figure 5.2) exhibit none of the low current excursions shown in Figure 5.3, which again are associated with ATP or Kemptide binding to PKA. Furthermore, $\Delta I_{sd}(t)$ fluctuations were reliably eliminated by rinsing ATP and/or Kemptide off the device, and were restarted by reintroducing a

binding partner. As an example of this, the data in Figure 5.3 is chronologically reversed: the baseline I_{sd}(t) in Figure 5.3 (A) was acquired *after* probing the device with ATP and Kemptide solutions; the results confirmed recovery of the baseline after testing.

The electrical signals can be well-explained by an electrostatic transduction mechanism previously demonstrated using SWNT devices and single T4 lysoyzme molecules.[53] Like the previous experiments with lysozyme, PKA has two charged residues in close proximity to the SWNT conjugation site (Figure 5.1 (C)). In the lysozyme example, the two proximal residues have positively charged sidechains that swing away from the SWNT during enzyme closing; for the hole-doped SWNTs of our experiments, such movement results in an increase in I(t).[53] The proximal sidechain functionalities of PKA also move in concert; a negatively charged functionality flips away and a positively charged residue moves towards the SWNT. The net effect from the combined electrical field of both charged residues is a large decrease in I_{sd}(t), providing excellent signal to noise levels for analysis.

In the absence of binding partners, the PKA apoenzyme adopts an open conformation in which the large lobe (residues 127 to 300) is 1.33 nm from the smaller lobe (residues 30 to 120, as measured with respect the α-carbon of S53 and G186.[90] This stable, open conformation produces the baseline current observed in Figure 5.3 (A). Upon binding to either ATP or Kemptide, PKA moves into an intermediate conformation, in which the two lobes are separated by 1.18 nm or 1.07 nm, respectively.[98,99] For either binding partner, the large lobe moves closer to the small one, which is attached to the SWNT

conductor. The motions of PKA described by NMR[97,100] agree well with the dynamics described here. For example, Veglia, Taylor and co-workers [97,100] reported that the enzyme transits through three conformational states during catalysis, analogous to the open (apo), intermediate and closed (ternary) states observed using the SWNT device.

5.4 Dynamic Disorder of PKA Binary Complex

Single molecule measurements offer powerful tools to reveal enzyme variability and dynamic disorder, which are typically hidden during ensemble measurements.[23,101-103] The timing of PKA binding to ATP and Kemptide measured here both exhibited the wide variability associated with the dynamic disorder of the enzyme. Figure 5.4 (A) shows the distribution of the duration for the enzyme bound state for both ligands individually added to PKA-functionalized nanocircuits; the distributions were constructed from continuous, 45-second subsets of I_{sd}(t) recordings. Figure 5.4 (B) shows analogous distributions for the waiting times between binding events (i.e., the unbound or open-enzyme state). The slopes of simple, single-exponential fits (solid lines in Figures 5.4 (A, B)) determine the fitted τ values that represent the majority (95%) of events and determine the most probable on- and off-rates of either ATP or Kemptide.[104] However, all four distributions also include long-duration tails that deviate significantly from a single exponential behavior. The waiting time for ATP binding, in particular, exhibits a much longer distribution tail. Furthermore, unlike the near-parity situation for Kemptide on- and off-rates, the PKA-ATP complex has a slower off- than on-rate.

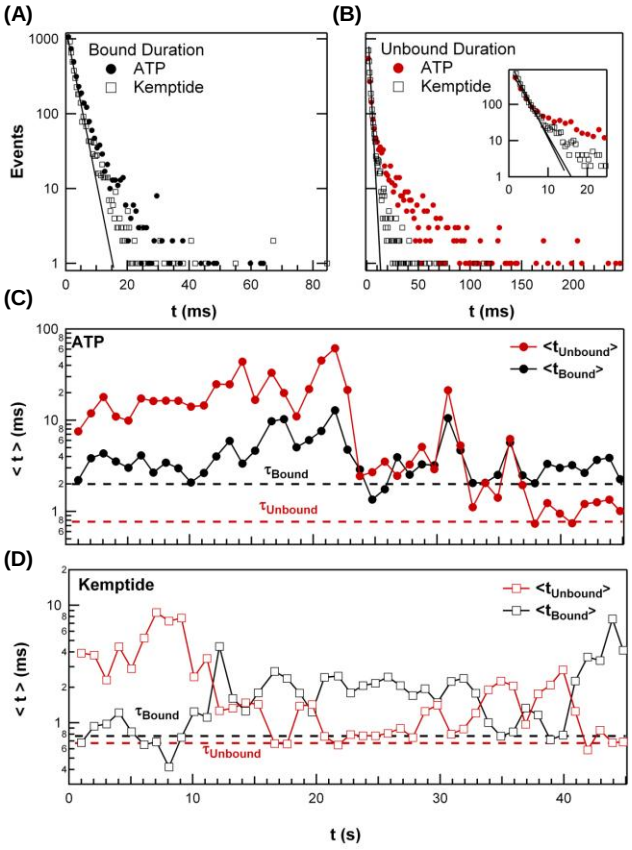


Figure 5.4: Dynamic disorder of PKA observed by single molecule measurements with either ATP or Kemptide. (A) Distributions of the duration of the enzyme bound conformation for ATP or Kemptide. (B) Distributions of the waiting times for ATP and Kemptide binding, with the shortest waiting times shown more clearly in the inset. In (A) and (B), single-exponential line fits determining τ are shown as solid lines. (C) Variation in the 1-second arithmetic mean values <t> of ATP binding kinetics. These values were calculated by averaging the indicated one second of data. The corresponding τ values from the exponential fit are indicated by dashed lines for comparison. (D) The analogous variation in Kemptide binding kinetics. Reproduced from [12].

The unusually long events in the distribution tails exert a disproportionate impact on the enzyme's activities. While most of the distribution has a mean duration τ, an arithmetic average of the entire distribution produces a longer average duration <t>. For Kemptide

binding, for example, <t> is more than 2τ. The long-duration events have similar effects on the statistical variances, σ^2. Because of these substantial differences, τ and <t> are tabulated independently in Table 5.1 with their corresponding standard deviations. The practical consequence of the longer <t> values is a reduction of the average ligand cycling rates by 59 to 66%. Even though the faster, maximum rate 1/τ is the probabilistically favored value from cycle to cycle, the reduced rate 1/<t> is the one accessible to ensemble measurements because it includes all excursions in the kinetics.

Consequently, one would not expect rates measured through ensemble techniques to agree with rates determined by molecular dynamics simulations or NMR spectroscopy. PKA is known to have a very dynamic structure with binding sites that allosterically couple with remote loops and subdomains.[97,100] Apparently, these interactions can result in a broad range of observable rate constants; such dynamic disorder is immediately evident to single molecule techniques.

Figures 5.4 (C, D) illustrate this dynamic disorder resulting in a temporal variation of PKA-ATP or PKA-Kemptide complex stability. These graphs plot the second-by-second variation in the average times for $<t_{bound}>$ and $<t_{unbound}>$, throughout the same 45-second intervals. During some seconds, very few long-duration events occur and <t> approaches τ. During others, <t> grows much longer. The rate-limiting waiting time for ATP binding extended over the widest range, varying over two orders of magnitude from one second to another (Figure 5.4(C)). Furthermore for the PKA-ATP complex, $<t_{unbound}>$ and $<t_{bound}>$ follow each other weakly, with a statistical correlation of r = 0.71 (Figure 5.5

(A)). A positive correlation suggests a common mechanism for both steps, such as a conformational change distant from the ATP binding site, that increases or decreases both $<t_{unbound}>$ and $<t_{bound}>$.

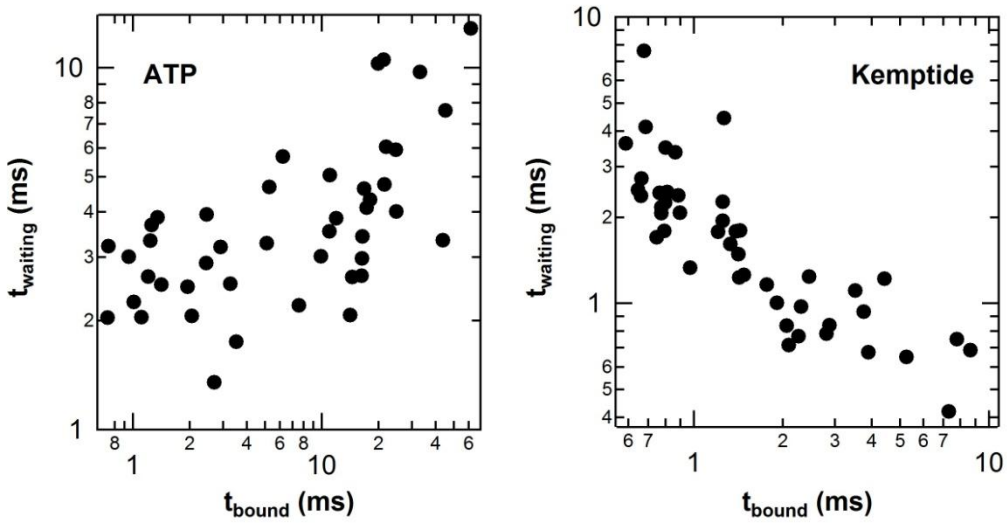


Figure 5.5: Scatter plot of $<t_{bound}>$ and $<t_{waiting}>$ using 1-second averages for ATP or Kemptide. (A) For ATP, $<t_{bound}>$ and $<t_{waiting}>$ are weakly correlated with r = 0.71. This positive correlation suggests a shared mechanism such as such as a conformational change distant from the ATP binding site which may modify the energy barrier between the bound and unbound states. (B) For Kemptide, $<t_{bound}>$ and $<t_{waiting}>$ are anti-correlated with r = -0.84. An anti-correlated behavior suggests that as PKA slowly undergoes slow viscoelastic motions the binding affinity for kemptide can either increase or decrease. Reproduced from [12].

Compared to ATP binding, PKA-Kemptide binding statistics show different trends (Figure 5.4 (D)). For Kemptide, the binding times $<t_{unbound}>$ and $<t_{bound}>$ were confined to a narrower range of 0.7 ms to 10 ms and tended to move in opposite directions. In fact, $\ln(<t_{unbound}>)$ and $\ln(<t_{bound}>)$ are anti-correlated with r = -0.84 (Figure 5.5 (B)). This strong, logarithmic anti-correlation is similar to the behavior of slow, viscoelastic motions.[105] Here, the binding and unbinding rates are affected by one or more

conformational motions, which increase the affinity of PKA for Kemptide, stabilizing the PKA-Kemptide complex and favoring its formation. Altering such conformational motions through binding by regulatory binding partners likely provides the basis for sensitive regulation of PKA activity, as such conformational changes will dramatically favor either the Kemptide bound or unbound states. Furthermore, ATP binding cannot provide a basis for regulated enzyme activity, as such conformational changes affect the stability of both bound and unbound PKA in a correlated manner.

Additionally, we note that $<t_{bound}>$ and $<t_{unbound}>$ varied widely enough to reverse their relative durations. Generally, the bound state of PKA interacting with either ATP or Kemptide was much shorter-lived than the unbound state; thus, the transduced $I_{sd}(t)$ signal looked like the pattern of excursions depicted in Figures 5.3 (B, C). Approximately 25% of the time, however, the bound and unbound lifetimes became comparable, and the resultant $I_{sd}(t)$ showed two-level switching with essentially symmetric timing. In rarer situations, the bound state became much longer than the unbound state. During these periods, the excursions in $I_{sd}(t)$ become positive spikes corresponding to a short-lived, apo PKA conformation. Examples of each case are shown for PKA binding to Kemptide in Figure 5.6. Fortunately, continuous single-molecule monitoring provided long-duration $I_{sd}(t)$ records in which the two states could be unambiguously identified throughout the experiment.

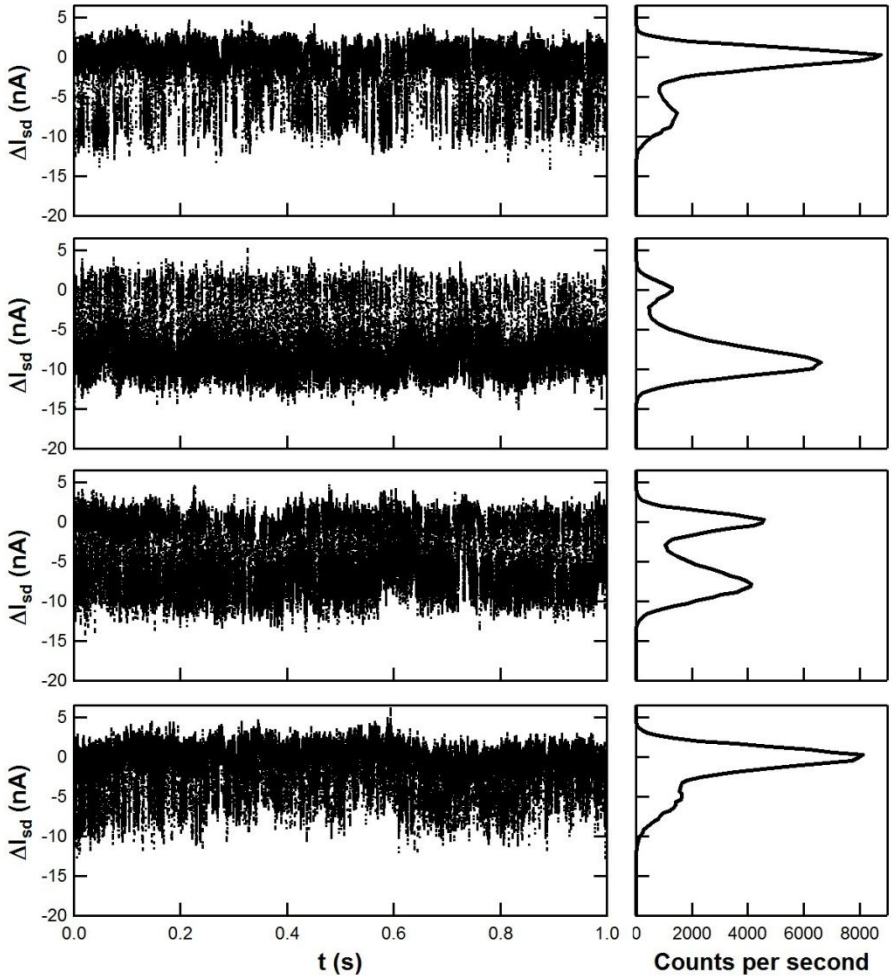


Figure 5.6: Conductance fluctuations of a single PKA device due to Kemptide binding and release. Over a ten minute measurement, $<t_{bound}>$ and $<t_{waiting}>$ varied dynamically such that $<t_{bound}>$ could be either larger or smaller than $<t_{waiting}>$. For one-second windows, the conductance histograms typify these dynamic, relative variations of $<t_{bound}>$ and $<t_{waiting}>$. Reproduced from [12].

5.5 Electronic Measurements of PKA Ternary Complex

The simultaneous binding of both ATP and Kemptide allows PKA to assume a fully closed conformation that completes formation of the catalytically functional, ternary complex. Once in this conformation, the enzyme can transfer the gamma phosphate of ATP to the Kemptide substrate.[85] Experimentally, the addition of both ATP and Kemptide to the PKA-conjugated SWNT produced three-level $I_{sd}(t)$ fluctuations shown in Figure 5.3 (D). The baseline and intermediate states are identical to those described above for single ligand binding events, and these intermediate states are joined by a new, quasi-stable current level that was 20 nA, or 42%, below the baseline current. This amplified signal is consistent with the fully closed enzyme conformation; such a conformation has been observed previously by NMR and X-ray crystallography.[91,97] In this conformation, the large lobe approaches even more closely to the SWNT conductor, thus altering the electronic signal even more than upon ATP or Kemptide binding. Figure 5.3 (E) shows a high resolution portion of just 0.2 s of data, and illustrates excellent separation of individual events for statistical analysis.

Figure 5.7 shows probability distributions and mean values for the durations of the apo, intermediate, and fully closed PKA conformations. The mean durations are 4.4, 1.1, and 2.6 ms for the apo, intermediate, and closed conformations, respectively. Such durations are naturally influenced by the concentrations of ATP and Kemptide present, which were 2 mM and 100 μM, respectively. For each conformation, we separately plot two distributions to account for the possibility that the duration of the conformation depends

on the previous state of the enzyme. For example, Figure 5.7 (A) shows the apoenzyme conformation. The entire distribution is stretched to longer durations when the open state follows the closed state instead of the intermediate one. A physical explanation of this increase could be that the preceding closed state has resulted in a successful catalytic event, after which product release slows the enzyme as it begins a new cycle; furthermore, the divergence between the distributions of the apoenzyme state resulting from either the ternary or the intermediate states is consistent with a different conformation required for catalysis, than for mere binding. The intermediate conformation (Figure 5.7 (B)) has a much smaller, but still significant dependence on the previous conformational state. Transitions through the intermediate conformation are 30% longer, on average, when they follow the closed rather than the open conformation. The duration of the ternary complex has essentially no such dependence. All six probability distributions are stretched exponentials, indicating varying kinetics and possibly a variety of hidden states to which $I_{sd}(t)$ may not be sensitive; for example, a slow step might follow the intermediate step before product release.

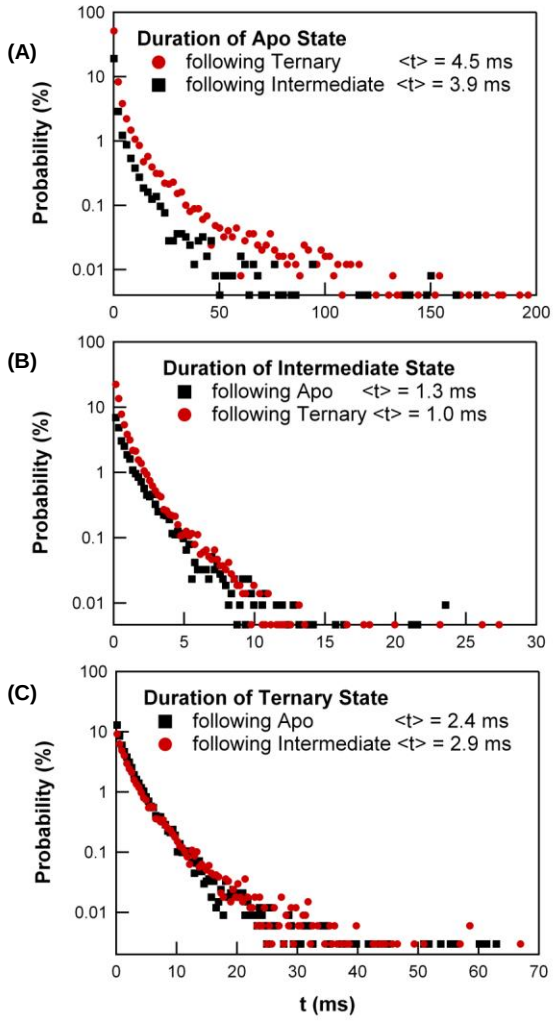


Figure 5.7: Probability distributions of the duration spent in each of the following three PKA conformations: (A) the unbound apo state, (B) the intermediate state with one binding partner, and (C) the ternary, fully closed state. For each state, two distributions are shown to distinguish the direction of conformational change. Only the apo state in (A) has a significant dependence on its previous conformational state. Reproduced from [12].

5.6 Transition Probablities of PKA

The high quality signal shown in Figure 5.3 (E) allow determination of a wide variety of statistics, and Table 5.2 shows mean durations of the final state and the transition

probability matrix amongst each of the possible conformations. Beginning in the open conformation, transitions directly to the ternary complex were observed 73% of the time, while transitions to the intermediate state only occurred in the remaining 27%. Of course, every formation of the ternary complex must occur via the intermediate bound state; however, the binding of Kemptide and ATP are known to be highly cooperative[97], and therefore occur nearly simultaneously on the time scale of the electronic measurements. The measurements here were performed with 20 μs time resolution, during which diffusion-limited transport and near-simultaneous binding could very well have occurred in too few data points to be resolvable.

Table 5.2. Matrix of transition probabilities and mean durations.

	Final State					
	Low		Middle		High	
Initial State	P	<t>	P	<t>	P	<t>
Low			45%	1.0 ms	55%	4.5 ms
Middle	71%	2.9 ms			29%	3.9 ms
High	73%	2.5 ms	27%	1.3 ms		

Complex transition probabilities between more than just two conformations are interesting to complete the portrait of PKA activity. For example, the mean time from the beginning of one closure to the next via the intermediate configuration determines the effective catalytic turnover rate, assuming successful phosphorylation takes place each time the enzyme accesses the fully closed conformation and then returns to the apo state. In a single data set, we observed 20,000 such events and were able to determine a mean turnover rate of 107 s^{-1}.

5.7 The Efficiency of Phosphorylation by PKA

As with the other rates described above, however, the mean value concealed the true variability of the processes observed. The mean turnover rate for 10 s intervals ranged broadly from 13 to 230 s^{-1}, which overlaps with the ensemble-measured value of 21 s^{-1}.[89] The vast majority (77%) of turnovers occurred via a straightforward sequence of open-intermediate-closed-open conformations and with a rate of 155 s^{-1}. A minority (13%) of turnovers visited the closed state twice before opening, leading to a slower rate of 91 s^{-1}. And finally, the remaining 10% of turnovers cycled multiple times between the closed and intermediate conformations before finally opening with product release with a turnover rate of 37 s^{-1}. We interpret these sequences as failed attempts to phosphorylate the Kemptide, which remained bound while PKA repeatedly closed upon it. Thus, we determine PKA to have a 77% probability of success during the first closure and only a ~50% probability of catalysis during each subsequent attempt (Figure 5.8). This relatively low probability leads to occasional sequences of enzyme motion in which 10 or

more closures are observed before substrate release (Figure 5.8, inset). A minimal kinetic scheme consistent with this data is shown in Figure 5.9. Furthermore, if the enzyme fails to catalyze the phosphorylation reaction each time it cycles between fully closed and the apo state, the turnover rates and efficiency could be even lower; the reported rates represent an upper bound on the catalytic efficiency of PKA.

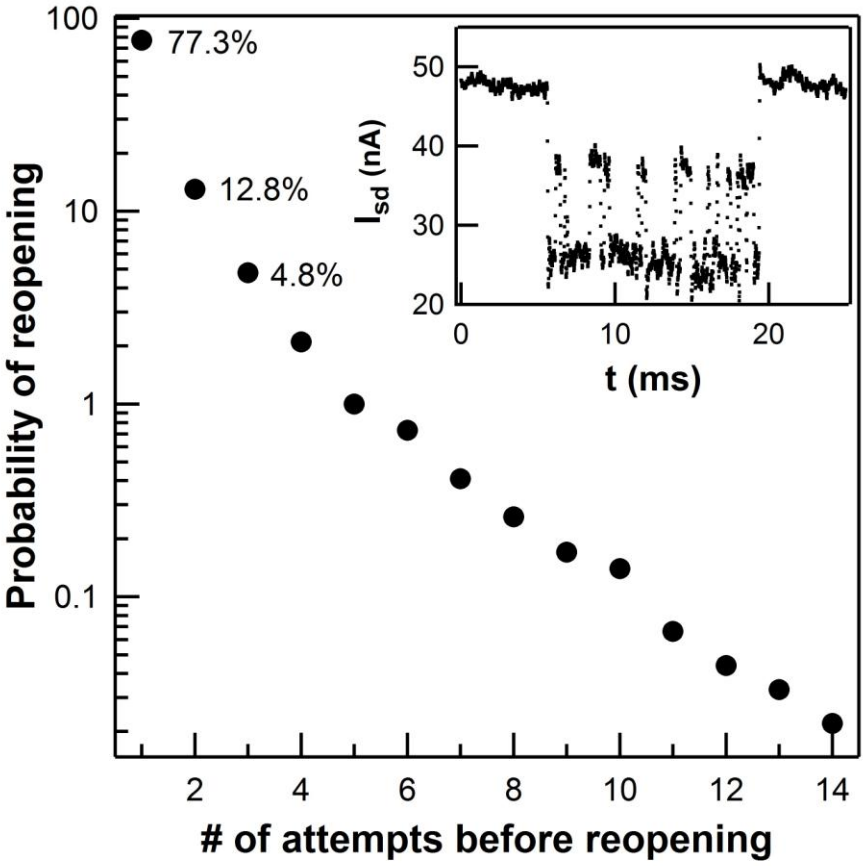


Figure 5.8: Probability of re-opening, as indicated by the return to the apo conformation. Inset: I_{sd}(t) trace shows an example of multiple transitions between the intermediate and closed conformations before finally re-opening. Reproduced from [12].

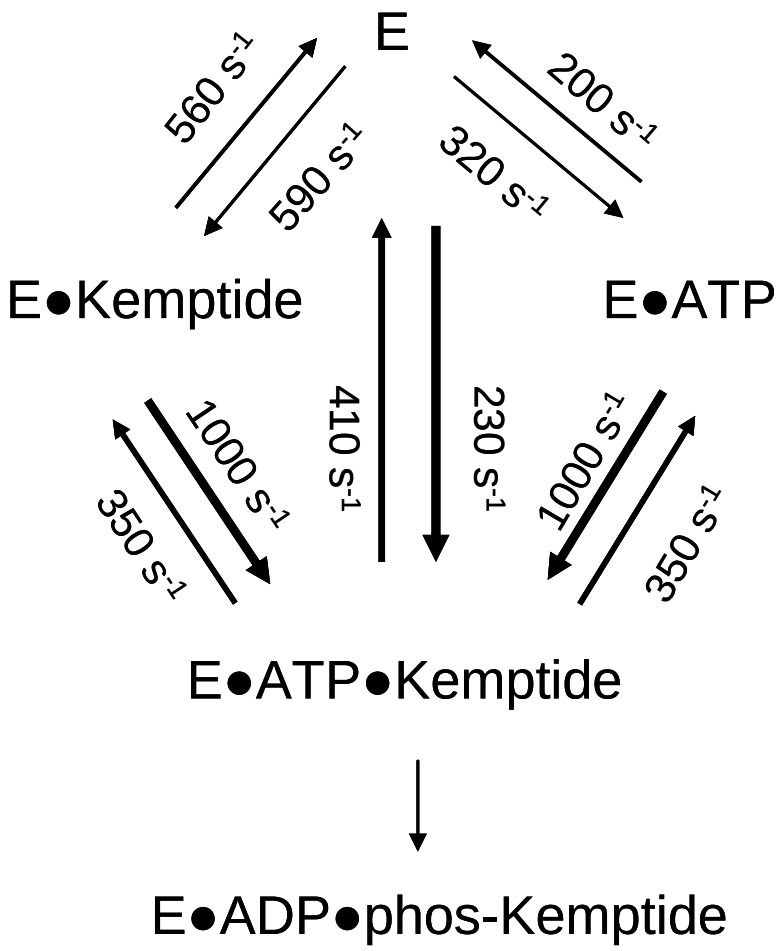


Figure 5.9: A kinetic scheme for the PKA-catalyzed phosphorylation of Kemptide with rates measured by a single PKA functionalized SWNT device. The thickness of the lines reflects the transition probabilities from Table 5.2 with thicker lines indicating a higher probability. Reproduced from [12].

In the perfect enzyme described by Knowles, every substrate binding event results in catalysis.[106] The conformational vicissitudes described above undermine the catalytic efficiency of PKA. Each failure to access the fully closed configuration necessary state for catalysis wastes an opportunity for substrate-to-product conversion. In comparison, the enzyme hexokinase catalyzes a similar phosphoryl transfer reaction to a primary hydroxyl functionality, yet exhibits far higher catalytic efficiency (2×10^9 $M^{-1}s^{-1}$ for hexokinase vs. 5-6 x 10^6 $M^{-1}s^{-1}$ for PKA).[107,108] The efficiency of hexokinase is consistent with its role as catalyst for a key step in metabolism. PKA's vacillation from the intermediate configuration reflects the evolution of signaling kinases like PKA to provide a regulatable molecular switch, rather than evolution to optimize catalytic efficiency.

5.8 Fluctuation and Noise Measurements

A final notable aspect of the I_{sd}(t) signals in Figure 5.3 is a difference in the widths of their distributions. Individual peaks in the I_{sd}(t) histograms were fit to Gaussian functions to quantitatively compare these widths. The baseline current centered around $\Delta I_{sd} = 0$ had the narrowest distribution σ_o = 1.03± 0.06 nA, and we found this width to be independent of whether binding partners were present (e.g., Figure 5.3 (B, C or D) or not (Figure 5.3 (A)). The smaller, secondary peaks associated with PKA binding to ATP or Kemptide both had widths of approximately $1.5\sigma_o$. The distribution of the ternary complex had the lowest mean value but the largest width of nearly $2\sigma_o$. This trend is opposite to the behavior of the SWNT's 1/f noise, which normally decreases

proportionally to the mean current. Thus, the increased width of ΔI_{sd} is most likely associated with the attached PKA and the motions of its surface charges, which are more stochastic upon ligand binding. In other words, the enzyme accesses a broader range of conformational motions during formation of the ternary complex from the intermediate conformation.

The fluctuation magnitudes ΔI_{sd} shown in the y-axis of Figure 5.3 are sensitive to both the contact resistance and transconductance of a particular SWNT device. Both of these parameters vary from device to device. Thus, to aid direct comparisons within this report, all of the data in Figures 5.3-5.7 were collected from a single device. Similar fluctuations have been observed over shorter durations using other PKA-labeled SWNT devices, and past work has proven that fluctuation magnitudes ΔI_{sd} can be converted into an effective molecular "gating" (ΔV_G) that eliminates device-to-device variability; we have successfully applied this approach to eliminate this variability in >100 devices with different enzymes attached.[53] The effective ΔV_G relates ΔI_{sd} to the transconductance of the device and is a measure of the change in electrolyte gate that would reproduce the observed signal.

For the T32C variant of PKA described here, the transition from the open or apoenzyme to the intermediate state produces a ΔI_{sd} that is equivalent to a change in electrolyte gate ΔV_G of +87 ± 7 mV for ATP and +65 ± 11 mV for Kemptide. The transition from the open apoenzyme to the fully closed, ternary complex is equivalent to ΔV_G = 221 ± 20 mV, an effect that is much greater than the sum of ATP and Kemptide binding. All of the

stated error bars are one standard deviation calculated from relatively limited data sets (Figure 5.10), and they may reduce significantly once data is available from a wider range of SWNT devices. In the meantime, these mean ΔV_G values allow the data to be compared to theoretical models and predict how similar PKA-SWNT devices should behave.

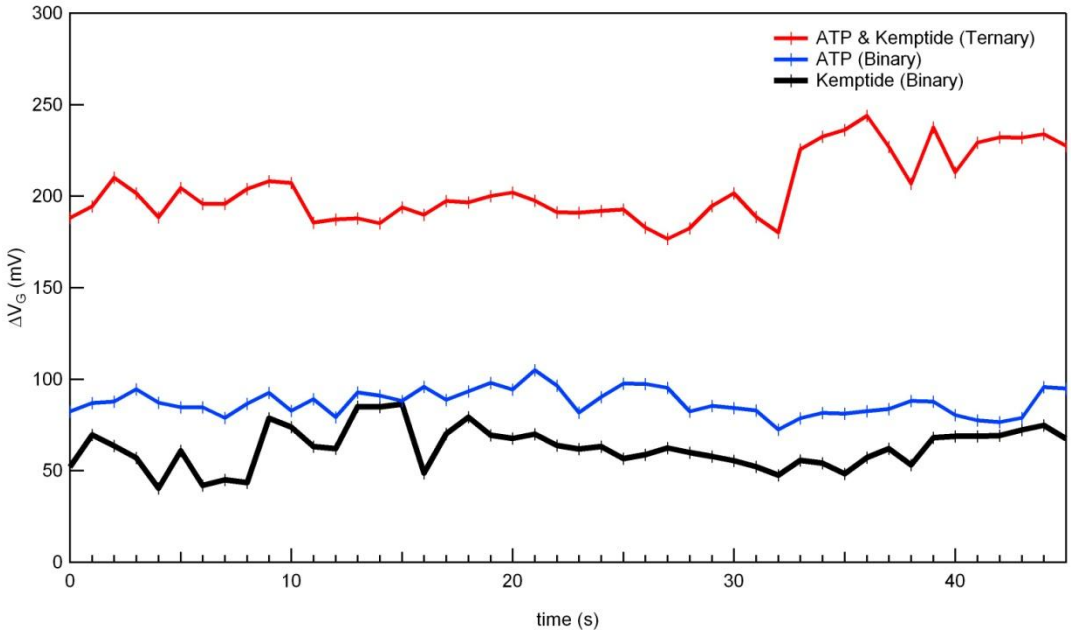


Figure 5.10: Time-dependence of the effective gating of a single PKA device. The transconductance of SWNT device provides a metric for measuring the device response to changes in the protein conformation. From the apoenzyme to binary complex formed by Kemptide (black), the ΔV_G is +65 ± 11 mV. From apoenzyme to binary complex formed by ATP (blue), the ΔV_G is +87 ± 7 mV From apoenzyme to the ternary complex, the ΔV_G is 221 ± 20 mV. Reproduced from [12].

5.9 Electrically-Driven Deposition of Peptides

In order to further understand the recognition and regulation mechanism of PKA, it would be useful to consider the interaction PKA with various peptide inhibitors. Peptides, while biologically interesting, may cause additional complications when

measured using SWNT sensors due to their potential to adsorb to the sidewall of the nanotube through hydrophobic and aromatic interactions. This affinity however leads to additional possibilities in the selective adsorption and patterning of peptides on SWNTs.

The particular peptide considered here is the Protein Kinase Inhibitor (5-24) or PKI. PKI has the following sequence: Thr-Thr-Tyr-Ala-Asp-Phe-Ile-Ala-Ser-Gly-Arg-Thr-Gly-Arg-Arg-Asn-Ala-Ile-His-Asp.[109] Embedded within this sequence are positive and negatively charged residues at pH 7.4 that yield an overall net charge of + 2 q for PKI, but the net charge of the peptide fails to capture the inherent polarity within the sequence itself. The first half of the sequence carries an isolated negative charge due to the aspartic acid while the second half carries four positive charges and a negative charge directly adjacent to one of the positive charged residues. This polarity within the sequence suggests that the molecule should be capable of being oriented in the presence of an external electric field.

While the charge distribution within PKI suggests that the peptide could be electrically oriented and driven to the SWCNT surface through the application of an external electric field, the peptide must irreversibly adsorb to the sidewall in order to functionalize the SWCNT. Furthermore, this adsorption should be stable once the external electric field is no longer applied. For this to occur, it is necessary for the peptide to interact with SWCNT in such a way that is independent of an applied electric field (e.g., aromatically or hydrophobically). In the case of PKI, there is a region encompassing the isolated negative charge that includes both hydrophobic and aromatic residues: Tyr-Ala-Asp-Phe-

Ile-Ala. Of the twenty-one naturally occurring amino acids, three amino acids (phenylalanine, tyrosine, and tryptophan) are aromatic and eight amino acids (alanine, valine, isoleucine, leucine, methionine, phenylalanine, tyrosine, and tryptophan) are hydrophobic, and because of their aromaticity and hydrophobicity, these amino acids can adsorb to the SWCNT sidewall through a π-π or hydrophobic interaction, respectively.[110] Of the seven hydrophobic residues in PKI, five of them encompass the negatively-charged aspartic aid; of these five hydrophobic residues, two are also aromatic. Therefore, this negatively charged region should have a very high affinity to adsorb to sidewall of a SWCNT.

The sequence suggests that applying a negative potential to the liquid with respect to the SWCNT could drive PKI the surface of SWCNT with the preferred orientation for adsorption. By applying a negative potential to the liquid, the negative region of the PKI should orient itself to reside in close proximity to the more positively charged nanotube. This was accomplished by windowing the devices as described in Chapter 2, grounding the SWCNT device, and applying a potential of -0.4 V to a 10 nM PKI solution (100mM MOPs, 9 mM $MgCl_2$, 100 μM TCEP, pH 7.2) for 20 min. The results for two devices can be seen in Figure 5.11. Figure 5.11 (A, B) shows the devices before and after the electrically-driven deposition of PKI, respectively. Even at low concentrations of PKI, there is a substantial amount deposition of the peptide on the nanotube.

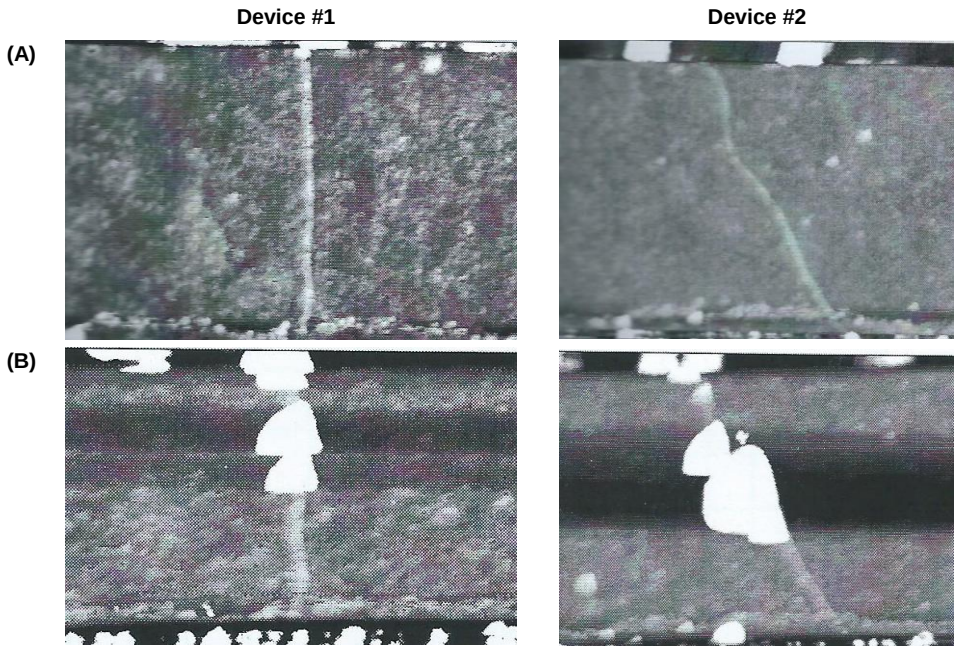


Figure 5.11: Atomic force micrographs (A) before and (B) after the electrically-driven deposition of PKI onto a SWNT using a 10 nM solution of PKI at -0.4V versus Pt(V_{RE}) for 20 minutes.

To confirm that the adsorption of the PKI is initially electrically-driven it is necessary to show that minimal adsorption occurs in the absence of an applied electric field. Figure 5.12(A, B) shows the results before and after incubation in a 30 min 10 nM PKI solution. Evident from Figure 5.12 is that even after a 30 minute incubation there is no substantially deposition of PKI on the nanotube as compared to Figure 5.11. From this it appears that the affinity imparted by the aromatic and hydrophobic residues within the PKI molecule is not sufficient to deposit onto the sidewall of the nanotube.

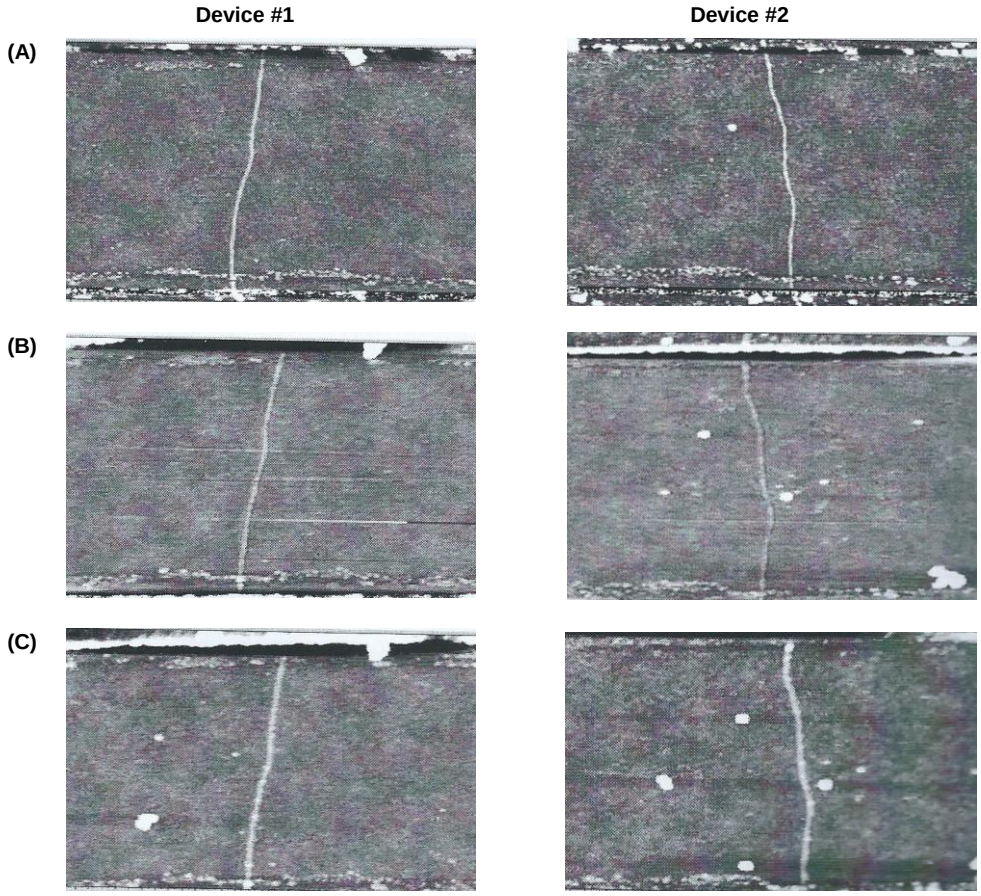


Figure 5.12: Atomic force micrographs (A) before, (B) after a 30 minute incubation in 10 nM PKI solution, and after (C) 20 minutes in a 100 µM Kemptide solution at -0.4V versus Pt(V_{RE}).

To further test electrodeposition of peptides, Kemptide was also used whose sequence is Leu-Arg-Arg-Ala-Ser-Leu-Gly.[88] Figure 5.12 (C) shows the results of the attempt to electrically-drive Kemptide adsorption using a 100 µM solution of Kemptide (100 mM MOPs, 9 mM $MgCl_2$, 100 µM TCEP, pH 7.2) at -0.4 V versus Pt(V_{RE}). The results can be reasonably understood by examining the Kemptide's sequence in further detail.

Kemptide carries an overall net charge of + 2 q due to the two arginine residues. This overall net charge is equivalent to that of PKI, but unlike PKI, Kemptide does not contain any negative charge residues that could impart an effective polarity to the sequence. Also, Kemptide does not contain any aromatic residues nor does it have comparable region of affinity to that of PKI where five of the six residues in a particular sub-sequence are hydrophobic.

While this examination proves that some peptides can be electrically-driven to adsorb onto SWCNTs, the exact mechanism behind the electrically-driven deposition is still elusive. Since deposition of PKI is only observed in the presence of an externally applied electric field, this observation suggests that charged residues serve a critical role in rapidly transporting the peptide to the SWCNT surface, and since the deposition is present after the externally field is removed, this suggests that PKI has high affinity for the nanotube. Similar phenomena have been observed before in the electrically driven patterning of DNA where single-stranded DNA was electrically-driven to surfaces containing complementary oligonucleotides [111]. From the height of the depositions, it is clear that PKI can aggregate or self-assemble either electrostatically or hydrophobically. With further understanding and application of this phenomenon, it is plausible to produce peptide-functionalized SWCNTs that could be used as sensors or as drug-delivery vehicles for therapeutic peptides.

5.10 Summary

In conclusion, SWNT-based devices are proving to be powerful tools for observing single molecule kinetics. Using PKA, we have observed highly variable on- and off-rates for both the substrate and the ATP co-factor, and we have directly observed dynamic interconversion between the intermediate and fully closed conformations. Using 10-minute recordings extending over many thousands of binding events, we have calculated the full transition probability matrix among three possible configurations and the conversion rates among them. The resulting portrait of PKA depicts a highly dynamic enzyme with turnover rates varying over two orders of magnitude. Such abilities befit the function of an enzyme subject to extensive regulatory pressures; as shown by the anti-correlated bound and unbound PKA-Kemptide stabilities changing over time, enzyme regulation could operate on binding to its substrates, but not ATP. Furthermore, the stochastic choreography of PKA motions, with only 77% of events following a set pattern, illustrates the complicated nature of coupling enzyme motion with catalysis.

This study of PKA provides additional opportunities for gaining insight into the catalytic activity of enzymes. First, PKA requires a cofactor in order to effectively catalyze its substrates. PKA can bind up to two Mg^{2+} ions, and its catalytic activity varies whether it is singly or doubly bound.[112] This ability may suggest that the activity, and therefore, its pathways that it regulates are dependent on the ionic environment within the cell. Similarly, the activity of PKA is dependent also on the species of the ion bound.[112] An understanding of the effect of ions have on PKA's activity at the single-molecule may yield answers to the mechanism (e.g. diminished ATP Binding) that reduces its activity.

This could also provide additional insight into how PKA responds to changes in the ionic environment as the enzyme regulates ion channels.[113] Secondly, PKA is a possible target for drugs since it regulates many cellular pathways and any abnormal phosphorylation by PKA may cause a diseased state.[114] For this reason, it would useful to examine the effects of inhibitors of the enzyme in order to understand the inhibition mechanism and the effectiveness of the inhibitors. This may provide an opportunity to screen many candidates to assess their utility as drugs. Next, the ability to work with charged substrates provides an opportunity to drive molecules towards the tethered enzyme. If it is possible to transport substrates rapidly to the enzyme, this could allow for an inexpensive way to study some substrates as high concentrations would not be required to overcome diffusion-limited reactions. Lastly, the main limitation of this technique is its inability to confirm the formation of a product. PKA has a commercially available fluorescent substrate that would allow for simultaneous optical and electronic measurements. This would provide a tour de force approach to couple conformational motion of the enzyme with product formation.

Bibliography

[1] R. Zwanzig, Accounts of Chemical Research **23**, 148 (1990).

[2] T. L. Kuo, S. Garcia-Manyes, J. Y. Li, I. Barel, H. Lu, B. J. Berne, M. Urbakh, J. Klafter, and J. M. Fernandez, Proceedings of the National Academy of Sciences of the United States of America **107**, 11336 (2010).

[3] R. H. Austin, K. W. Beeson, L. Eisenstein, H. Frauenfelder, and I. C. Gunsalus, Biochemistry **14**, 5355 (1975).

[4] M. J. Schnitzer and S. M. Block, Cold Spring Harbor Symposia on Quantitative Biology **60**, 793 (1995).

[5] M. J. Schnitzer and S. M. Block, Nature **388**, 386 (1997).

[6] D. L. Floyd, S. C. Harrison, and A. M. van Oijen, Biophysical Journal **99**, 360 (2010).

[7] D. L. Floyd, J. R. Ragains, J. J. Skehel, S. C. Harrison, and A. M. van Oijen, Proceedings of the National Academy of Sciences of the United States of America **105**, 15382 (2008).

[8] J. R. Moffitt, Y. R. Chemla, K. Aathavan, S. Grimes, P. J. Jardine, D. L. Anderson, and C. Bustamante, Nature **457**, 446 (2009).

[9] S. Myong, M. M. Bruno, A. M. Pyle, and T. Ha, Science **317**, 513 (2007).

[10] K. Svoboda, P. P. Mitra, and S. M. Block, Proceedings of the National Academy of Sciences of the United States of America **91**, 11782 (1994).

[11] Y. Choi, I. S. Moody, P. C. Sims, S. R. Hunt, B. L. Corso, I. Perez, G. A. Weiss, and P. G. Collins, Science **335**, 319 (2012).

[12] P. C. Sims, I. S. Moody, Y. Choi, C. J. Dong, M. Iftikhar, B. L. Corso, Q. T. Gul, P. G. Collins, and G. A. Weiss, Journal of the American Chemical Society **135**, 7861 (2013).

[13] M. H. M. Olsson, W. W. Parson, and A. Warshel, Chemical Reviews **106**, 1737 (2006).

[14] L. Y. P. Luk *et al.*, Proceedings of the National Academy of Sciences of the United States of America **110**, 16344 (2013).

[15] J. Villa and A. Warshel, Journal of Physical Chemistry B **105**, 7887 (2001).

[16] J.-P. Changeux and S. Edelstein, F1000 Biology Reports **3**, 19.

[17] J. Monod, J. Wyman, and J. P. Changeux, Journal of Molecular Biology **12**, 88 (1965).

[18] M. M. Rubin and J. P. Changeux, Journal of Molecular Biology **21**, 265 (1966).

[19] D. E. Koshland, Proceedings of the National Academy of Sciences of the United States of America **44**, 98 (1958).

[20] S. Gianni, J. Dogan, and P. Jemth, Biophysical Chemistry **189**, 33 (2014).

[21] P. J. Tummino and R. A. Copeland, Biochemistry **47**, 5481 (2008).

[22] G. G. Hammes, Y. C. Chang, and T. G. Oas, Proceedings of the National Academy of Sciences of the United States of America **106**, 13737 (2009).

[23] H. P. Lu, L. Y. Xun, and X. S. Xie, Science **282**, 1877 (1998).

[24] B. P. English, W. Min, A. M. van Oijen, K. T. Lee, G. B. Luo, H. Y. Sun, B. J. Cherayil, S. C. Kou, and X. S. Xie, Nature Chemical Biology **2**, 87 (2006).

[25] T. Ha, T. Enderle, D. F. Ogletree, D. S. Chemla, P. R. Selvin, and S. Weiss, Proceedings of the National Academy of Sciences of the United States of America **93**, 6264 (1996).

[26] T. Ha, Methods **25**, 78 (2001).

[27] T. Ha, A. Y. Ting, J. Liang, W. B. Caldwell, A. A. Deniz, D. S. Chemla, P. G. Schultz, and S. Weiss, Proceedings of the National Academy of Sciences of the United States of America **96**, 893 (1999).

[28] T. Hirschfeld, Applied Optics **15**, 3135 (1976).

[29] R. Martel, T. Schmidt, H. R. Shea, T. Hertel, and P. Avouris, Applied Physics Letters **73**, 2447 (1998).

[30] S. J. Tans, A. R. M. Verschueren, and C. Dekker, Nature **393**, 49 (1998).

[31] Y. Cui and C. M. Lieber, Science **291**, 851 (2001).

[32] P. G. Collins, K. Bradley, M. Ishigami, and A. Zettl, Science **287**, 1801 (2000).

[33] Y. Cui, Q. Q. Wei, H. K. Park, and C. M. Lieber, Science **293**, 1289 (2001).

[34] J. Kong, N. R. Franklin, C. W. Zhou, M. G. Chapline, S. Peng, K. J. Cho, and H. J. Dai, Science **287**, 622 (2000).

[35] F. Schedin, A. K. Geim, S. V. Morozov, E. W. Hill, P. Blake, M. I. Katsnelson, and K. S. Novoselov, Nat Mater **6**, 652 (2007).

[36] Y. Lu, B. R. Goldsmith, N. J. Kybert, and A. T. C. Johnson, Applied Physics Letters **97**, 083107.

[37] I. Heller, A. M. Janssens, J. Männik, E. D. Minot, S. G. Lemay, and C. Dekker, Nano Letters **8**, 591 (2008).

[38] P. E. Sheehan and L. J. Whitman, Nano Letters **5**, 803 (2005).

[39] E. Stern, R. Wagner, F. J. Sigworth, R. Breaker, T. M. Fahmy, and M. A. Reed, Nano Letters **7**, 3405 (2007).

[40] H. B. Peng, M. E. Hughes, and J. A. Golovchenko, Applied Physics Letters **89**, 243502 (2006).

[41] B. R. Goldsmith, J. G. Coroneus, A. A. Kane, G. A. Weiss, and P. G. Collins, Nano Letters **8**, 189 (2008).

[42] S. Sorgenfrei, C.-y. Chiu, R. L. Gonzalez, Y.-J. Yu, P. Kim, C. Nuckolls, and K. L. Shepard, Nat Nano **6**, 126 (2011).

[43] E. A. Manrao, I. M. Derrington, A. H. Laszlo, K. W. Langford, M. K. Hopper, N. Gillgren, M. Pavlenok, M. Niederweis, and J. H. Gundlach, Nature Biotechnology **30**, 349 (2012).

[44] B. R. Goldsmith, J. G. Coroneus, V. R. Khalap, A. A. Kane, G. A. Weiss, and P. G. Collins, Science **315**, 77 (2007).

[45] S. Sorgenfrei, C.-y. Chiu, M. Johnston, C. Nuckolls, and K. L. Shepard, Nano Letters **11**, 3739 (2011).

[46] Y. Choi, I. S. Moody, P. C. Sims, S. R. Hunt, B. L. Corso, D. E. Seitz, L. C. Blaszczak, P. G. Collins, and G. A. Weiss, Journal of the American Chemical Society **134**, 2032 (2012).

[47] A. Müller, S. K. Das, H. Bögge, M. Schmidtmann, A. Botar, and A. Patrut, Chemical Communications, 657 (2001).

[48] A. Müller, S. K. Das, P. Kogerler, H. Bögge, M. Schmidtmann, A. X. Trautwein, V. Schünemann, E. Krickemeyer, and W. Preetz, Angew. Chem.-Int. Edit. **39**, 3414 (2000).

[49] L. An, J. M. Owens, L. E. McNeil, and J. Liu, Journal of the American Chemical Society **124**, 13688 (2002).

[50] Madhusudan, P. Akamine, N. H. Xuong, and S. S. Taylor, Nat Struct Biol **9**, 273 (2002).

[51] P. Akamine, Madhusudan, J. Wu, N. H. Xuong, L. F. Ten Eyck, and S. S. Taylor, J Mol Biol **327**, 159 (2003).

[52] Z. Technikova-Dobrova, A. M. Sardanelli, and S. Papa, Febs Letters **292**, 69 (1991).

[53] Y. Choi, T. J. Olsen, P. C. Sims, I. S. Moody, B. L. Corso, M. N. Dang, G. A. Weiss, and P. G. Collins, Nano Letters **13**, 625 (2013).

[54] R. J. Chen, Y. G. Zhan, D. W. Wang, and H. J. Dai, Journal of the American Chemical Society **123**, 3838 (2001).

[55] G. T. Hermanson, *Bioconjugate Techniques* (Academic Press, Inc., Chicago, 2008), 2nd edn.

[56] N. C. Nelson and S. S. Taylor, J Biol Chem **258**, 10981 (1983).

[57] R. Kuroki, L. H. Weaver, and B. W. Matthews, Proceedings of the National Academy of Sciences of the United States of America **96**, 8949 (1999).

[58] S. M. Khamis, R. A. Jones, and A. T. C. Johnson, AIP Advances **1**, 022106 (2011).

[59] Y. C. Lin, C. C. Lu, C. H. Yeh, C. H. Jin, K. Suenaga, and P. W. Chiu, Nano Letters **12**, 414 (2012).

[60] M. Ishigami, J. H. Chen, W. G. Cullen, M. S. Fuhrer, and E. D. Williams, Nano Letters **7**, 1643 (2007).

[61] Y. Zhang, S. L. Yuan, W. W. Zhou, J. J. Xu, and Y. Li, Journal of Nanoscience and Nanotechnology **7**, 2366 (2007).

[62] Y. W. Fan, B. R. Goldsmith, and P. G. Collins, Nature Materials **4**, 906 (2005).

[63] D. T. Kim, H. W. Blanch, and C. J. Radke, Langmuir **18**, 5841 (2002).

[64] T. J. Su, J. R. Lu, R. K. Thomas, Z. F. Cui, and J. Penfold, Journal of Colloid and Interface Science **203**, 419 (1998).

[65] R. J. Chen, S. Bangsaruntip, K. A. Drouvalakis, N. W. S. Kam, M. Shim, Y. M. Li, W. Kim, P. J. Utz, and H. J. Dai, Proceedings of the National Academy of Sciences of the United States of America **100**, 4984 (2003).

[66] Y. Ohno, K. Maehashi, and K. Matsumoto, Journal of the American Chemical Society **132**, 18012 (2010).

[67] I. Heller, S. Chatoor, J. Männik, M. A. G. Zevenbergen, C. Dekker, and S. G. Lemay, Journal of the American Chemical Society **132**, 17149 (2010).

[68] P. Debye and E. Huckel, Z. Phys **24**, 185 (1923).

[69] J. N. Israelachvili, *Intermolecular and surface forces* (Academic Press London, 1991).

[70] G. B. Abadir, K. Walus, and D. L. Pulfrey, Nanotechnology **21**, 015202 (2010).

[71] L. Prisbrey, G. Schneider, and E. Minot, J. Phys. Chem. B **114**, 3330 (2010).

[72] R. Kuroki, L. H. Weaver, and B. W. Matthews, Science **262**, 2030 (1993).

[73] R. Kuroki, L. H. Weaver, and B. W. Matthews, Nature Structural & Molecular Biology **2**, 1007 (1995).

[74] L. Jin, F. E. Cohen, and J. A. Wells, Proceedings of the National Academy of Sciences **91**, 113 (1994).

[75] D. Mann, A. Javey, J. Kong, Q. Wang, and H. J. Dai, Nano Letters **3**, 1541 (2003).

[76] Z. Chen, J. Appenzeller, J. Knoch, Y. Lim, and P. Avouris, Nano Letters **5**, 1497 (2005).

[77] W. Kim, A. Javey, R. Tu, J. Cao, Q. Wang, and H. Dai, Appl. Phys. Lett. **87**, 173101 (2005).

[78] Y.-C. Tseng, K. Phoa, D. Carlton, and J. Bokor, Nano Letters **6**, 1364 (2006).

[79] P. G. Collins, M. S. Fuhrer, and A. Zettl, Appl. Phys. Lett. **76**, 894 (2000).

[80] Y.-M. Lin, J. Appenzeller, J. Knoch, Z. Chen, and P. Avouris, Nano Letters **6**, 930 (2006).

[81] D. Tobias, M. Ishigami, A. Tselev, P. Barbara, E. D. Williams, C. J. Lobb, and M. S. Fuhrer, Physical Review B **77**, 033407 (2008).

[82] J. MÃ¤nnik, I. Heller, A. M. Janssens, S. G. Lemay, and C. Dekker, Nano Letters **8**, 685 (2008).

[83] P. Pjura and B. W. Matthews, Protein Science **2**, 2226 (1993).

[84] J. A. Adams, Chem Rev **101**, 2271 (2001).

[85] D. A. Johnson, P. Akamine, E. Radzio-Andzelm, M. Madhusudan, and S. S. Taylor, Chem Rev **101**, 2243 (2001).

[86] G. Manning, D. B. Whyte, R. Martinez, T. Hunter, and S. Sudarsanam, Science **298**, 1912 (2002).

[87] S. S. Taylor, J. Yang, J. Wu, N. M. Haste, E. Radzio-Andzelm, and G. Anand, Bba-Proteins Proteom **1697**, 259 (2004).

[88] B. E. Kemp, D. J. Graves, E. Benjamini, and E. G. Krebs, J Biol Chem **252**, 4888 (1977).

[89] J. A. Adams and S. S. Taylor, Biochemistry **31**, 8516 (1992).

[90] P. Akamine, Madhusudan, J. Wu, N. H. Xuong, L. F. Ten Eyck, and S. S. Taylor, J Mol Biol **327**, 159 (2003).

[91] J. H. Zheng, E. A. Trafny, D. R. Knighton, N. H. Xuong, S. S. Taylor, L. F. Teneyck, and J. M. Sowadski, Acta Crystallogr D **49**, 362 (1993).

[92] J. Lew, S. S. Taylor, and J. A. Adams, Biochemistry **36**, 6717 (1997).

[93] S. Whitehouse, J. R. Feramisco, J. E. Casnellie, E. G. Krebs, and D. A. Walsh, J Biol Chem **258**, 3693 (1983).

[94] C. T. Kong and P. F. Cook, Biochemistry **27**, 4795 (1988).

[95] D. Q. Ni, J. Shaffer, and J. A. Adams, Protein Science **9**, 1818 (2000).

[96] B. D. Grant and J. A. Adams, Biochemistry **35**, 2022 (1996).

[97] L. R. Masterson, A. Mascioni, N. J. Traaseth, S. S. Taylor, and G. Veglia, Proc Natl Acad Sci U S A **105**, 506 (2008).

[98] Madhusudan, E. A. Trafny, N. H. Xuong, J. A. Adams, L. F. Teneyck, S. S. Taylor, and J. M. Sowadski, Protein Sci **3**, 176 (1994).

[99] N. Narayana, S. Cox, X. Nguyen-huu, L. F. Ten Eyck, and S. S. Taylor, Structure **5**, 921 (1997).

[100] L. R. Masterson, C. Cheng, T. Yu, M. Tonelli, A. Kornev, S. S. Taylor, and G. Veglia, Nat Chem Biol **6**, 821 (2010).

[101] S. N. Xie, Single Mol **2**, 229 (2001).

[102] H. Yang, G. B. Luo, P. Karnchanaphanurach, T. M. Louie, I. Rech, S. Cova, L. Y. Xun, and X. S. Xie, Science **302**, 262 (2003).

[103] J. Park, S. Myong, A. Niedziela-Majka, K. S. Lee, J. Yu, T. M. Lohman, and T. Ha, Cell **142**, 544 (2010).

[104] For Kemptide, the tails are composed of 5% of all events. For ATP, the tails are composed of 15% of binding times and 32% of waiting times.

[105] I. Goychuk, Physical Review E **80**, 046125 (2009).

[106] J. R. Knowles, Nature **350**, 121 (1991).

[107] I. A. Rose, E. L. O'Connell, and S. Litwin, J Biol Chem **249**, 5163 (1974).

[108] J. A. Adams, M. L. McGlone, R. Gibson, and S. S. Taylor, Biochemistry **34**, 2447 (1995).

[109] H. C. Cheng, B. E. Kemp, R. B. Pearson, A. J. Smith, L. Misconi, S. M. Vanpatten, and D. A. Walsh, Journal of Biological Chemistry **261**, 989 (1986).

[110] C. H. Wang, S. Li, R. Q. Zhang, and Z. J. Lin, Nanoscale **4**, 1146 (2012).

[111] M. S. Bowen *et al.*, edited by U. S. P. a. T. Office (Illumina, 2014).

[112] J. A. Adams and S. S. Taylor, Protein Science : A Publication of the Protein Society **2**, 2177 (1993).

[113] P. C. Gray, J. D. Scott, and W. A. Catterall, Current Opinion in Neurobiology **8**, 330 (1998).

[114] P. Cohen, Nat Rev Drug Discov **1**, 309 (2002).